New physics from rare beauty

VRIJE UNIVERSITEIT

New physics from rare beauty

ACADEMISCH PROEFSCHRIFT

ter verkrijging van de graad Doctor aan
de Vrije Universiteit Amsterdam,
op gezag van de rector magnificus
prof.dr. L.M. Bouter,
in het openbaar te verdedigen
ten overstaan van de promotiecommissie
van de faculteit der Exacte Wetenschappen
op maandag 1 maart 2010 om 11.45 uur
into the aula van de universiteit,
De Boelelaan 1105

door

Eduard Ebron Simioni

geboren te Cittadella, Italië

promotor:	prof.dr. M.H.M. Merk
copromotoren:	dr. A. Pellegrino
	dr. W.D. Hulsbergen

This work is dedicated to the memory of Norbert Scheu,
brilliant scientist and a dear friend.
He was a kind and gentle soul who had a great sense of humor.
He was too young to leave us. Rest in peace Norbert.

I wish you to find the Question.

Contents

Chapter 1

Introduction

The Standard Model (SM) of particle physics offers a framework to describe sub-nuclear physics processes. These processes involve three of the four known fundamental forces of Nature: the strong force, the weak force and the electromagnetic force (gravity is not included in the SM). The SM building blocks are 12 elementary particles (six quarks and six leptons), interacting through the exchange of four types of gauge vector bosons and a scalar Higgs boson. All SM gauge bosons except for the Higgs boson [1] have been experimentally observed. The photon and the gluons are massless and are responsible for the electromagnetic and strong interaction, respectively. The W and Z have a mass of 80.4 GeV and 91.2 GeV respectively, and are responsible for the weak interactions.

Despite its success in describing a large variety of sub-nuclear phenomena, the SM leaves open a number of questions: it does not give an explanation of the spectrum of fermion masses and mixings; it does not achieve the unification of fundamental interactions (three different gauge coupling constants do not converge to a single value [2]); it has quadratic divergences in the radiative corrections to the Higgs mass ("fine-tuning" [3] and hierarchy problems). For this reasons the SM is regarded by particle physicists as an effective quantum field theory, rather than a credible candidate to be the ultimate theory of fundamental interactions. Further problems to the SM are provided by cosmology. E.g. to account for the "baryogenesis" (postulated by Andrei Sakharov in 1967 [4] to explain the excess of matter over antimatter in the universe), baryon number violation, Charge (C) and Charge-Parity (CP) symmetry violation, and interactions out of thermodynamic equilibrium are required: the SM can accommodate such conditions, but their effect does not seem to be strong enough to explain the present baryon asymmetry [5]. These and other considerations have led particle physicists to postulate the existence of New Physics (NP) beyond the SM. This would result into the creation of new particles that could then be observed at higher energy regimes than hitherto explored. These particles could be observed directly or indirectly, through their contributions to quantum loops. A promising ground to look for NP are the Flavor Changing Neutral Currents (FCNCs). In those

processes the SM contributions are suppressed (rare decays) since they are forbidden at the tree level and can proceed only via loop diagrams.
Due to its precise theoretical prediction, one of the most promising rare decay channel is the B_s meson decaying into two muons. In this dissertation the strategy for an early measurement of the $B_s \to \mu^+\mu^-$ branching ratio at the "Large Hadron Collider beauty" (LHCb) experiment [6] will be illustrated.
LHCb is one the four particle physics detector experiments being constructed at the Large Hadron Collider (LHC) accelerator at CERN (European Organization for Nuclear Research). It is the only LHC experiment explicitly designed to study CP violation and rare B hadron decays.

Outline of this thesis

This dissertation, aimed at describing a method to determine the $B_s \to \mu^+\mu^-$ branching ratio, is mainly concerned with four topics:

- *Rare B meson decays and the LHCb experiment (Chapters 2 and 3)*
  The SM framework is presented. In Sec. 2.3.1, the Minimal super-symmetrical extension of the SM (MSSM), proposed as a natural theory to solve the fine-tuning problem of quadratic divergences of the Higgs mass, is introduced. The MSSM has 124 free parameters, 105 more than the SM. However, based on experimental bounds, the free parameters can be constrained by requiring consistency with the present experimental measurements, resulting in a SUSY model with less parameters and higher predictive power. The current experimental limit on the $\mathrm{Br}(B_s \to \mu^+\mu^-)$ is discussed in Sec. 2.2. An Overview of the LHC machine and of the LHCb experiment is given in Chapter 3. The LHCb sub-detectors are briefly discussed, together with the LHCb trigger system.

- *Outer Tracker detector and readout (Chapters 4 and 5)*
  LHCb is essentially a spectrometer: particles in the LHCb acceptance must be efficiently detected and have their momentum measured with a resolution of $\frac{\delta p}{p} \approx 0.5\%$. The Outer Tracker (OT) detector, covering most of the tracking volume, is described in detail. Low intensity irradiation tests of the OT showed that the amplification degrades relatively rapidly. An overview of the OT aging is given. The drift times of particles detected in the detector are measured by the OT electronics as the time difference between the hit signals from the anode wires and the LHC bunch crossing clock. The Front-End Electronics contains all the circuitry necessary to read out the hit signals from the straw tubes, determine their timing with respect to the LHC clock, and ship them to the off-detector electronics. The OT has been installed and the electronics built and commissioned for data taking.

- *Momentum resolution studies (Chapter 6)*
  Detailed studies of the systematic uncertainties related to the OT geometry

are of paramount importance in the decay mass reconstruction. A misaligned tracking system leads to a deterioration of the track reconstruction performance that can be quantified in terms of efficiency loss and reduced track parameter resolution. The degradation of the momentum resolution due to these misalignments is studied. Another source of bias in the momentum reconstruction are errors in the magnetic field parametrization. The effect of a B-field scale transformation and its relation with a common translation of the tracking stations is studied.

- *$B_s \to \mu^+\mu^-$ branching ratio exclusion limit and sensitivity (Chapter 7)*
  The SM prediction for the $B_s \to \mu^+\mu^-$ branching ratio is $(3.35 \pm 0.32) \times 10^{-9}$ [8, 9]. A crucial issue for such a measurement is the background rejection, depending on vertexing and mass resolution. Using a Monte Carlo simulation the potential of LHCb in measuring the $B_s \to \mu^+\mu^-$ branching ratio is investigated. The analysis strategy for the extraction of the branching ratio and the normalization with control channels is described.

Chapter 2

$B_S \to \mu^+\mu^-$ in the SM and beyond

In this chapter, the theoretical framework of the dissertation is presented (Sec. 2.1) and the choice of the B_s decay into a $\mu^+\mu^-$ pair as a tool to search for new physics beyond the Standard Model (SM) is motivated (Sec. 2.2). In particular, large Flavour Changing Neutral Currents (FCNCs) are disfavored in the SM, whereas they are favored in several Super Symmetry models (Sec. 2.3).

2.1 Standard Model

The SM of fundamental interactions is a gauge theory describing electroweak and strong interactions. The interactions proceed through the exchange of gauge particles associated to the local symmetry group

$$SU(3)_C \otimes SU(2)_L \otimes U(1)_Y. \tag{2.1}$$

The SM building blocks are summarized in Tab. 2.1. They are divided into three sectors: the gauge sector (vector bosons), the fermion sector (quarks and leptons) and the Higgs sector (scalar boson). The theory is described by the fundamental Lagrangian:

$$\mathcal{L} = \mathcal{L}(SU(3)_C) + \mathcal{L}(SU(2)_L \otimes U(1)_Y) + \mathcal{L}(Higgs) + \mathcal{L}(Yukawa). \tag{2.2}$$

The Yukawa interaction is used to describe the coupling between the Higgs, quarks and leptons. The symmetry is spontaneously broken by the vacuum expectation value of the Higgs field (v), which also allows the fermions to acquire mass via Yukawa interactions.
The interactions involving the neutral bosons Z^0, γ and gluons conserve the flavor, therefore FCNC transitions are forbidden at the tree level. Charged current processes mediated by $W^\pm$ are flavor violating and the strength of the violation is given by the

Fermions ($S = 1/2$)					**Bosons** ($S = 1$)		
	Charge	Generation I	II	III		Charge	
Quarks	$+\frac{2}{3}$	u up	c charm	t top	G gluon	0	Strong
	$-\frac{1}{3}$	d down	s strange	b bottom	γ photon	0	Electroweak
Leptons	0	ν_e electron neutrino	ν_μ muon neutrino	ν_τ tau neutrino	Z boson	0	
	-1	e electron	μ muon	τ tau	W boson	± 1	
Scalar Higgs Boson ($S = 0$) H							

Table 2.1: *The elementary particles in the SM.*

weak gauge coupling g and a unitary $3 \otimes 3$ matrix, (the CKM matrix [10–12]). As a consequence, weak eigenstates (d', s', b') and the corresponding mass eigenstates d, s, b are connected by:

$$\begin{pmatrix} d' \\ s' \\ b' \end{pmatrix} = \begin{pmatrix} V_{ud} & V_{us} & V_{ub} \\ V_{cd} & V_{cs} & V_{cb} \\ V_{td} & V_{ts} & V_{tb} \end{pmatrix} \begin{pmatrix} d \\ s \\ b \end{pmatrix} \quad . \tag{2.3}$$

The coefficients V_{ij} are in general complex numbers. Imposing unitarity constraints to the CKM matrix, four parameters are left: three real parameters and a complex phase. The complex phase is the main source of CP violation in the SM.

2.2 Expectation for the Br($B_s \to \mu^+\mu^-$) in the SM

The SM allows B_d and B_s mesons to decay to e^+e^-, $\mu^+\mu^-$ or $\tau^+\tau^-$ final states via FCNCs transitions, absent at tree level, but allowed by loop diagrams involving both W and Z propagators as shown in Fig. 2.1. They correspond to a set of basic effective vertices called "penguin" (Fig. 2.1(c)) and "box" (Fig. 2.1(d)) diagrams, respectively. Even at the quantum loop level, the amplitude from FCNCs diagrams (proportional to off-diagonal elements of the $V^\dagger_{CKM}V_{CKM}$ matrix) are strongly reduced by the unitarity of the CKM matrix, and they are ultimately not zero due to the non-degeneracy of the quark masses. The presence of different quark masses in the propagator ensures a non-zero amplitude, roughly proportional to $\frac{m_q^2}{M_W^2}$ (GIM mechanism [13]).
In addition, B_d decays are suppressed relative to the B_s decays by a factor $|V_{td}/V_{ts}|^2$

and the branching ratios of double leptonic B decays is proportional to the square of the final state lepton masses (the so called "helicity suppression" [14]). Therefore, the largest branching fraction is associated to $B_s \to \tau^+\tau^-$ (about 4×10^{-7}) and the smallest to $B_d \to e^+e^-$ (about 2×10^{-15}). Decays to the final states $e^\pm\mu^\mp$, $e^\pm\tau^\mp$ or $\mu^\pm\tau^\mp$ are forbidden in the SM by lepton number conservation.

The decays of B_d and B_s into two leptons are also theoretically "clean". In the

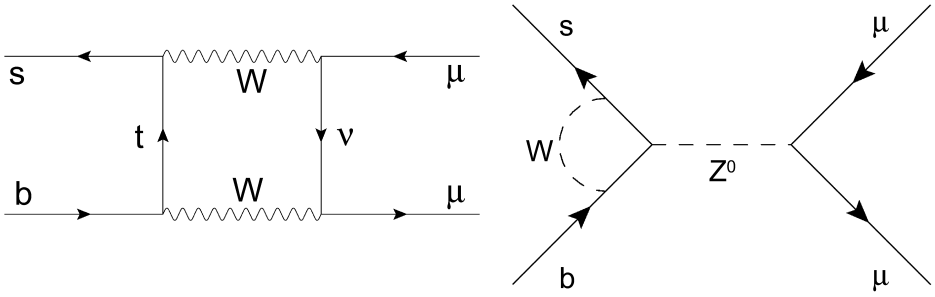

(a) SM box diagram (b) SM penguin diagram

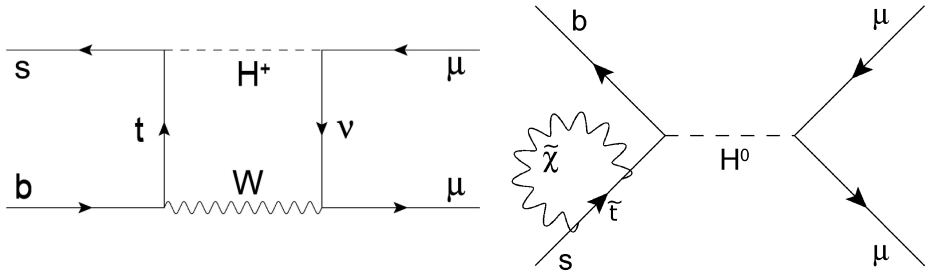

(c) SUSY box diagram (d) SUSY penguin diagram

Figure 2.1: *Examples of $B_s \to \mu^+\mu^-$ diagrams in the SM (a) and (b) and SUSY (c) and (d).*

models with Minimal Flavour Violation (MFV) the ratio between the B_s^0 oscillation frequency (ΔM_s) and and the Br($B_s \to \mu\mu$) do not depend on the B_s meson decay constant (which is the main theoretical uncertainty in the prediction) and the CKM matrix elements. The only hadronic parameter left is related to $B_s - \bar{B_s}$ mixing (the so called "bag parameter"). Since the values of ΔM_s have been measured ($17.77 \pm 0.12 ps^{-1}$ [7]) the prediction of the Br($B_s \to \mu\mu$) is [8, 9]:

$$Br^{SM}(B_s \to \mu\mu) = (3.35 \pm 0.32) \times 10^{-9}. \tag{2.4}$$

The assigned error accounts for the various experimental uncertainties (the B_s lifetime $\tau(B_q)$, the top quark mass m_t and oscillation frequency ΔM_s).
Among the double-leptonic decays of the B-mesons, the $B_s \to \mu^+\mu^-$ seems the most promising because it is the one with the larger branching ratio compared to electrons and muons in the final state are much easier to detect compared to tau leptons.
The current exclusion limit on the Br($B_s \to \mu^+\mu^-$) was set at the Tevatron collider:

$$Br^{95\%CL}(B_s \to \mu^+\mu^-) < 4.7(5.3) \times 10^{-8} \tag{2.5}$$

by CDF and D0 respectively [15,16]. The limit on $B_s \to \mu^+\mu^+$ is still more than an order of magnitude higher than the SM expectation.
As will be explained in the following chapters, thanks to the high B meson production rate in the LHC and the excellent momentum resolution of the experiment, LHCb has the potential to significantly improve these results, scanning the branching ratio region down to the SM value with early data. The LHCb potential for measuring/excluding the SM $B_s \to \mu^+\mu^-$ branching ratio sets excellent prospects for possible future indirect detection effects of physics beyond the SM.
Moreover, two general purpose LHC-experiments, ATLAS [17] and CMS [18], in addition to their main discovery program, will perform rare B decays measurements. First results are planned in 2009/2010 when the integrated luminosity is expected at the level of 10 to 30 fb^{-1} and the resulting upper limit on the branching fraction is estimated to be at the level of the SM prediction [19, 20].

2.3 Beyond the Standard Model

The SM is affected by problems due to the quadratic divergences of the Higgs mass. In the SM the Higgs mass receives a divergent contribution from each fermion coupling with it (see Fig. 2.2(a)) through the Yukawa interaction defined as

$$\mathcal{L}_{Yukawa} = -\lambda_f \langle \bar{\psi} | H | \psi \rangle \tag{2.6}$$

where λ_f is the Yukawa constant associated to the fermion field ψ (and proportional to its mass after diagonalization of the mass matrix) and H is the Higgs field.
Direct searches constrain the Higgs mass above 114.4 GeV at 95% CL [7,21,22] and precise measurements of the SM electroweak sector (i.e. $W^\pm$ and top mass measurements) constrain the SM Higgs mass below 175 GeV at 95% CL [7]. To account for these limits on the Higgs mass, the parameters in the expansion of the Higgs mass in a series of bare couplings must be fine tuned which is sometimes considered to be "unnatural" [7]. In addition, the number of fundamental fermions and their masses as well as the flavor mixing parameters remain unexplained. Moreover, the couplings of the electromagnetic, weak and strong force are a function of the energy scale and a unification of these couplings are expected at a certain energy scale (Grand Unification Theory scale) as a manifestation of a common origin of these three interactions. In the SM this unification is not achieved (see Fig. 2.3).

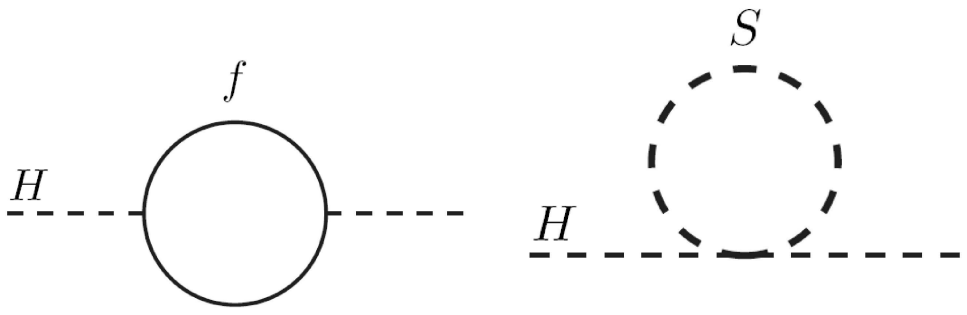

(a) Fermion contribution (b) Scalar contribution

Figure 2.2: *One loop corrections to the Higgs mass mass parameter due to a fermion (a) and a scalar (b).*

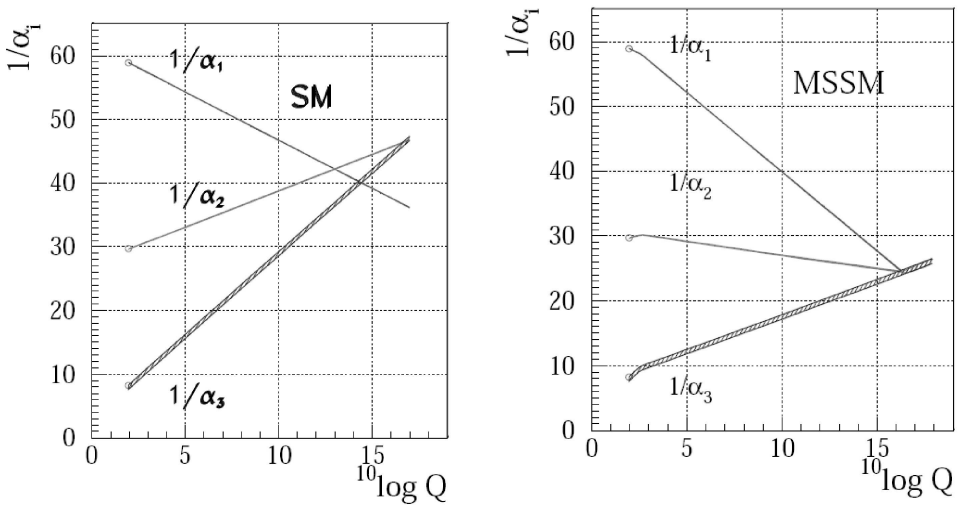

(a) SM (b) MSSM

Figure 2.3: *Evolution of the inverse of the three coupling constant in the SM (a) and in the super-symmetrical extension of the SM (MSSM, see text). Only in the latter case unification is obtained.*

2.3.1 Minimal Super-Symmetric extension of the SM (MSSM)

A very attractive method to solve the Higgs mass fine-tuning problem in a "natural" way, is to build a theory in which the physical mass of the Higgs and the corresponding bare mass of the fundamental Lagrangian are the same. This is the case for super-symmetric (SUSY) models which involve a space time symmetry relating bosonic and fermionic degrees of freedom. Super symmetry associates to each fermion a complex scalar boson and for each gauge boson a fermion. Consequently fermions are grouped together with bosons in objects called super-multiplets. In SUSY the Higgs couples also to scalars as shown in the diagram of Fig. 2.2(b). Due to the spin-statistics theorem, the fermions and the bosons have opposite sign contributions to the Higgs mass correction. Requiring the scalar Yukawa coupling $\lambda_s = |\lambda_f|^2$, the two contributions naturally cancel each other, without any fine-tuning. However, SUSY particles with low mass have not been observed. As consequence, if supersymmetry exists, it must be broken and SUSY particles are presumably heavier than the energy scale so far reached at colliders.
The simplest SUSY extension of the SM is the MSSM. It consists of adding all the SUSY partners to SM particles and enlarging the SM Higgs sector to a complex scalar doublet to generate the mass for both u and d quarks families. The total number of parameters in the MSSM is 124 among which 18 are the known SM parameters, one is the singlet scalar Higgs and 105 are new free parameters [23]. The general nomenclature for the spin-0 partners of quarks and leptons are constructed by prepending an "s", for scalar (squarks and sleptons). The generic nomenclature for the spin-1/2 super-partners is to append "ino" to the name of the SM Model particle, e.g. the fermionic partners of the Higgs scalars are called higgsinos.
The electroweak breaking occurs when the Higgs doublets acquire a vacuum expectation value. The mass parameters of the Higgs sector can be re-expressed in terms of the vacuum expectation values v_d and v_u and the scalar Higgs mass parameter. Moreover, the sum $v_d + v_u$ is constrained by the relation:

$$v_u^2 + v_d^2 = \frac{4m_W^2}{g^2} = (246\ GeV)^2, \tag{2.7}$$

while the ratio

$$\frac{v_u}{v_d} = tan\beta, \tag{2.8}$$

remains a free parameter.
This parameter can play a key role in the onset of new physics in the $B_s \to \mu^+\mu^-$ branching ratio. This can be seen e.g. in some modified SUSY models. Despite being natural theories SUSY in its general form leads to predictions inconsistent with the current experimental observations, i.e. a too high proton decay rate predicted as consequence of the exchange of SUSY particles. To overcome this problem the conservation of "R-parity" was postulated. R-parity is a quantum number defined as: $R = (-1)^{3(B-L)+2S}$ where B and L are the baryon and lepton number and S is the

particle spin. All SM particles are even R-Parity eigenstates while the super partners are odd R-Parity eigenstates. Due to R-Parity conservation, super-symmetrical particles must be produced in pairs and the lightest SUSY particles must be stable and, most likely, electrically and color neutral [24] (providing a natural candidate for cold dark matter).
Moreover, in general the MSSM does not predict the suppression of FCNCs, provides unobserved sources of CP violation, predicts large dipole moments in the neutron, electrons and atoms, and finally allows the violation of the lepton numbers L_e, L_μ and L_τ [14]. Those phenomenological deficiencies rule out most of the parameter space of the MSSM. Based on experimental bounds, the 105 new free parameters can be constrained by requiring the consistency with the experimental measurements, resulting in SUSY models with less parameters and higher predictive power.

2.3.2 Minimal super gravity (mSUGRA)

To guarantee the absence of FCNCs mediated by virtual super-symmetric particle exchange, in mSUGRA it is assumed that the diagonal soft-super-symmetry-breaking scalar squared masses are universal at a given energy scale. The low energy MSSM parameters, relevant for collider physics, are then derived using the renormalization group equations (this is the so called "top-down" approach). In practice the applied conditions reduce the parameters by assuming equal masses at the Plank scale. Typical mSUGRA models give low energy values for the scalar masses with squark masses larger than slepton masses [25]. With these constraints the MSSM spectrum and its interaction strenghts are determined by the known 18 SM parameter plus the following five:

- $\tan\beta$: ratio of the vacuum expectation value among the two Higgs fields,
- $sgn(\mu)$: the sign of the Higgs mixing parameter,
- m_0: scalar Higgs mass,
- $m_{1/2}$: the universal scalar gaugino mass,
- A_0: trilinear (Higgs-squark-squark or Higgs-slepton-slepton) coupling term.

This simplified approach facilitates the study of phenomenology at colliders and sets benchmark in super-symmetrical parameter surfaces, from which masses and couplings could be derived. In particular an interpretation of the measured excess in $(g-2)_\mu$ in terms of mSUGRA corrections [26] implies a substantial super-symmetric enhancement of the branching ratio $B_s \to \mu\mu$. For not-too-large m_0, $m_{\frac{1}{2}} \leq 500\ GeV$ and $A_0 \approx 0$ the following relation holds (see Fig. 2.4):

$$Br^{SUSY}(B_s \to \mu\mu) = Br^{SM}(B_s \to \mu\mu) + 10^{-6} GeV^4 \times \frac{tan^6\beta\ m_{1/2}^2}{(m_{1/2}^2 + m_0^2)^3} \qquad (2.9)$$

The measurement of the BR($B_s \to \mu^+\mu^-$) could be a key measurement for discovering or excluding such a model.

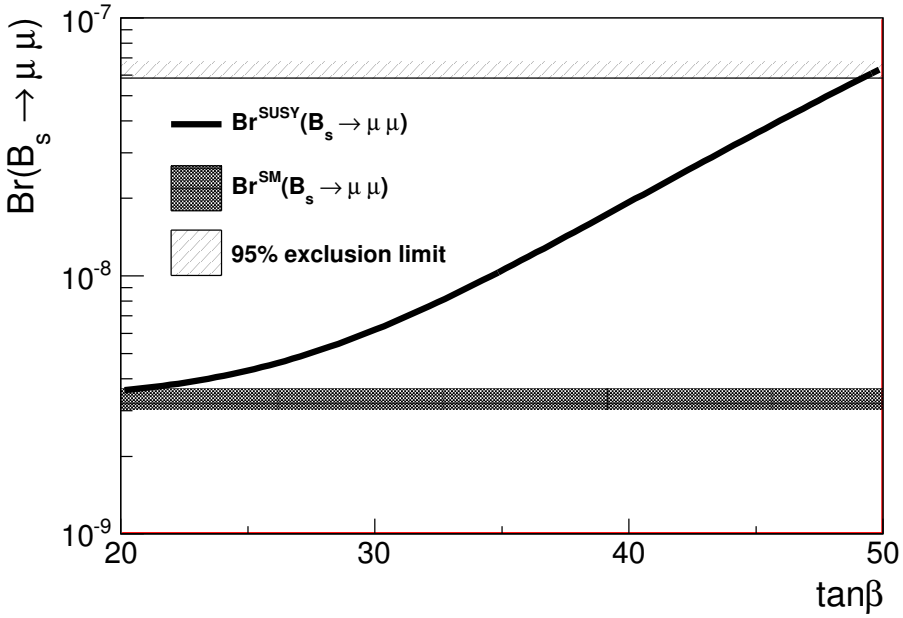

Figure 2.4: *$B_s \to \mu^+\mu^-$ branching ratio versus tanβ. The dashed area indicate the the current 95% exclusion limit set by CDF and the horizontal bar indicate the SM prediction.*

2.3.3 Constrained MSSM with Non Universal Higgs Masses (NUHM)

In this model the assumed universality for the soft SUSY-breaking masses in the mSUGRA framework is relaxed. The soft SUSY-breaking scalar masses are no longer the same as all the other squarks and sleptons. The models based on this assumption are called NUHM. The parameter space of the NUHM is two dimensions larger than the mSUGRA. This allows to study benchmark surfaces for the full Higgs MSSM sector.

In [27] the plane $m_{1/2}$ versus tanβ (where $m_{1/2}$ is indicated as M_A reference [27]) is studied for fixed values of the parameters m_0 and μ. The parameters were constrained by using the following experimental observables: the limit on the Higgs mass measured by LEP ($m_{Higgs} \leq 176\ GeV$ at 95% CL [21]), the relic dark matter density Ω_{CDM} [28] and the 3.4 σ discrepancy in the anomalous magnetic moment of the muon [29].

As shown in Fig. 2.5, for the considered benchmark surface, a best-fit point corresponds to tan$\beta \approx 37$ which corresponds to a Br($B_s \to \mu^+\mu^-$) of the order of $\sim 10^{-8}$ (see Fig. 2.4). This result is very encouraging, given that this would imply an early measurable deviation from the SM prediction.

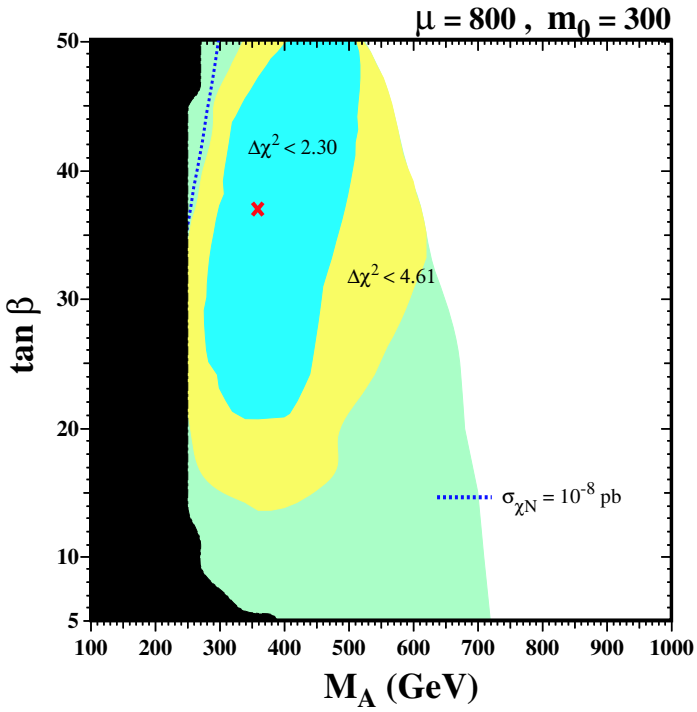

Figure 2.5: *The $(m_A,\ tan\beta)$ planes for the NUHM benchmark surfaces. The cross indicates the minimum value of the χ^2 corresponding to the most probable scenario based on experimental constraints (see text and [27]). The corresponding value of the $Br(B_s \to \mu^+\mu^-)$ is about $\sim 10^{-8}$.*

Chapter 3

The LHCb detector at LHC

The Large Hadron Collider beauty (LHCb) experiment is located at the European Center for Nuclear Research (CERN). It is designed to perform precision measurements of Charge Parity violation in the B-meson system and branching ratios of rare B decays at the Large Hadron Collider (LHC). The LHC is a two-rings, superconducting hadron-hadron collider that started operating in September 2008. Due to a failure in the cooling system, which lead to an explosion, LHC was interrupted few weeks later until november 2009. Currently LHC is successfully colliding protom beams. The LHC layout is shown in Fig. 3.1. It was built in the LEP [30] tunnel, which has a radius of 4.3 km. Equating the Lorentz and the centripetal force, one obtains the following expression for the proton momentum:

$$p[TeV] = 0.3 \times B[T] \times R[Km]. \tag{3.1}$$

Therefore, to achieve the nominal design beam momentum of $p = 7\ TeV$, a magnetic field strength of B = 5.4 T is needed. In practice, the LHC tunnel is not completely filled with magnets and the required bending power is obtained with about 1200 superconducting dipole magnets, providing a field of 8.33 T each (the actual field in the storage ring depends on the heat load and temperature inside the cryo-magnets). These magnets are cooled down to a temperature of 1.9 K by cryostats containing super-fluid helium.

The LHC machine is designed to achieve a luminosity of $10^{34} cm^{-2} s^{-1}$. The luminosity depends on several beam parameters [31]:

$$Luminosity = \frac{N^2 n f_{rev} \gamma_r}{4\pi \epsilon_n \beta^*} F, \tag{3.2}$$

where N is the number of particles per bunch, n is the number of bunches per beam, f_{rev} the revolution frequency, γ_r is the relativistic gamma factor, ϵ_n is the (normalized) transverse beam emittance, β^* is the optical β-function at the interaction point and F is the geometric reduction factor due to the beams crossing angle. The luminosity in LHC is not constant and decreases due to the collisions themselves; the

estimated beam lifetime is about 15 hours. A summary of the main LHC parameters is given in Tab. 3.1. As shown in Fig. 3.1, four experiments are installed in the LHC ring: ATLAS [17] and CMS [18] are general-purpose experiments searching among others for the Higgs boson and for super-symmetric particles; ALICE [33] is a heavy ions experiment to study the behavior of nuclear matter at very high energies and densities; LHCb [34] is dedicated to study the decays of B mesons. In this chapter, the LHCb detector layout and components are described.

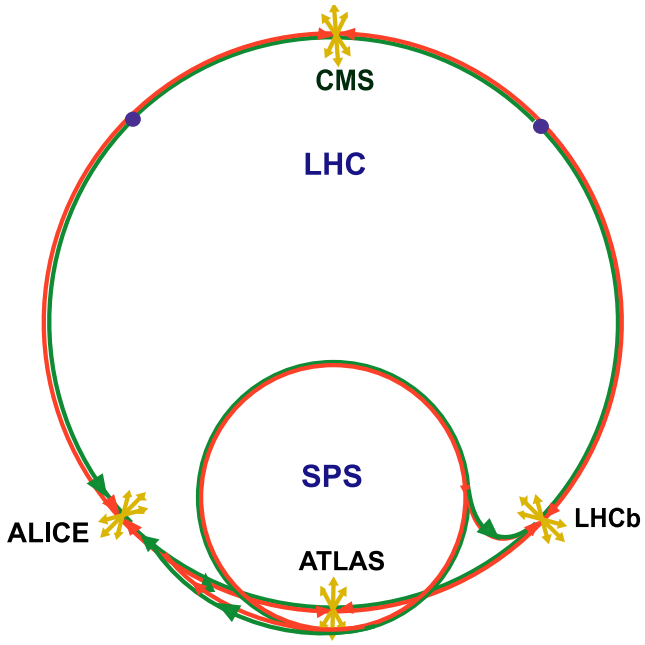

Figure 3.1: *Schematic view of the 27 km long LHC ring. The position of the four experiments is indicated. The inner ring is the Super Proton Synchrotron (SPS), which injects bunches of 450 GeV protons into the LHC ring.*

3.1 The LHCb experiment

The LHCb experiment was designed to precisely measure CP violating effects in specific B mesons decays as well as branching ratios of rare decays. From the LHC proton-proton collisions, B mesons are predominantly produced in either the forward or the backward direction, as shown in Fig. 3.2. Only forward events are collected by the LHCb detector, covering an acceptance from 15 $mrad$ to 300 $mrad$ in the horizontal plane, and from 10 to 250 $mrad$ in the vertical plane. The detector layout is shown in Fig. 3.4. In this dissertation, a right-handed coordinate system is adopted: the positive z axis is defined as pointing from the interaction vertex towards the muon detector, and the positive y axis is pointing upwards; the x axis

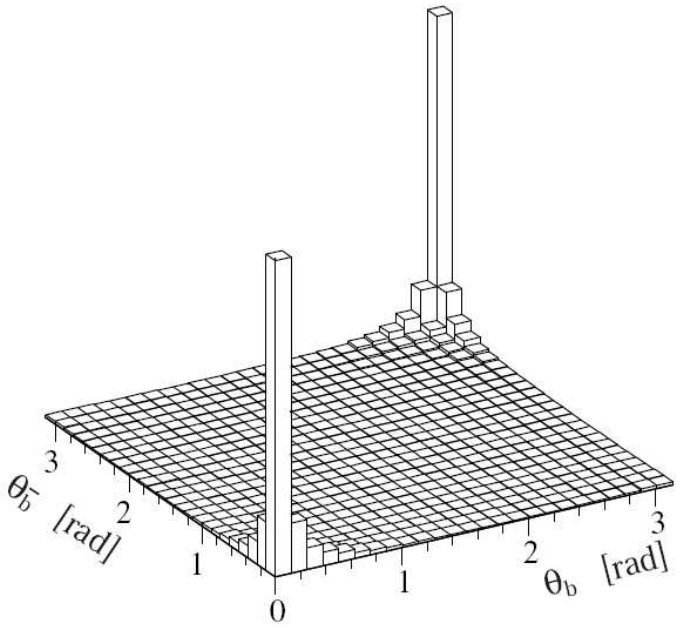

Figure 3.2: *Polar angles of the b and $\bar{b}$ calculated by the PYTHIA event generator [35].*

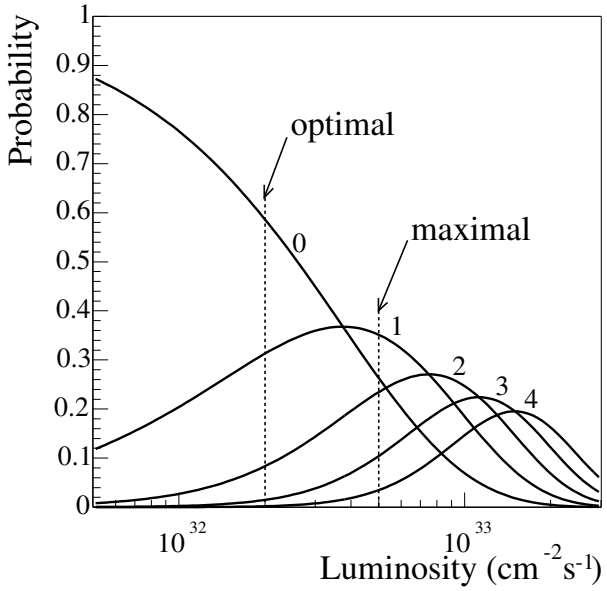

Figure 3.3: *Probability for multiple inelastic collisions (0, 1, 2, 3, 4) per bunch crossing as function of luminosity. LHCb was designed to operate between the optimal luminosity of $2\times10^{32}\mathrm{cm}^{-2}\mathrm{s}^{-1}$ and the maximal luminosity of $5\times10^{32}\mathrm{cm}^{-2}\mathrm{s}^{-1}$.*

Circumference	26659 m
Energy per beam	7 TeV
Nominal CMS energy	14 TeV
Injection energy	0.45 TeV
Field at 450 GeV	0.535 T
Field at 7 TeV	8.33 T
Helium temperature	1.9 K
Luminosity	$10^{34} cm^{-2} s^{-1}$
Bunch spacing	25 ns
Luminosity lifetime	15 h

Table 3.1: *Summary of the main LHC parameters. In the first year LHC will run at a lower CMS (center of mass energy of 7 TeV)*

points horizontally away from the center of the LHC ring.
For LHCb the value of β^* in Eq. 3.2 is modulated to achieve a reduced luminosity of $2\times10^{32}\text{cm}^{-2}\text{s}^{-1}$, to reduce the probability to get more than one event per bunch crossing (see Fig. 3.3). This also reduces the hit multiplicity in the detectors and the resulting radiation damage.

The LHC beams pass through the LHCb detector within a beam pipe consisting of four conical sections from 2 to 6 meters in length, as shown in Fig. 3.5. The first three sections are made of beryllium to minimize the creation of secondary particles while still withstanding the design beam vacuum of 10^{-9} $mbar$.

The LHCb detector is a forward spectrometer. The trajectories of charged particles are deflected by the B field when traversing the magnet and their momentum is then measured. The bending power of the magnet is represented by the integrated field

$$\int dz \times B_y = 4.2\ Tm. \tag{3.3}$$

The y component of the magnetic field (B_y) is the dominant one and therefore the charged particles trajectories are bent in the xz-plane. The strength of the main component of the magnetic field versus the z axis is shown in Fig. 3.6. During three campaigns (December 2004, June 2005 and December 2005), the components of the B field were measured across the tracking volume and the B field accuracy measurement was estimated to be better than 10^{-3} T [36,37].

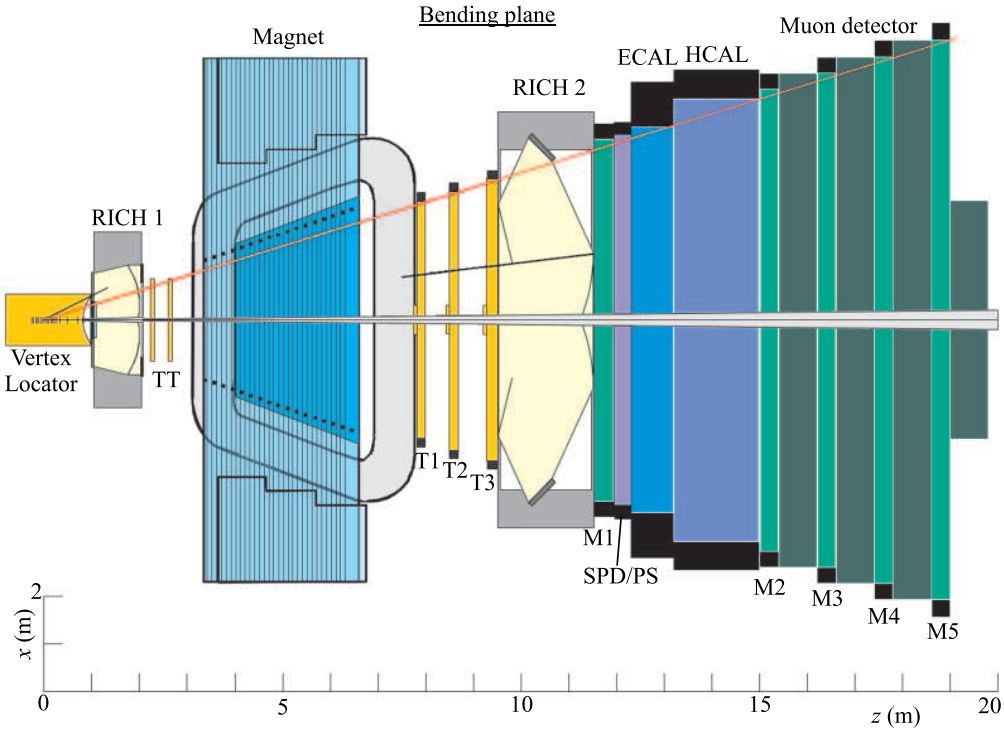

Figure 3.4: *Top view of the LHCb spectrometer with the different sub-detectors. From left to the right: silicon vertex detector (VELO), first ring imaging detector (RICH1), silicon tracker (TT), dipole magnet, tracking stations (T1, T2 and T3), second ring imaging detector (RICH2), first muon detector (M1), scintillating pad detector (SPD) and preshower (PS), electromagnetic calorimeter (ECAL), hadronic calorimeter (HCAL), and four muon detectors (M2 M3, M4 and M5).*

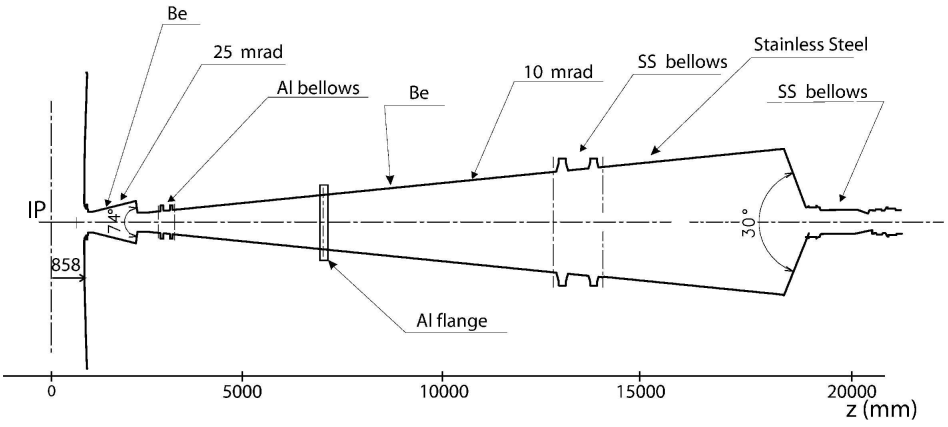

Figure 3.5: *Layout of the LHCb beam pipe. About 70% of the total lenght of the pipe is made of berillium. The bellows and flanges are made of aluminum to reduce the production of secondary particles.*

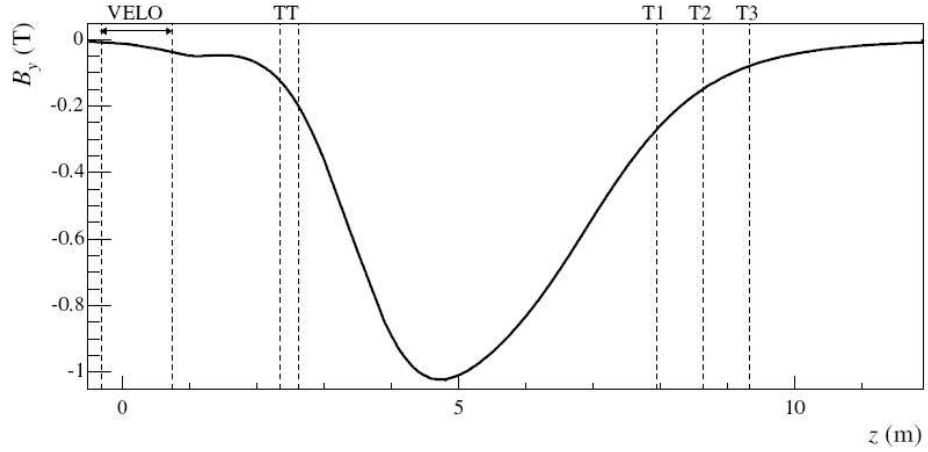

Figure 3.6: *The main component of the magnetic field strength (B_y) along the z axis.*

3.2 Tracking system

The tracking system consist of the VELO and Tracker Turicensis (TT) before the magnet, and the tracking stations (T1,T2,T3) after the magnet (see Fig. 3.4). It is designed to reconstruct charged particle tracks with the associated momentum information, as well as their corresponding primary and secondary vertices.

3.2.1 Vertex Locator (VELO)

The VELO [38] is located around the interaction point and makes use of silicon strip technology. It measures the position of the primary and secondary vertices and provides 3-D tracking to the high-level trigger. It consists of 21 stations placed along the beam axis, as shown in Fig. 3.7. During operation, the stations are placed 8.2 *mm* away from the beam line. Each station consists of two measurement planes: one plane is designed to measure the radial coordinates (r), and the other to measure the azimuthal ones (ϕ).
Two planes placed on the upstream side of the detector act as a Pile-Up veto trigger. Each plane consists of two overlapping sensors. The Pile-Up detector information is used in the Level-0 Trigger to suppress events with multiple proton-proton interactions in a single bunch crossing.

3.2.2 Tracker Turicensis (TT)

The TT [34] is located between RICH1 and the magnet, and makes use of silicon strip technology. It consists of two stations separated by a distance of 27 *cm*; each station in turn consists of two layers, for a total of four layers, with stereo angles

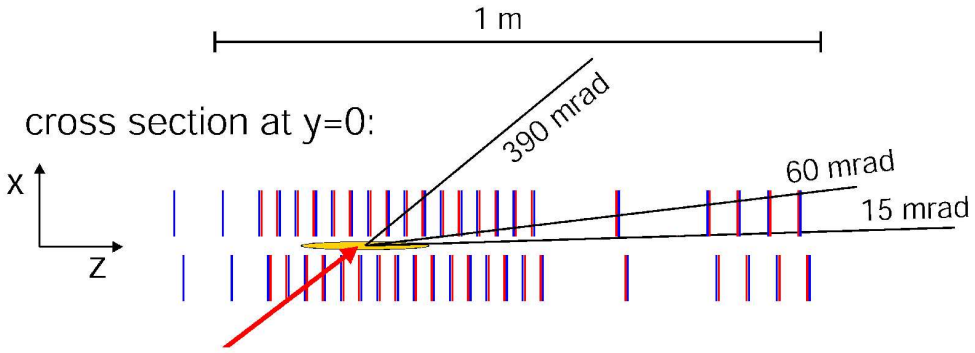

(a) VELO layout

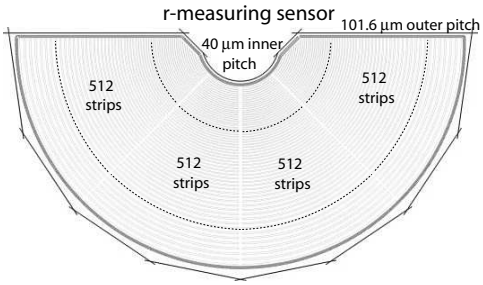

(b) VELO r sensors

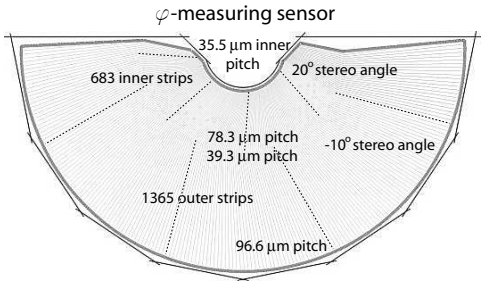

(c) VELO ϕ sensors

Figure 3.7: *(a): Top view of the VELO stations layout. (b) and (c): VELO r and ϕ sensors.*

in the X,U,V,X configuration: $0°, -5°, +5°, 0°$ (allowing a 3D track reconstruction). The sensors are made of 500 μm thick silicon planes ($9.44 \times 9.64\ cm^2$) with 183 μm strip pitch (see Fig. 3.8). The main TT tasks are to provide p_t information to the high level trigger and to reconstruct the trajectories of particles (i.e. K_s), decaying outside the VELO.

3.2.3 Tracking Stations: Inner and Outer Tracker

The three tracking stations T1, T2 and T3 are located between the magnet and the RICH2 covering a surface of about $6 \times 5\ m^2$ per plane. Two sub-detectors, the Inner Tracker (IT) and the Outer Tracker (OT), are used in regions with different particles fluxes.

Inner Tracker (IT)

The IT [39] make use of silicon strip technology and covers the innermost region corresponding to about 20% of the particle flux. The IT layout is shown in Fig. 3.9.

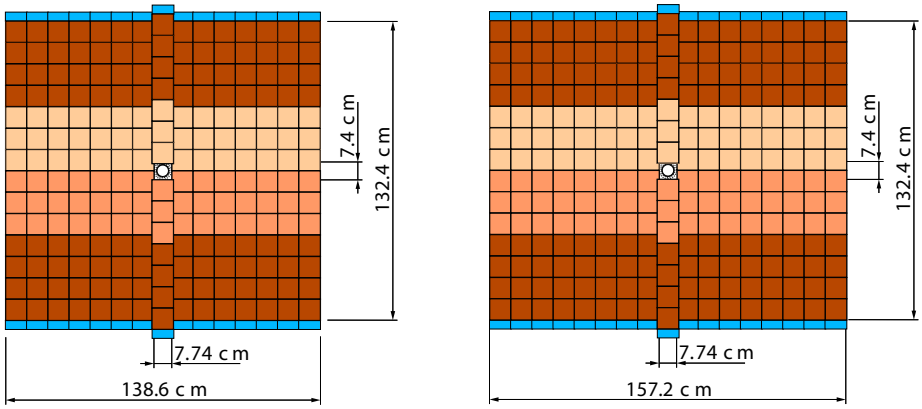

(a) First TT station (b) Last TT station

Figure 3.8: *Layout of the first (a) and last (b) TT stations. The square elements represent the silicon sensors which have a size of 9.44 × 9.64 cm^2.*

The detectors of 7.8 × 11 cm^2 are located in boxes containing double 410 μm thick silicon sensors, and single 320 μm thick silicon sensors, with a strip pitch of 198 μm. In each box, the sensors are arranged in four layers. The layers are in the same X,U,V,X stereo angle configuration as in TT.

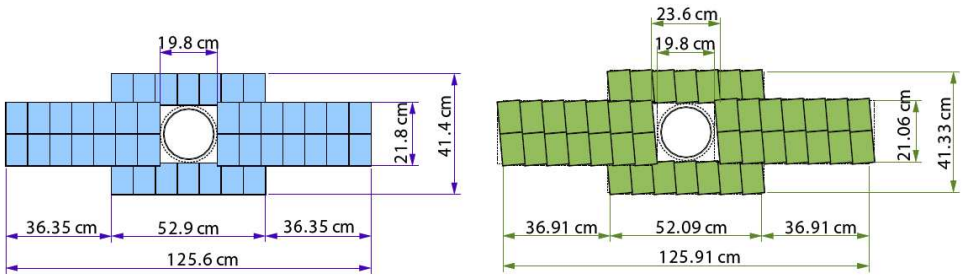

Figure 3.9: *Layout of an IT X (0° stereo-angle) and U (−5° stereo-angle) layer with the silicon sensors in the cross-shaped configuration.*

Outer Tracker (OT)

The Outer Tracker [40] covers the remaining area with straw tubes technology. It is described in detail in Chapters 4 and 5.

3.3 RICH detectors

In most B-decay channels, meaningful CP-violation measurements are only possible if hadron identification is available. The Particle Identification system (PID) allows in particular to separate pions from kaons. This task is performed by the two Ring Image Cherenkov (RICH) detectors [41].

A RICH detector is based on the Cherenkov effect: A cone of Cherenkov light is emitted when a charged particle traverses a "*radiator medium*" with a velocity greater than the speed of light in that medium ($v > \frac{c}{n}$). The RICH determines the velocity v of a particle by measuring the Cherenkov angle, θ_c, *i.e.* the angle between the emitted Cherenkov photons and the particle velocity vector. The following relations holds:

$$\cos\theta_c = \frac{c}{nv}, \tag{3.4}$$

where c is the speed of light and n is the refractive index of the medium. The Cherenkov light cone is detected on a sensitive planar photon detector, allowing the reconstruction of the light ring, the radius of which is a measure of the Cherenkov angle. Combining the deduced velocity with the measurement of the momentum of the traversing particle, its mass can be calculated and the particle identified.

In LHCb three radiator media are required to cover the full range: silica aerogel ($n = 1.03$) for the lowest momenta, gaseous CF_4 for the high momenta, and gaseous C_4F_{10} for the intermediate region. Given the high correlation between polar angle and momentum of the tracks (lower momentum at wider angles), the RICH system was subdivided into two sub-detectors (see Fig. 3.10):

- **RICH1**, located between VELO and TT, is optimized to identify low momentum ($1 \leq p \leq 60\ GeV/c$) particles. Solid aerogel and C_4F_{10} are used as radiator materials.
- **RICH2**, located between the OT and the ECAL, is optimized to identify higher momentum ($p \leq 100\ GeV/c$) particles in the limited 120 $mrad$(horizontal)$\times$100 $mrad$(vertical) region of high-momentum tracks. In RICH2, CF_4 is used as radiator material.

The main parameters of the RICH radiators are summarize in Tab. 3.2. A detailed description of the RICH detectors can be found in Ref. [42].

3.4 Calorimeter System

The main task of the calorimeter system is to identify hadrons, photons and electrons and to measure their energies and positions. The detection of photons enables the reconstruction of B-decay channels containing prompt γ or π^0. This information

	RICH1		RICH2
	aerogel	C_4F_{10}	CF_4
n	1.03	1.0014	1.0005
$\theta_{max}[mrad]$	242	53	32
p range $[GeV/c]$	1-10	10-60	60-100

Table 3.2: *Values of the refractive index n, the saturation angle θ_{max} and the working momentum range of the radiator media used in RICH1 and RICH2.*

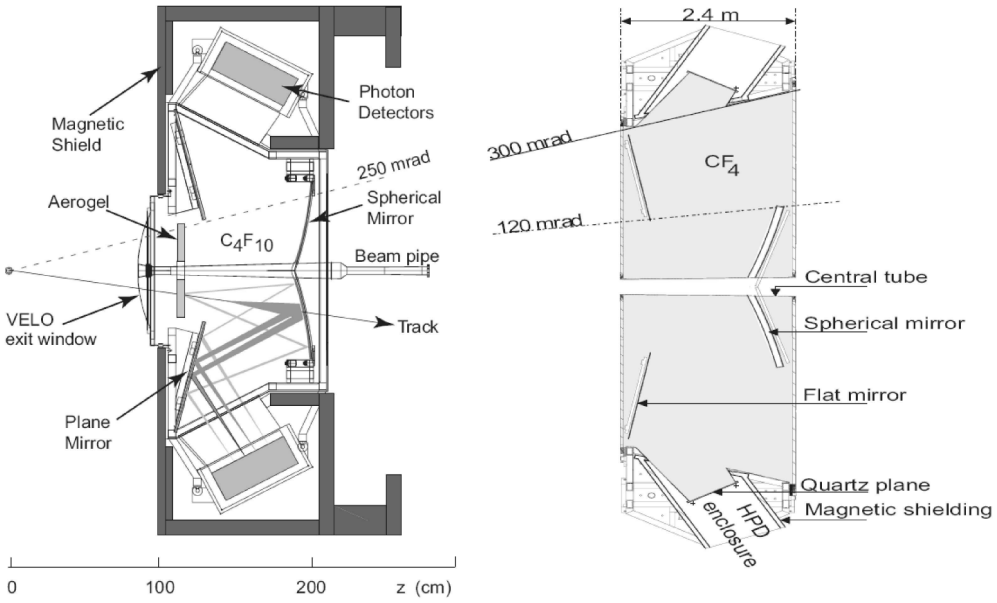

Figure 3.10: *Layout of RICH1 (left) and of the RICH2 (right) detectors.*

is used also in the L0 trigger. The LHCb calorimeter consists of an Electromagnetic (ECAL) and a Hadronic (HCAL) Calorimeter [43]. Two additional detector layers, a Scintillator Pad Detector (SPD), and a PreShower (PS), are placed in front of the ECAL. Each detector is divided into regions with different granularity as shown in Fig. 3.11. The segmentation is increasing with smaller distances from the beam-pipe to adapt for the magnet hit occupancy, while at the same time separating the two showers from high energy π^0. The different detection layers are arranged to obtain optimal particle identification with minimal loss of energy resolution. Electrons and photons start to shower entering the SPD, positioned in front of a 12 mm thick lead wall, allowing a separation between electron and photon showers. The PS detector, behind this lead wall, measures the shower development. Both the SPD and the PS are made of 15 mm thick scintillator pads; the total surface is 6.2 m × 7.6 m. The

total radiation thickness of the SPD/PS detectors is 2 X_0.

The ECAL uses the "*shashlik*" technology with alternating layers of 2 mm lead (Pb) sheets and 4 mm thick scintillators plates together with wavelenght shifting fibers for the light collection. The ECAL electromagnetic showers can be measured with a resolution of:

$$\frac{\sigma(E)}{E} = \frac{10\%}{\sqrt{E}} \oplus 1.5\%, \tag{3.5}$$

where E is expressed in GeV.

The HCAL is an iron-scintillating tile calorimeter read out by wavelength shifting fibers. The scintillators are on average 4 mm thick every 16 mm of iron. The total HCAL thickness is 1.2 m, while the transverse dimension is 6.8 m $\times$ 8.4 m. The resolution is

$$\frac{\sigma(E)}{E} = \frac{80\%}{\sqrt{E}} \oplus 10\%, \tag{3.6}$$

where E is expressed in GeV.

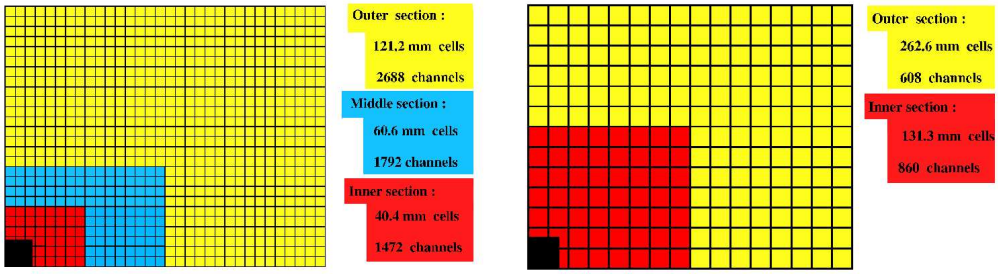

Figure 3.11: *Left panel: Lateral segmentation of the SPD/P and ECAL. One quarter of the front-face is shown. Right panel: lateral segmentation of the HCAL. One quarter of the front-face is shown.*

3.5 Muon System

Muons are present in the final states of many B decays of interest. Also the reconstructed charge of muons in semileptonic B decays is an important tool to determine the flavour of the produced b-quark. Therefore, the Muon system is crucial both in the LHCb trigger and in the offline reconstruction. The Muon system consists of five muon tracking stations (M1, M2, M3, M4 and M5) placed along the beam axis (see Fig. 3.4) and interspersed with "filters" (steel walls) to attenuate hadrons, electrons and photons. The M1 station is placed in front of the calorimeter preshower providing a measurement point evoiding additional multiple scattering in the calorimeters.

The remaining four stations are interleaved with the muon filters at mean positions of z=15.2 m (M2), 16.4 m (M3), 17.6 m (M4) and 18.8 m (M5). The Muon system makes use of two detector technologies: Multi Wire Proportional Chamber (MWPC) and triple Gas Electron Multiplier (GEM) detectors. The latter is only used in the innermost part of M1, the region with the highest particle flux.

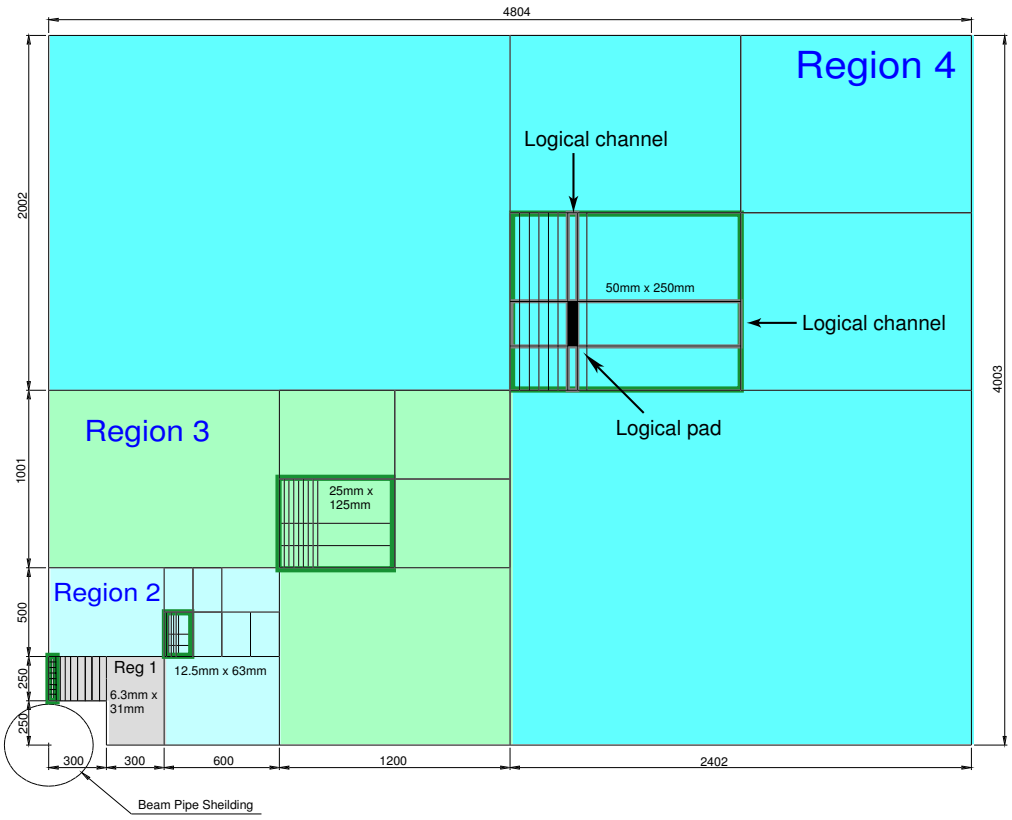

Figure 3.12: *Front view of a quarter of MUON station M2, showing the dimension of the regions. Inside each region, a sector is shown, defined by the size of horizontal and vertical strips. Dimensions scale by a factor two from one level to next.*

3.6 Trigger

At the nominal instantaneous luminosity of $2{\times}10^{32}\mathrm{cm}^{-2}\mathrm{s}^{-1}$ events containing a $b\bar{b}$ pair are produced at a rate of 100 kHz, assuming a production cross section of $\sigma_{b\bar{b}} = 500\ \mu barn$. However, the branching ratios of the interesting B decays are typically of the order of 10^{-4} or less. Therefore, a trigger is needed to ensure that only events of interest are selected and stored for offline analysis. LHCb has only two trigger levels: Level-0 (L0) and an High Level Trigger (HLT), bringing the event rate down to 2 kHz, as outlined in Fig. 3.13.

L0

The L0 reduces the LHC beam crossing rate of 40 MHz to the 1 MHz rate established for the readout of the FE-electronics of the entire detector. The L0 trigger is fully implemented in hardware with a fixed latency of 4 μs. B mesons have a lifetime of about 1.5 ps and their decay products have a high transverse momentum p_t. ECAL and HCAL are used to determine the highest E_{T} hadron, electron and photon clusters in the Calorimeter; the muons stations are used to select the highest p_{T} muons, and the Pile-Up to reject high multiplicity events from multiple pp interactions. Hadronic, electronic and muonic channels are selected with efficiencies of about 50%, 70% and 90%, respectively [44].

HLT

The HLT algorithms run concurrently on 2000 CPU nodes and have access to the full event data. The HLT is split in:

- **HLT1:** tracks in the VELO and the T-Stations are reconstructed.
- **HLT2:** B decays are partially or totally reconstructed (using inclusive and exclusive trigger algorithms). After the HLT2, the data contains only events of physics interest.

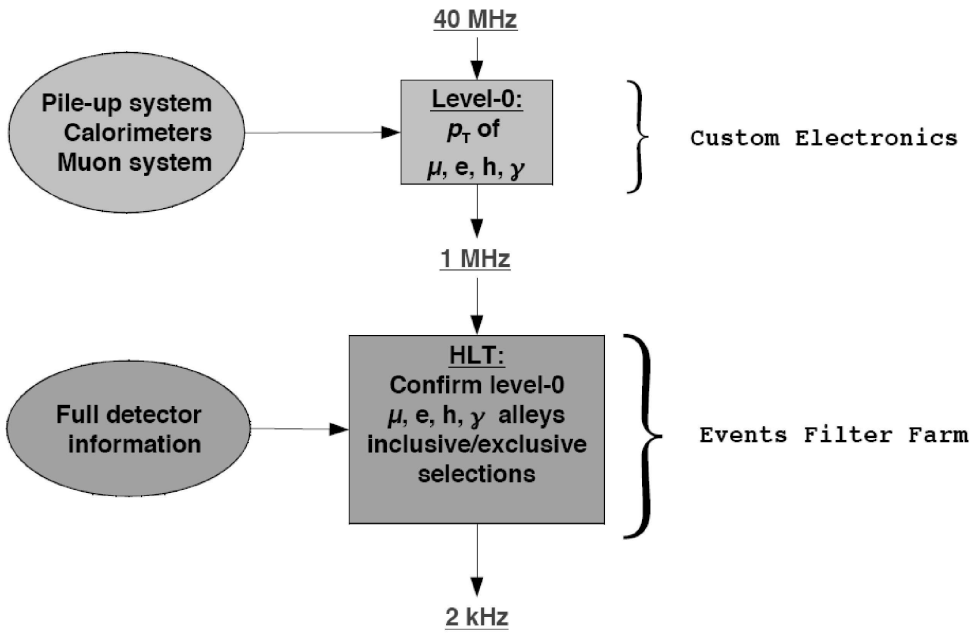

Figure 3.13: *Outline of the LHCb two-levels trigger system.*

3.7 Outlook

To perform the $B_s \to \mu^+\mu^-$ measurement, a copious source of B mesons is needed. LHC is the most powerful pp collider ever built, it accelerates proton bunches in opposite directions in a ring of 27 km circumference. Protons will collide every 25 ns at a center-of-mass energy of 14 TeV producing $b\overline{b}$ pairs in a forward and backward cone along the beam axis. The LHCb tracking system efficiently reconstructs charged tracks, measures primary and secondary decay vertices providing precise particle momentum measurements. The Tracking Stations (T-stations) measure the momenta of charged particles with a nominal momentum resolution ($\Delta p/p$) of about 0.5% in the momentum region from 2 to 100 GeV.

Chapter 4

Outer Tracker

In a typical B event on average 110 charged particles tracks are reconstructed in the LHCb acceptance (see Fig. 4.1(a)). These particles must be efficiently detected and have their momentum measured. The LHCb Outer Tracker is a gas detector made of 53760 drift cells built out of straws tubes, ordered in 24 layers of typically 2.5 m long straws and covering a surface area of $6 \times 5\ m^2$ per layer. The primary and secondary particles produced leave an average of 2400 hits in the OT (see Fig. 4.1(b)). The detector was designed such that in the hottest region the occupancy stayed below 10%, resulting in an efficiency for reconstructing long tracks higher than 90% [46]. MC studies [47] showed that an intrinsic spatial resolution of 200 μm leads to a typical momentum resolution of $\frac{\delta p}{p} \approx 0.5\%$ and a resulting mass resolution for reconstructed B mesons of about 20 MeV.

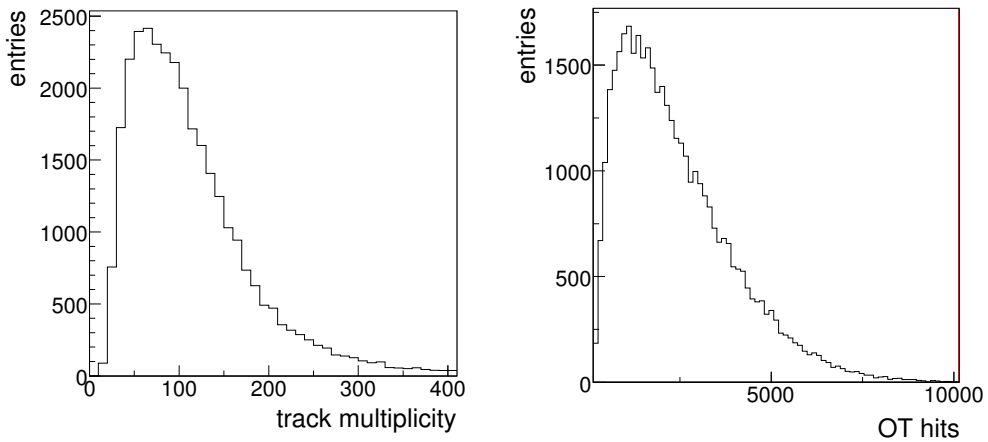

(a) (b)

Figure 4.1: *Distribution of charged particles track multiplicity (a) and the number of OT hits (b) observed in 40000 $B_d \to \pi\pi$ events.*

4.1 Outer Tracker straw tube

The Outer Tracker modules are drift-chamber detectors based on straw tube technology. They are made out of cylindrical cells with an anode (wire) under positive high voltage (1600 V, proportional regime) and a cathode (straw) connected to ground. The counting gas is a mixture of Argon (30%) and Carbon Dioxide (70%). The anode wire is made of gold-plated tungsten (4-6% gold) of 25.4 μm diameter. The straws are cylindrical tubes of 2.45 mm radius, about 2.4 m long, made of an inner layer of carbon-doped Kapton of 40 μm, and an outer layer of a thin laminate (25 μm polyimide and 12 μm aluminum).

The working principle is shown in Fig. 4.2. A charged particle crossing the straw ionizes the counting gas. The electric field between the anode and the cathode drives the resulting free electrons toward the anode wire and the heavier ions toward the cathode. While the ions slowly drift toward the cathode, the electrons quickly gain kinetic energy, and when they reach the ionization potential of the counting gas, free more electrons generating an electromagnetic avalanche. The combined movement of the large number of charged particles induces a measurable electrical pulse in the anode wire. The time of occurrence of this pulse provides the drift time, which in

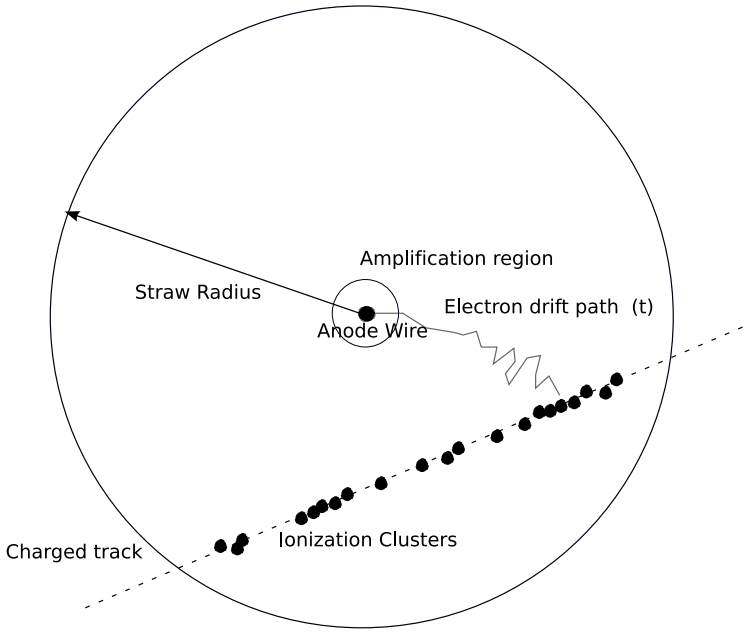

Figure 4.2: *Drift cell working principle.*

turn is related to the distance between the wire and the closest ionization cluster. All measured times are relative to the interaction clock of the LHC machine and must be corrected to account for the time of flight of the particle in the spectrometer, the time the signal needs to propagate along the wire and finally the delay time due

to the readout electronics. A typical drift time spectrum is shown in Fig. 4.3. It

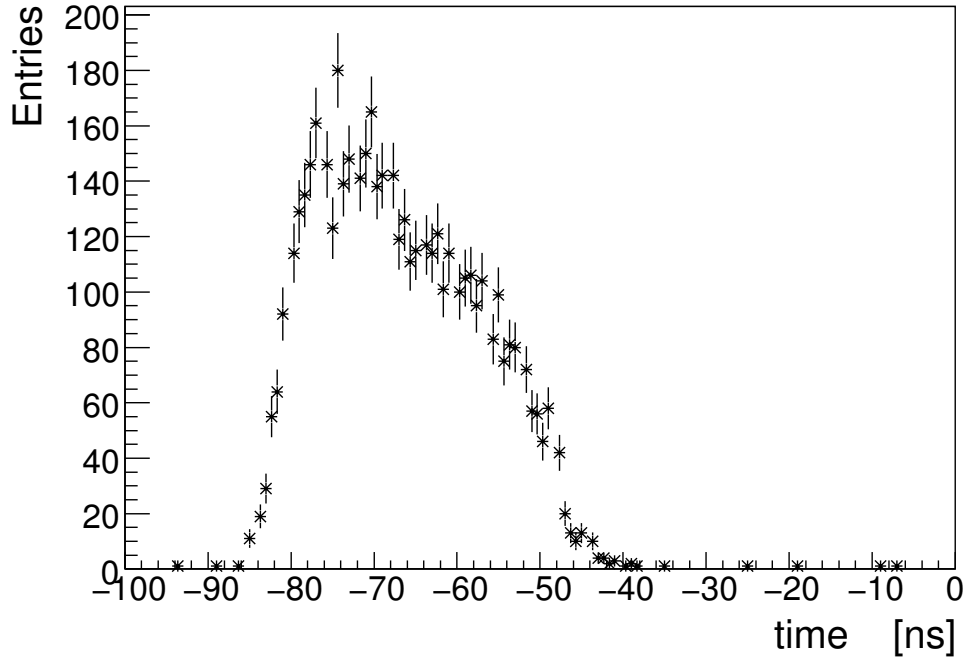

Figure 4.3: *Drift time distribution of an OT straw drift cell. This distribution was obtained using low energy (up to 2.4 MeV) electrons from a 2 mCi ^{90}Sr placed at the far end of the module (240 cm from the preamplifier) with 30% Ar and 70% CO_2 counting gas at 1600 V.*

is about 40 *ns* wide; since the LHC bunch crossing frequency is 25 *ns*, the readout electronics was designed to detect hits in a window of up to three bunch crossing.

4.2 Geometrical layout of the OT

The OT has a modular design. The straws are arranged in modules containing two staggered layers of 64 straws as shown in Fig. 4.4. Each straw layer is glued to a panel built from a 10 *mm* core of Rohacell foam, covered on both sides by a thin laminate (25 μm polymide and 12 μm Aluminum) and a skin of Carbon composite with a thickness of about 90 μm. The two straw mono-layers are finally joined to form a module and sealed using carbon-fibers strips as side walls. The total estimated radiation length of a module is $X/X_0 = 0.74\%$ [48]. Each module has four gas pipes at both ends.

The OT modules were built in four different types: F, S1, S2 and S3, with the characteristics listed in Tab. 4.1. The modules are organized in 3 stations, each consisting of four layers: X(0°), U(−5°), V(+5°), X(0°). The X layers provide a

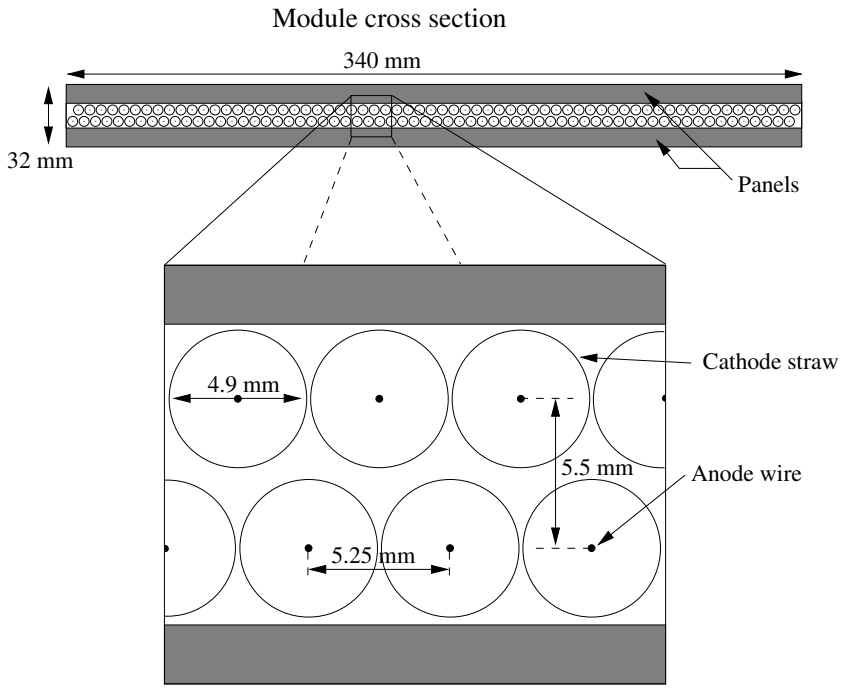

Figure 4.4: *Cross section of an OT module.*

direct measurement out of the magnet bending coordinate, while the stereo layers (U and V) allow track reconstruction in 3 dimensions. In a layer the modules are arranged as shown in Fig. 4.5. Each OT module is fixed to a metallic support

Module type	Size (mm)	#Channels	Amount
F	4900×340×32	256	168
S1	2375×340×32	256	24
S2	2275×340×32	256	12
S3	2275×170×32	128	12

Table 4.1: *Straw modules characteristics.*

structure (C-Frame) by means of two dowel pins. Each OT layer is split onto two C-Frames, movable independently on either side of the beam pipe. The C-Frames provide also services (water cooling, gas system etc.). They are fixed to a stainless structure (bridge) between the magnet and the RICH2, as shown in Fig. 4.6.

4.3 OT module production

The straw-tube modules were produced in three production sites. This required the production procedure to be standardized and stringent quality checks to be put

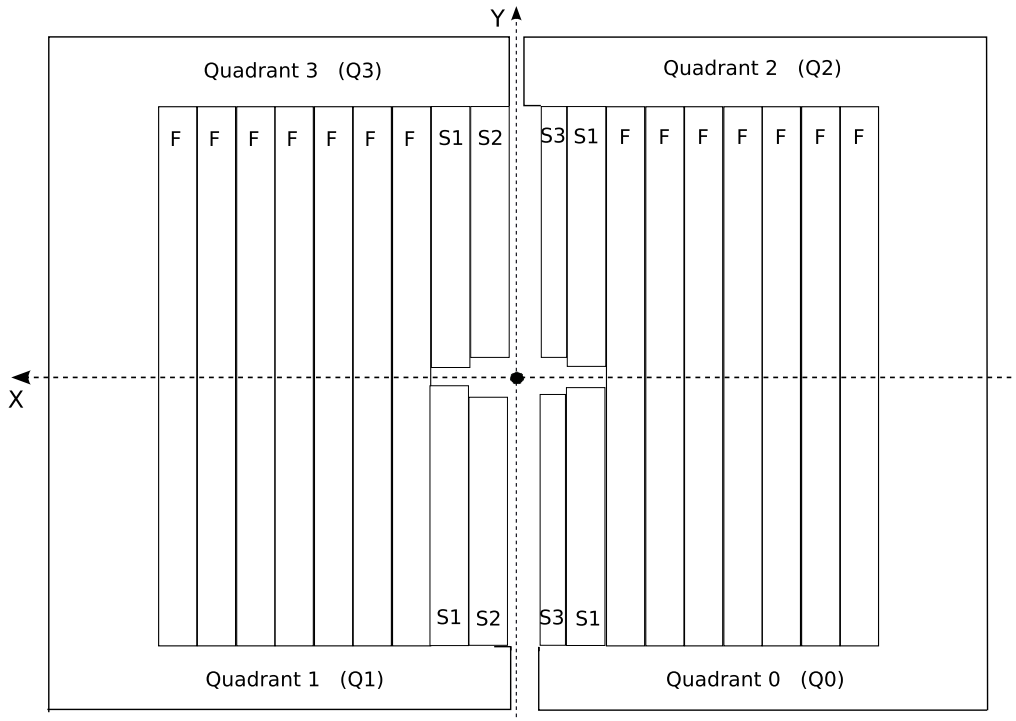

Figure 4.5: *Outline of the first X layer of the T1 station supported by 2 C-Frames (view from the VELO sub-detector).*

in place. The Outer Tracker module production sequence can be summarized as follows:

- Straw tubes were cut to the proper length and ground contacts were crimped to one straw tubes end.
- Straw tubes were aligned with a precision jig and equipped with wire-locators every 80 *cm*. The wire locators keep the wires centered. At the straw tube ends, end-pieces were inserted to align the wires and to ensure a proper flow of the counting gas in the straw.
- Once aligned on the jig, the straws were glued to a light support panel forming a mono-layer. The straw tubes ground contacts were soldered to feed-through boards.
- The straw tubes were equipped with anode wires. For each wire the position, mechanical tension and current under high voltage were measured as part of the quality control procedure (see Sec. 4.3.1). Wires that do not pass the quality criteria were replaced.
- Two mono-layers were then glued together and sealed with a carbon-fiber side wall.

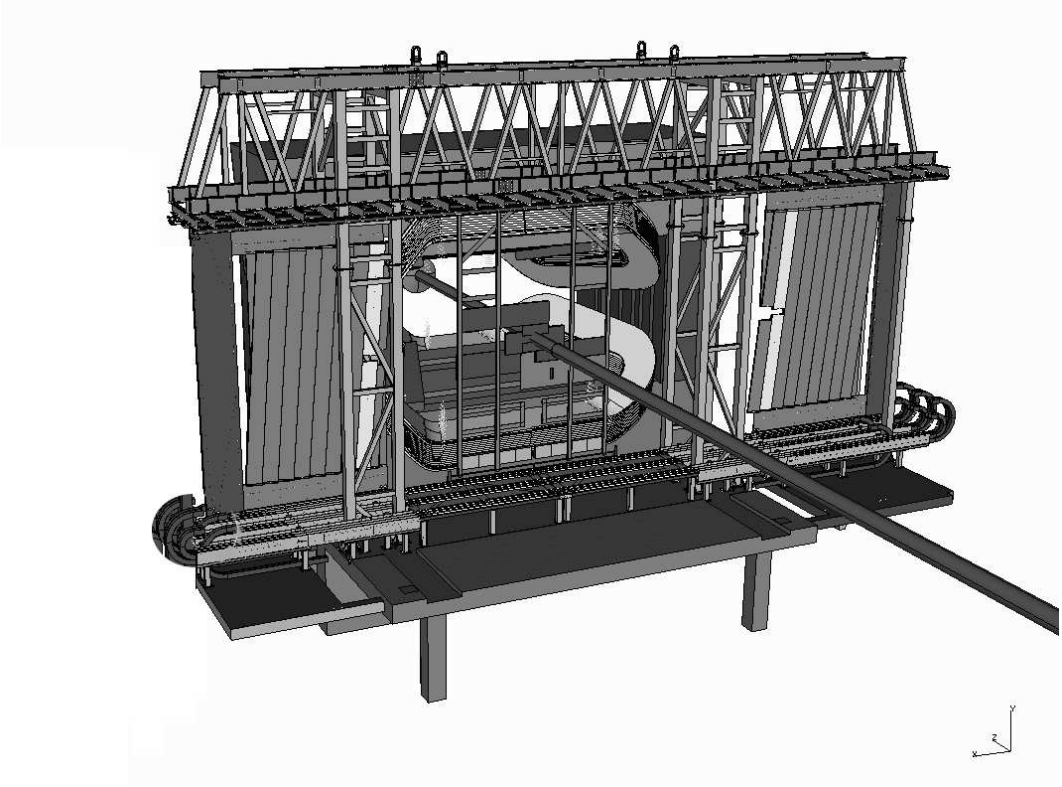

Figure 4.6: *Overview of the OT Detector, showing the bridge supporting the C-Frames equipped with straw-tubes modules. The detector is displayed in the open position, such that the magnet region and the Inner Tracker modules can be seen.*

4.3.1 Tests during production

Testing during production has to be quick and should spot major problems related to the quality of the incoming material and the production procedure.

Wire tests

Every spool of wire (1000 m) was sampled at three points in the first 30 m of wire. Each sample of 10 cm was visually checked under an optical microscope to spot surface defects (lack of gold, sharp edges etc.). Before being soldered, wires were stretched by a fixed weight of 75 g. The tension was checked after soldering by a wire tension meter. This was done by injecting an electric signal on the wire and measuring the resonance frequency of the wire in a magnetic field [50].

High voltage tests in air

To spot broken wires or shortcuts before gluing two mono-layers together, a voltage of 50 V was initially applied to the wires. The voltage was slowly raised in steps of 50 V up to 1000 V and in steps of 100 V from 1000 V to 2000 V. If the current

exceeded 20 nA at 1600 V, the corresponding wire was replaced. Typically, one or two wires per module were replaced.

4.3.2 Tests after production

Tests on a newly born module were are aimed at guaranteeing its functionality under HV as well as its gas tightness.

High Voltage training

Before applying the nominal 1600 V, the modules were first flushed (1 volume/hour), with the counting gas for at least 12 hours then the HV was slowly increased up to the nominal 1600 V. The current was monitored every 20 seconds on each channel. The high voltage was continuously applied (typically for 1.5 h), until the current was about few nA (in few cases, initial currents could go up to few hundreds of nA). This training procedure guarantees a stable low dark current during operation.

Validation using a scan with a radioactive source

The response of each straw tube to a radioactive source was checked with a ^{90}Sr source, to find non-uniformities of the drift cell response due to shifted or missing wire locator, deformed straws etc. The emitted electrons have sufficient energy (up to 2.24 MeV) to traverse the straw tubes inside the module and ionize the counting gas resulting in a current per wire of about 100 nA. Each module was irradiated in steps of 1 cm along its entire length. A typical module response (the current of each channel, proportional to the straw-tube gain, after source profile correction), is shown in Fig. 4.7. For most of the surface the gain variation is within a few percent, whereas variation of $\pm 20\%$ can be accepted for good modules. All data collected were stored for future reference.

Gas tightness

The module has to be gas tight to avoid contamination and losses larger than 10% of its volume per hour [51] (for an F module the maximum allowed leak rate is 2.5×10^{-4} l/s). First an overpressure of 7 $mbar$ of Argon was applied to the module; then by observing the overpressure decay after three minutes, large leaks were eventually located and repaired by using an argon sniffer. As a second step, a precise measurement of the leakage rate was done filling the module with nitrogen against an overpressure of 7 $mbar$, and monitoring the gas flow with a precise flow meter.

4.4 Support Frames

As described in Sec. 4.2, all straw tube modules are supported by metallic C-Frames, providing also the interface to the detector services (cooling, gas, slow and fast

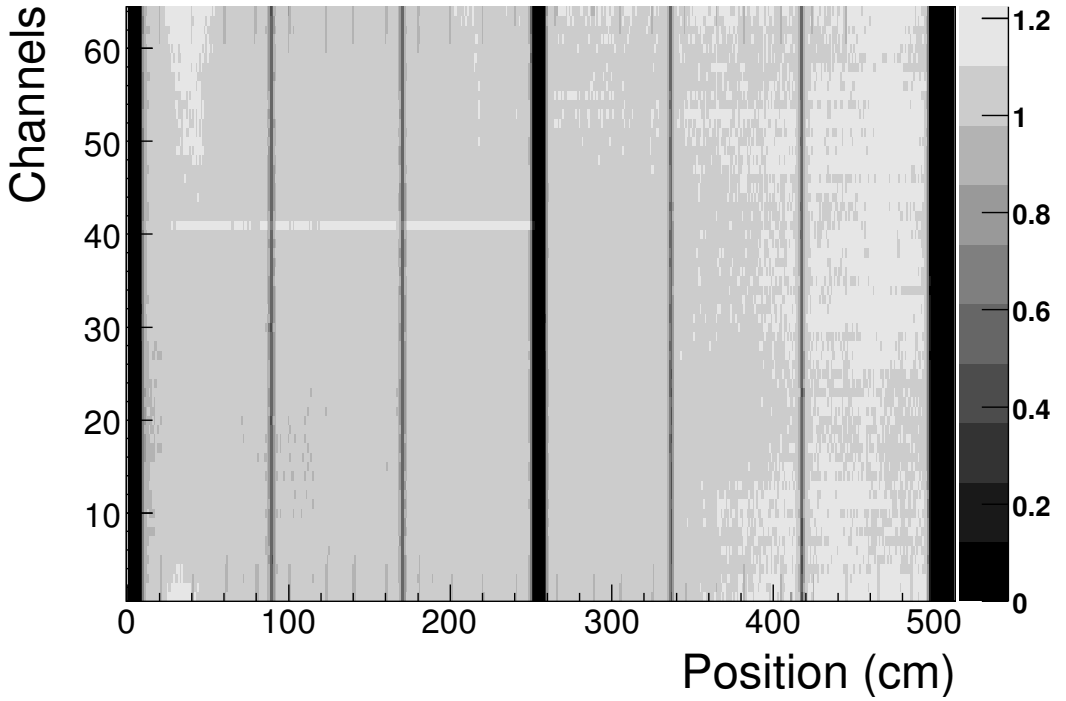

Figure 4.7: *Result of a scan with a radioactive source of a module mono-layer (F module 17B, Oct 18 2004). The grey scale shows the module response in arbitrary units (after source profile correction [51]). The black areas corresponds to low gain regions due to the presence of the wire locators and the wire-splitting board. In this example wire 41 of the left module half shows a high current.*

control, etc.). There are 12 C-Frames, 6 on each side of the beam pipe (see Fig. 4.5). These 12 C-Frames were pre-assembled at Nikhef (see Fig. 4.8). During the pre-assembly electrical and optical cables, water cooling and gas pipes were installed and tested. Those tests were eventually repeated at CERN during the installation in situ.

4.4.1 C-Frame Quality Assurance

The services installed on the C−frame are:

1 High Voltage (HV) to the anode wires.

2 Timing and Fast Control (TFC) and Experiment Control System (ECS).

3 Optical fibers to transfer the serialized drift−time data to the TELL1 boards.

4 RASNIK Alignment system.

5 Low Voltage (LV) to bias the Front End electronics.

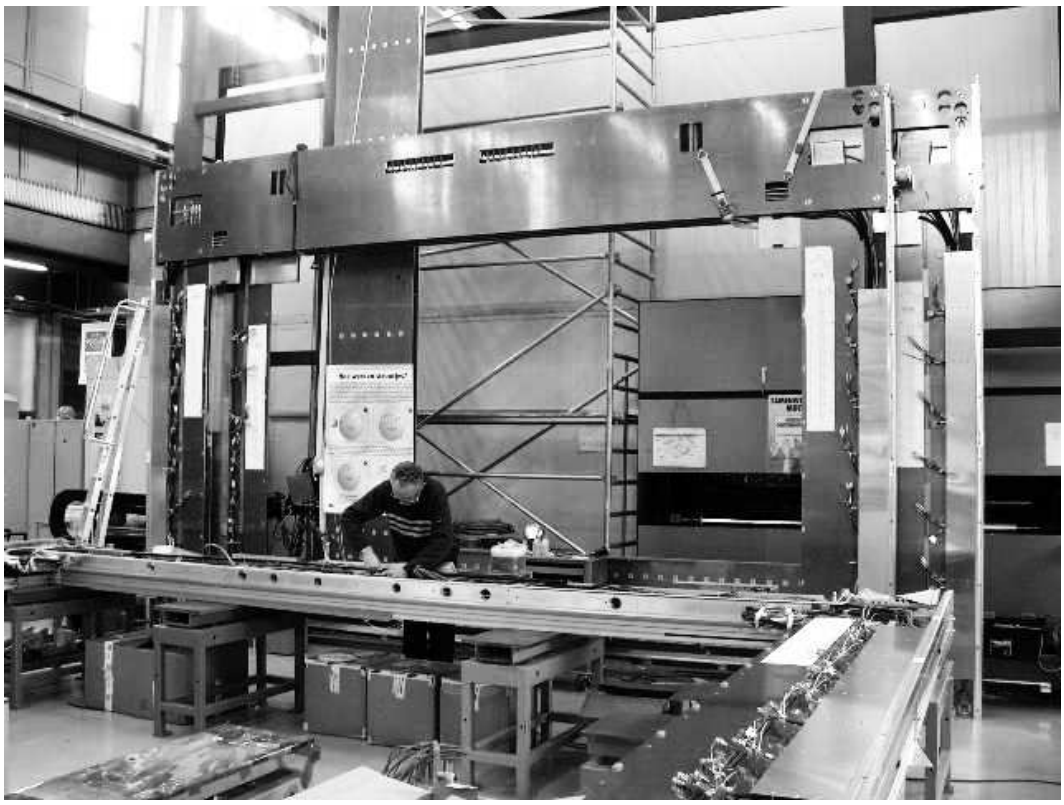

Figure 4.8: *Photograph of the C-Frame assembly hall at Nikhef.*

6 Gas System.

7 Cooling system.

All cables, fibers and pipes have been individually tested after manufacturing. A final global system check was performed in order to exclude any damage, miscablings, etc. due to the pre-assembly. The main goals were to verify that the whole distribution (patch panels, manifolds etc.), works correctly and that the mapping of cables, fibers and pipes is as expected. The services 1 through 4 are patched onto a panel, as shown in Fig. 4.9.

HV Test

On each C-Frame HV is supplied through four multi-pole connectors (52 pins) located on the patch panel. From there, multi-wire cables route the HV to "junction boxes" from where they are further routed to the FE-Boxes via cables of type RG59 ending with Safe High Voltage connectors (SHV). To check the routing from the single pins on the patch panel to the SHV connectors, a resistivity measurement was performed.

Figure 4.9: *C-Frame patch panel showing from left to right two ECS connections (SPECS through CAT6), two TFC optical connections, four output data fibers, four RASNIK lines and four multi-pole HV input connectors.*

LV Test

Each C-Frame is supplied by six LV lines: four carrying $+6V$ and two $-6V$. From the input terminals, they are routed to two LV distribution boxes. The LV distribution boxes fan out the positive and negative bias to the FE-Boxes. All LV lines were individually tested.

Optical Data Fibers

Each FE-Box produces data in an optical serial protocol (see Sec. 5.1.5); the FE-Box data output consists of a female Sub Miniature version A connector (SMA). The data from 9 FE-Boxes, at the top or bottom of a C-Frame are grouped through breakout fibers, coupling individual fibers with male SMA connectors into a ribbon cable ending with a male Multi-fiber Push On connector (MPO, see Fig. 4.10). The four outputs are patched onto the C-Frame patch panel with female-female MPO connectors. Each fiber was fully tested by the manufacturer. In addition, the light attenuation in each fiber was measured at Nikhef quantifying it as the power loss in [1]dBm for 850 μm light and a precision of 0.2 dBm. For a good fiber, the measured attenuation was in the range of -15 to -20 dBm. Few fibers with larger attenuations were replaced.

[1] dBm indicates the power ratio in decibels (dB) of the measured power, referenced to one milliwatt.

(a) SMA connector

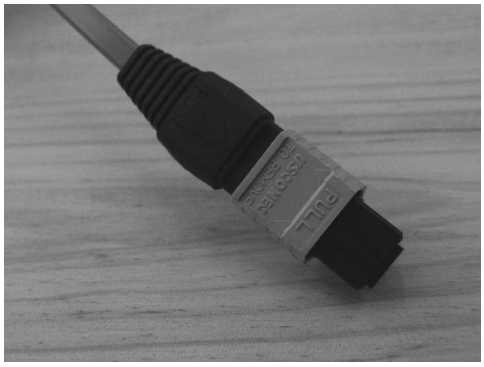

(b) MPO connector

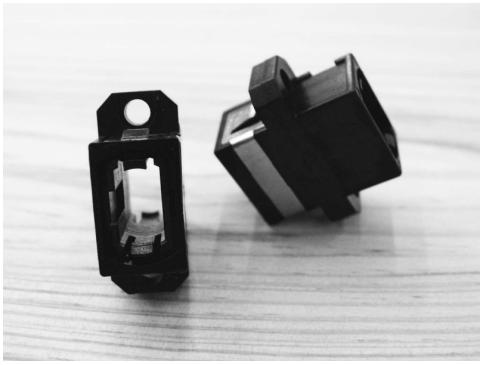

(c) MPO junction

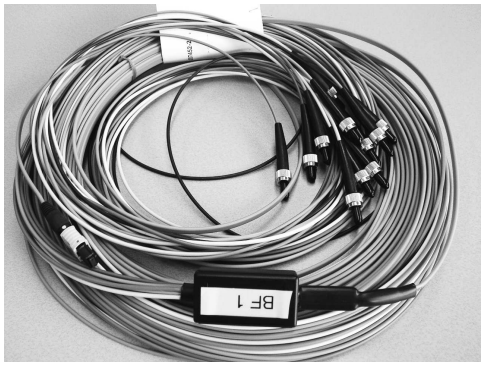

(d) BF fibers

Figure 4.10: *Fiber connectors. Female SMA (a) and male MPO (b). MPO junction (c) and break-out fiber (d).*

4.4.2 Test of the C-Frame prototype with mass production modules

A prototype of the LHCb Outer Tracker C-Frame, equipped with mass production detector modules, was built at Nikhef in 2005. Several tests were performed, in order to probe the engineering of the detector as a whole and the functioning of the readout chain, mimicking the experimental conditions. As a final test, the detector response to a radioactive source was measured with a prototype of FE electronics. Several tests were done with a 2 mCi ^{90}Sr in combination with a scintillator of 15x25 cm^2 as trigger. Drift time histograms were produced and clusters of hit straws were identified. Cross-talk was also measured at several positions along the module, and for different voltages applied. At 1600 V, a cross-talk of 3-7% was measured, compatible with the measurements done during the OT beam tests [52]. The tests with the ^{90}Sr source went on for about three weeks. A reduction of the analog signal was observed as shown in Fig. 4.11(a). This was later investigated

with the module scanning setup (see Sec. 4.3.2), which revealed several spots with lower amplification corresponding to the positions in which the source was placed as shown in Fig. 4.11(b). This triggered a series of dedicated aging studies, discussed in detail in the next section.

4.5 Aging of the OT

The OT modules were designed to withstand an equivalent irradiation dose of 10 years of LHC operation. This was confirmed by a series of R&D studies and tests performed with various high-intensity radioactive sources (9 keV X-rays, 11 MeV protons, etc.) [54, 56, 57]. However, the modules from mass production were found to suffer from gain losses after irradiation by a ^{90}Sr source: tests made with low intensity sources (2 mCi ^{90}Sr) [53] showed that the amplification degrades relatively rapidly when exposed to irradiations corresponding to currents of few nA/cm.
Fig. 4.12 shows that the higher damage is obtained by using a source intensity which produce a current of a few nA/cm.

The method adopted for the aging studies is based on the same scanning setup used to commission the modules (see Sec. 4.3.2). A first scan is done prior to irradiation. After irradiation, a second scan is done to measure the gain loss. By taking the ratio of the current responses measured before and after irradiation, a map like the one shown in Fig. 4.13 is obtained, corresponding to 20 hours irradiation time with the source at a distance of 2 cm from the detector surface (the dose directly under the source corresponds to 4 mC/cm). Although a spherically symmetric source is used, the aging pattern shows a half-moon shape. This is correlated with the direction of the gas flow: the damaged area is located upstream of the source position. This feature has not, to the best of our knowledge, been reported in the existing literature.

4.5.1 Overview of the tests performed

Since its observation in 2005 (see Sec. 4.4.2), extensive studies to understand the OT aging mechanism were carried out.

Wire inspection

Samples of damaged wire were investigated with an electron microscope. The surface of a non-irradiated wire is smooth (comparable to that of an unused wire). On a damaged wire (see Fig. 4.14), a thin (<1 μm) insulating layer was observed on the wire surface. From spectroscopy analysis, carbon was identified as the main polluting component, in combination with hydrogen (indirectly detected).

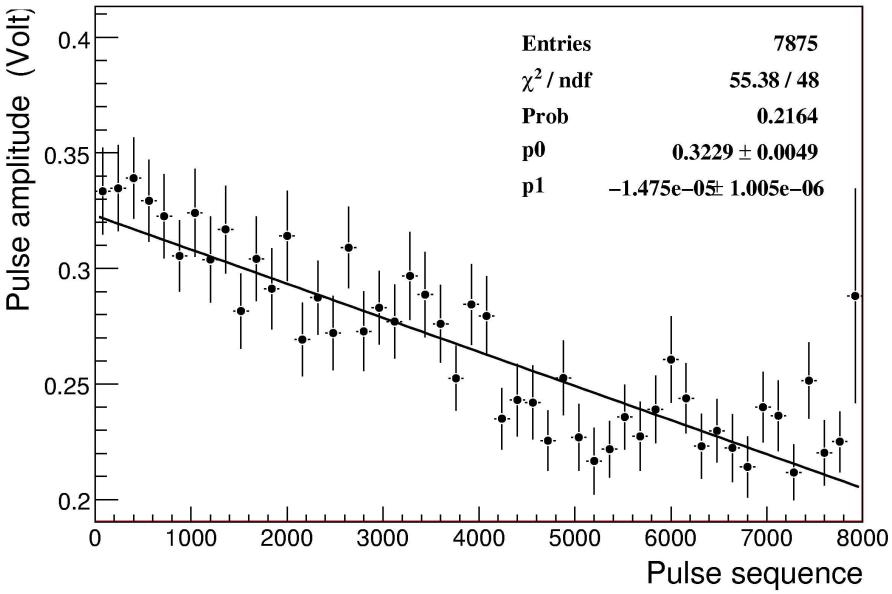

(a) Decrease of the average pulse height.

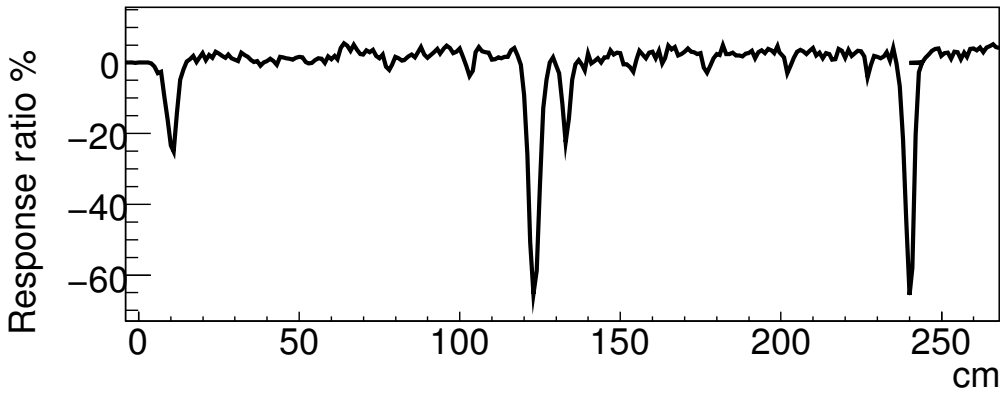

(b) Dips in the wire response

Figure 4.11: *(a) Average pulse amplitude versus pulse sequence (ordered in time), showing the average pulse height decreasing during the C-Frame system test. Each point corresponds to the average of 160 pulses. (b) Dips given by the ratio % of the wire response before and after irradiation. The observed dips correspond to the position in which the 2 mCi ^{90}Sr source was placed. The area of the dips are proportional to the irradiation time.*

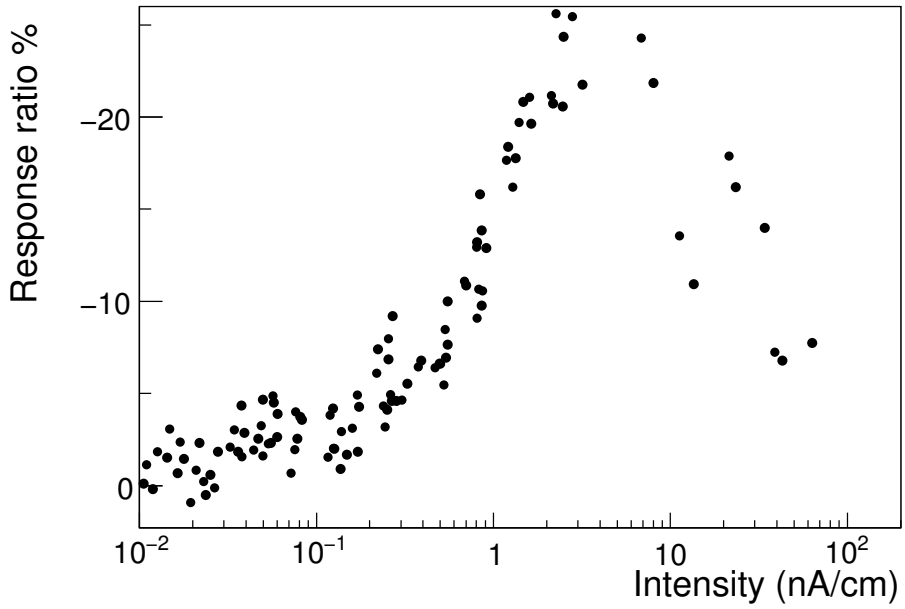

Figure 4.12: *Ratio % of a wire response before and after irradiation, versus intensity of the irradiating 20 mCi ^{90}Sr.*

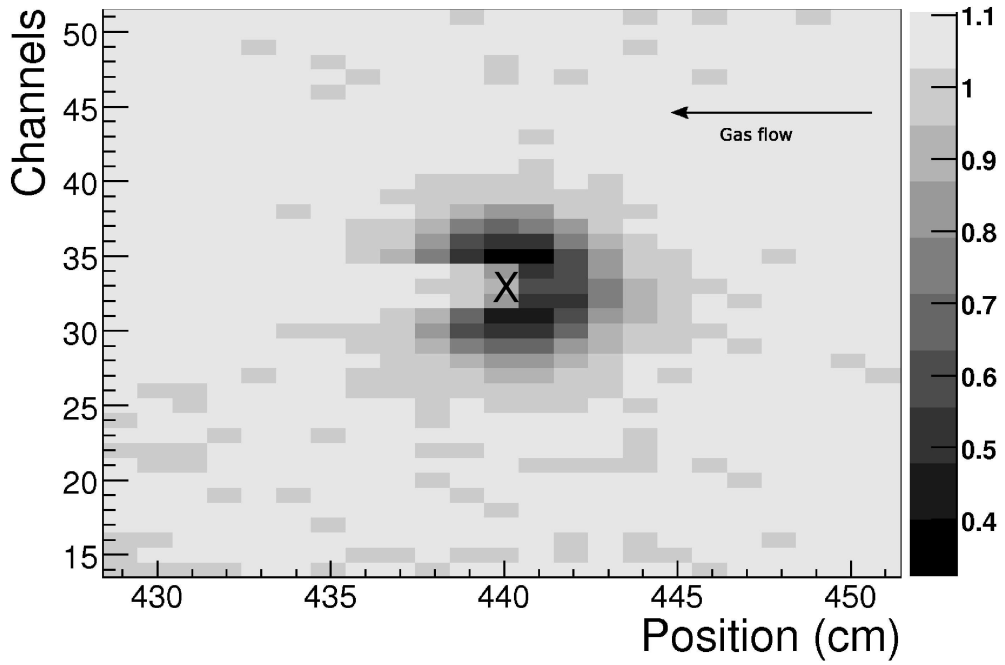

Figure 4.13: *An example of OT aging pattern. The 2 mCi ^{90}Sr source was located above wire 32 at position 440 cm. The gas flow goes from right to left. The grayscale represent the ratio between the current response after and before irradiation.*

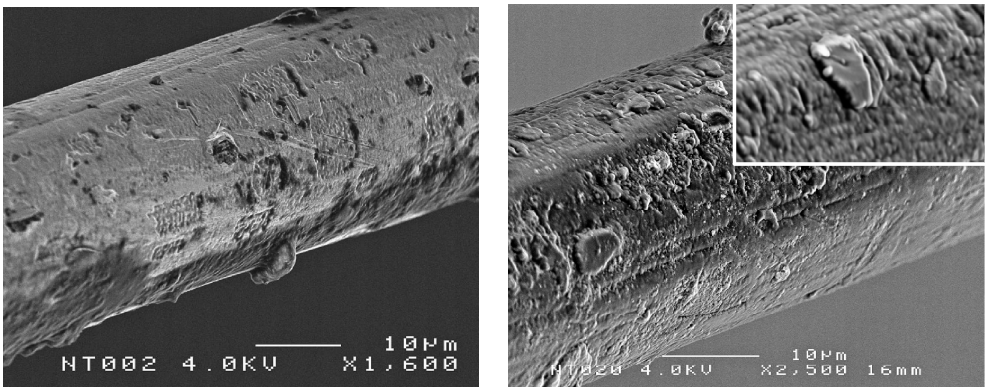

(a) Before irradiation (b) After irradiation

Figure 4.14: *Left panel: SEM image of an un-irradiated wire. Right panel: SEM image of an irradiated wire showing depositions. In the upper right corner, a zoom-in is shown.*

Gas flow and mixture

The aging develops preferentially upstream of the gas flow. The asymmetry is lost if the aging test is performed in the absence of gas motion. If the gas flow is increased, then higher gain losses are produced. At the same time, flushing helps to transport the products of chamber material outgassing out of the module; modules that were flushed for longer times were observed to be more aging resistant. In Fig. 4.15 the gain loss is studied as function of the flushing time. Due to its beneficial effect, the modules have been flushed continuously since their installation in 2007.

HV training

Damaged spots were recovered with an HV training process, applying a high HV setting of $\approx$1900 V, resulting in a dark current of the order of 10 μA per wire (about 100 times larger than the maximum current expected from incident particles at LHCb operation at the nominal HV of 1550 V). In Fig. 4.16(a) a heavily damaged spot (gain loss up to 80%) is shown. The HV training was then applied on the upper half of the damaged spot (from wire 33 through 64). The result is shown on Fig. 4.16(b): several wires were fully recovered while two wires remained affected by the gain loss. The "cure" is not permanent: under irradiation aging effects are again visible (albeit after an "immunity" period of about 200 hours). Presumably, the high currents sputter the deposits off the wire. HV training can be a feasible method to remove existing aging damages (and possibly temporarily prevent new aging). The high current was shown not to affect the wire surface by inspection with the electron microscope.

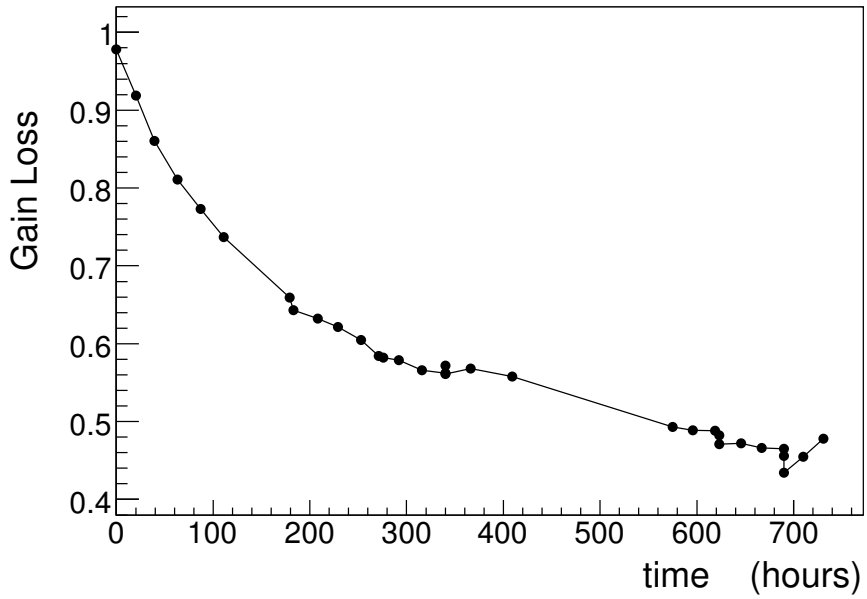

Figure 4.15: *Gain loss in 20 h irradiation with a 2 mCi ^{90}Sr source versus flushing time.*

Oxygen

A counting gas with respectively 1%, 2.5% and 4% of oxygen, was tried and observed to reduce the aging rate by a factor 2 in all three cases [58]. The small loss of signal can be compensated by a small increase of the applied HV ($\approx 20\ V$).

4.5.2 Aging mechanism

In wire chambers, ionizing particles produce local electron avalanches, which can interact with the surrounding material or gas creating chemically reactive radicals in the gas. Radicals can recombine or react with the anode (wire) and the cathode (carbon), or produce insulating deposits. Dedicated tests done with a special openable test chamber [59], showed that no aging is observed using a module built without glue. This observation, combined with the tests described in the previous section (and others described in detail in [54, 56, 57]) led to the conclusion that the glue (ARALDITE AY103-1 resin in combination with the HY901 hardener) used to construct the OT modules suffers from a small out-gassing (total mass loss <1%) nevertheless sufficient to pollute the gas mixture and cause the insulating deposits on the wire. The half-moon shape of the measured gain damaged could conclusively be ascribed to the production of ozone (O_3) in the highest intensity irradiation area (directly under the source): the beneficial effects of ozone preventing the insulating deposits on the wire is then "felt" downstream of the gas flow (ozone survives for about 20 min, roughly corresponding to a transport length of 1 meter in the

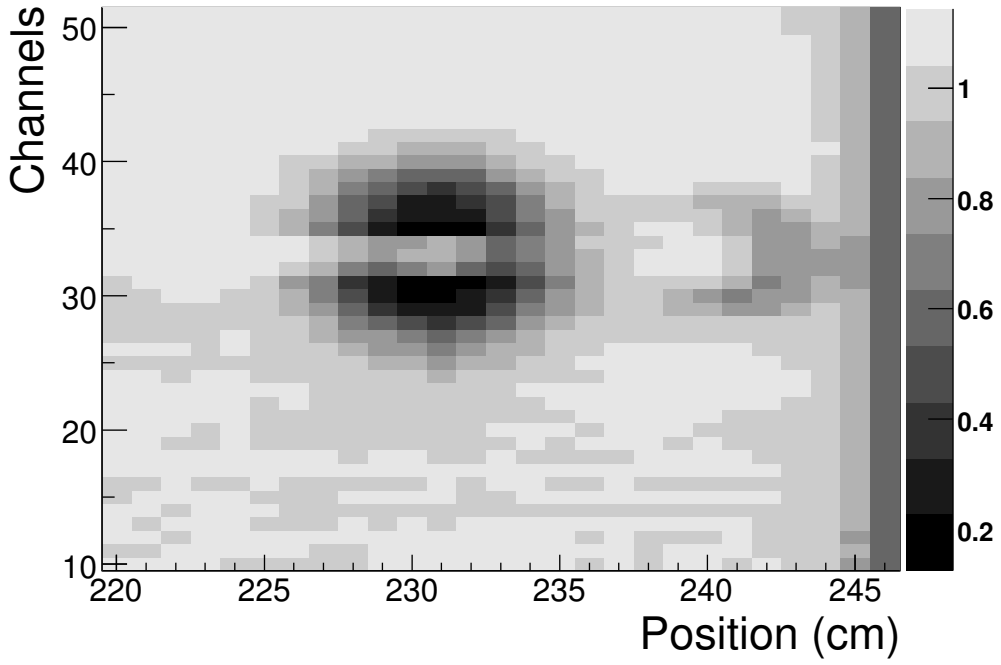

(a) Before HV training

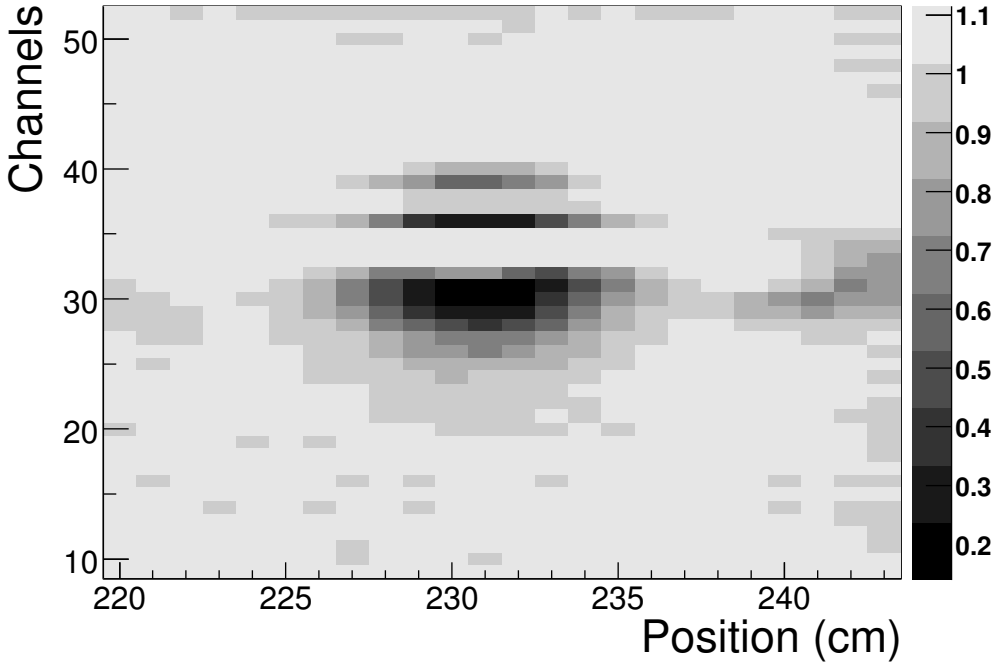

(b) After HV training

Figure 4.16: *A module was irradiated with a 2 mCi ^{90}Sr source located above wire 32 at position 231 cm. The aging pattern is shown in the upper panel. In the lower panel, the half of the damaged area (from wire 33 through wire 64) was trained at 1900 V. Most wires recovered from the damage.*

straws). In this framework, the higher damage, observed at higher gas flow, can be related to the faster transport of ozone. Small quantities (≈100 ppm) of a strong stable oxidant with a molecular structure similar to O_3, nitrogen dioxide (NO_2), was added to the gas mixture. Beneficial effects of NO_2 in preventing the aging were observed [60]. Unfortunately, NO_2 is a highly poisonous and aggressive chemical that would require very special treatment in the gas system.
Given that the glue is out-gassing, it was verified that heating an entire module to a temperature of 40°C can increase the beneficial effects of flushing. A setup to heat all modules of the OT detector in situ was designed and installed in the LHCb hall on 2008. Aging still occurs, but at a slower rate. Tests are still ongoing.

4.5.3 Prospective for Run1

Tests have shown that the gain reduction as function of the irradiation dose has large variations from module to module. Some of the modules are almost completely aging resistant, whereas others show a large gain reduction. Modules were flushed starting prior to installation and heated in situ. HV training can recover aging effect, but may not always be fully effective. The possibility to add to the counting gas chemical substances (e.g NO_2) moderating the gain loss is currently under study.
A gain loss in the analog signal, could be compensated by reducing the threshold of the analog readout at the price of a higher noise rate [52]. Alternatively, the gain loss can be compensated by a higher HV, at the cost of larger cross talk in the region without irradiation damage.

The maximum damage is obtained by low intensity irradiation which produce a current of few nA on the wire. From the expected particle flux, the dose and therefore the current on the wire can be estimated by simulation and result of about 7 nA in the hottest region. The results obtained in the laboratory with a small setup can be extrapolated at larger scale on the OT layers in the LHC enviroment for a nominal year of integrated luminosity, under several assumptions [61]. The resulting gain loss in the transverse plane of the OT layer is shown in Fig. 4.17. The highest damage is of about 50% in gain loss, located at low y on the magnet bending plane where the particle flux is higher.

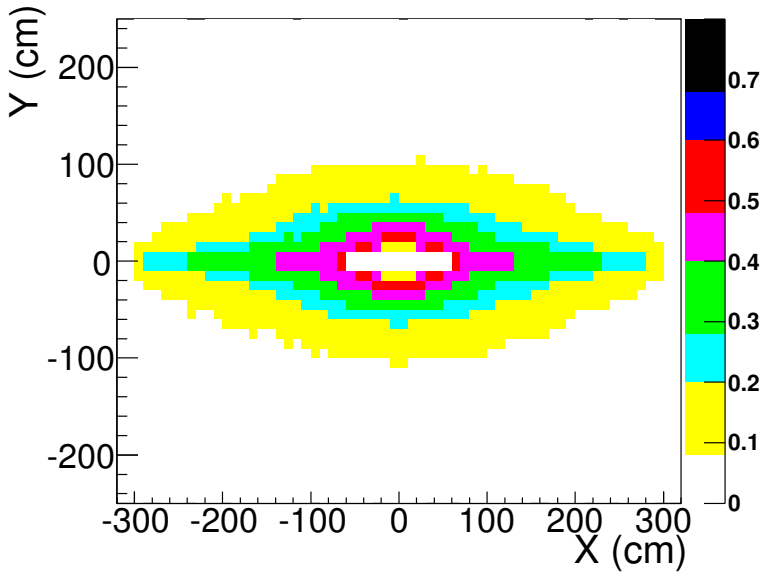

Figure 4.17: *Gain loss after 1 year LHCb nominal lumi.*

4.6 Outlook

The Tracking Stations (T-stations) measure the momenta of charged particles. They cover a surface-area of about 6 × 5 m^2. Over this area, there is a large variation in the particle flux: the innermost part (IT) is covered with silicon strips, while the outer part (OT) is covered with straw tube drift cells. The OT serves to reconstruct tracks with a nominal momentum resolution ($\Delta p/p$) of about 0.5% in the momentum region from 2 to 100 GeV. The OT layers in the T stations consist of modules. Each module has two separated detector halves containing two mono-layers of straw tubes. The detector efficiency and resolution have been measured in a test beam: a resolution of 200 μm and an average cell efficiency ϵ_{cell} of 98% have been found.

Irradiation of the straw modules with low intensity ($\sim$ 2 mCi) radioactive sources, have shown significant gain loss. Dedicated tests showed that this is due to the out-gassing of the glue used in the module construction (ARALDITE AY103-1 resin in combination with the HY901 hardener) sufficient to cause insulating deposits on the wire. To increase the lifetime of the module, the installed modules were flushed and heated in situ. HV training can recover the gain lost, but may not always be fully effective. The possibility to add to the counting gas chemical substances (e.g NO_2) moderating the gain loss is currently under study. A loss of pulse height in the analog signal could be compensated by reducing the preamplifier thresholds (at the price of a higher noise rate) or by raising the HV (at the cost of larger cross talk in the region without irradiation damage).

Chapter 5

Outer Tracker Electronics

5.1 Introduction

The working principle of the straw tubes has been illustrated in Sec 4.1. As discussed therein, the hit signals on the anode wires are induced by the movements of the electrons (fast drift toward the wires) and of the ions (slow drift toward the straw walls) liberated in the gas amplification process (proportional regime). The drift times of particles detected in the OT are measured by the OT electronics as the time difference between the hit signals from the anode wires and the LHC bunch crossing clock. Before the hit timing can be determined, the small hit signals have to be amplified. The connection between the drift-tubes and the preamplifiers is schematically shown in Fig. 5.1(a). The signal shape and magnitude have to be carefully considered in the Front-End (FE) Electronics design. E.g. dead-time-free operation in the fast LHC bunch structure (25 ns spacing) requires the cancellation of the slow ion tail in the signal shape (see Fig. 5.1(b)).

The OT FE Electronics schematically (see Fig. 5.2(a)) consists of a fast amplifier with a baseline restoration circuit to eliminate the slow ion tail, a discriminator to generate the hit signal, and a Time-to-Digital Convertor (TDC) to determine the timing of this hit signal. The OT FE electronics provides fast, virtually dead-time free response demanded by the revolution frequency (40 MHz) of the LHC machine. To accomodate a required drift distance measurement resolution of 200 μm a time resolution of 2 ns is required [47]. Moreover, the high-occupancy environment of the LHCb experiment requires minimization of the number of fake hits due to noise and cross-talk, specified to be less than 10 kHz per channel and 5%, respectively [52]. Last but not least, the multi-particle final states of interest for the reconstruction of the B decays, demand an intrinsic drift-cell efficiency of virtually 100%, implying that the preamplifier threshold should not exceed an equivalent charge of 4 fC (a Minimum Ionizing Particle (MIP) causes an average charge of 400 fC on the anode wires, of which about 67 fC is collected by the preamplifier).

The Front-End (FE) Electronics is hosted in modular units (FE-Boxes) installed at both ends of each detector module. A FE-Box services 128 straw-tube channels, each channel consisting of a shaping preamplifier and a discriminator, a TDC and a data serializer and optical link transmitter. Therefore, a FE-Box contains all the electronics necessary to read out the hit signals from the straw tubes, determine their timing with respect to the LHC clock, and ship them to the off-detector readout electronics if a positive L0 decision is received. These functionalities are implemented in a modular structure, consisting of various service boards: HV board (decoupling the analog signal on the anode wire from the high voltage), ASDBLR board (preamplifying and discriminating the analog signal), OTIS board (measuring the hit time with a TDC), and GOL/AUX board (supplying bias voltages and serializing data for optical transmission). These are shown in Fig. 5.2(a). The service boards are housed in an aluminum frame built to fit to the straw module and providing grounding and shielding.

5.1.1 FE-Box

A FE-Box consists of an aluminum chassis designed to fit to one end of the module. On this chassis are mounted 4 HV boards, 8 ASDBLR preamplifier boards, 4 OTIS TDC boards and 1 GOL/AUX Board, closed by metallic covers. The FE-Box provides the grounding and shielding of the straw-tube modules.

5.1.2 HV board

This board provides the interface between the FE Electronics and the anode wires. The essential function of the board is to host 32 capacitors of 330 pF to decouple the positive HV to the anode wires from the small hit charges to the ASDBLR preamplifiers. The capacitors are buried inside the PCB layer structure to reduce the environmental effects of the leakage current. Each FE-Box hosts 4 HV boards.

5.1.3 Amplifier

The hit signals from the anode wires are amplified, shaped and discriminated by means of the 8-channels ASDBLR chips developed for the ATLAS Transition Radiation Tracker [62]. The ASDBLR has a fast peaking time of about 7 ns and a fast baseline restoration to eliminate the long ion tail.

The ASDBLR chips have been produced with the DMILL process, that guarantees low crosstalk (0.2%), low noise ($\leq 1\ fC$) and a radiation hardness withstanding 3.5 $\times 10^{14}\ n/cm^2$ [63]. Two ASDBLR chips are assembled on one PCB (the ASDBLR Board). Each FE-Box hosts 8 ASDBLR boards. The ASDBLR test and selection procedure is discussed in detail in Sec. 5.3.

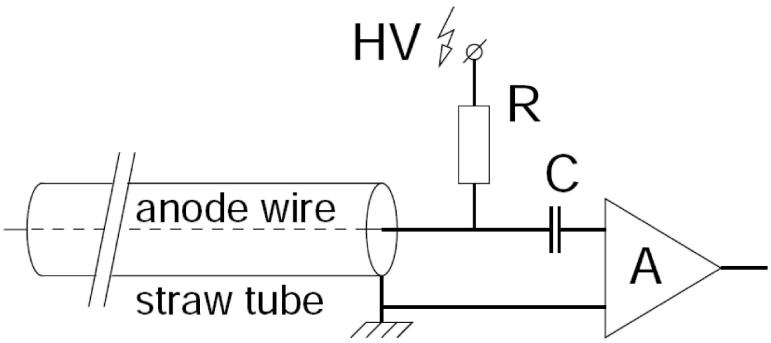

(a) Straw tube connection.

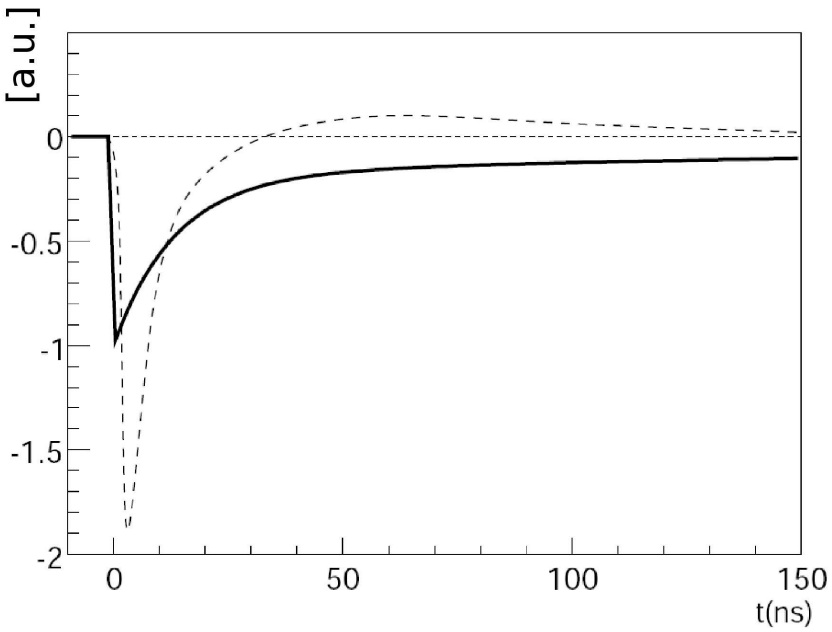

(b) Charge pulse.

Figure 5.1: *(a) Schematic of the straw tube connections. The High Voltage (HV) is connected through a series resistance R to the anode wire; the straw tube wall, acting as the cathode, is grounded. The preamplifier A is isolated from the HV by the capacitor C. (b) Modeled charge pulse for a single avalanche in Ar(70%)-CO_2(30%) counting gas after pre-amplifying (continuous line) and after shaping (dotted line), see text. An arbitrary threshold level is drawn [47].*

5.1.4 Time to digital converter (TDC)

The Outer tracker Time Information System (OTIS), is a 32-channels clock-driven TDC chip developed for the readout of the LHCb OT straw tubes produced with 0.25 μm CMOS technology. Digitized signals from two ASDBLR boards are sent to one OTIS Board that hosts one TDC chip. The OTIS TDC operates synchronous to the 40 MHz bunch crossing clock and provides intermediate data storage in the 4 μs L0 pipeline buffer. If a positive L0 trigger decision arrives, the chip transfers the corresponding event data to the GOL serializer chip. The OTIS chip is able to cope with a 1.1 MHz L0 rate and it is controlled via I^2C-bus by the Experimental Control System (ECS). In addition, the OTIS chip provides the threshold voltages to the four ASDBLR chips connected to it. The OTIS production and test is discussed in detail in Sec. 5.4. Each FE-Box hosts 4 OTIS boards.

5.1.5 Gigabyte optical link (GOL)

The output of four OTIS TDCs is sent to one Gigabit Optical Link chip [64] (GOL) mounted on the GOL/AUX Board. This board provides also the bias to the OTIS and the ASDBLR by means of radiation-hard voltage regulators and distributes the slow (ECS) and fast control (TFC) signals to the FE-Box. Optical fibers carry the data in the counting house at an output rate of 1.3 $Gbits/s$ to the TELL1 buffer board, which zero suppresses and ships the data to the HLT computer farm. Each FE-Box hosts 1 GOL/AUX board.

5.2 FE Electronics production and quality assurance

The OT FE Electronics required the production of about 500 FE-Boxes, including spares. This corresponds to several thousands boards of each type. This large number, in combination with the demanding requirements on the production quality, required a complex system of quality assurance and tracing to be developed. In the next section, the quality checks performed on the individual FE boards (ASDBLR, OTIS etc.) as well as on the final assembled FE-Box will be described. Each item in the process was assigned a unique serial number and a system of tracing based on a series of ACCESS databases was put in place.

5.3 ASDBLR chip production and quality assurance

The observed failure rate of the ASDBLR chip production has been of the order of 50% to 60%, attributed to a high defect density in the process (DMILL) and to electrical pick-up between circuit blocks. It was possible to increase the number of wafers purchased to accommodate for this lower yield: for the LHCb OT, 28514 chips were ordered whereas 8000 chips were needed. The final production

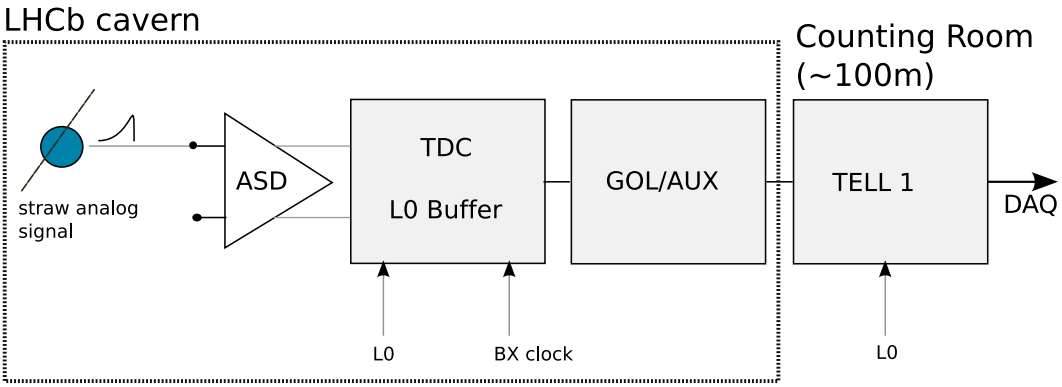

(a)

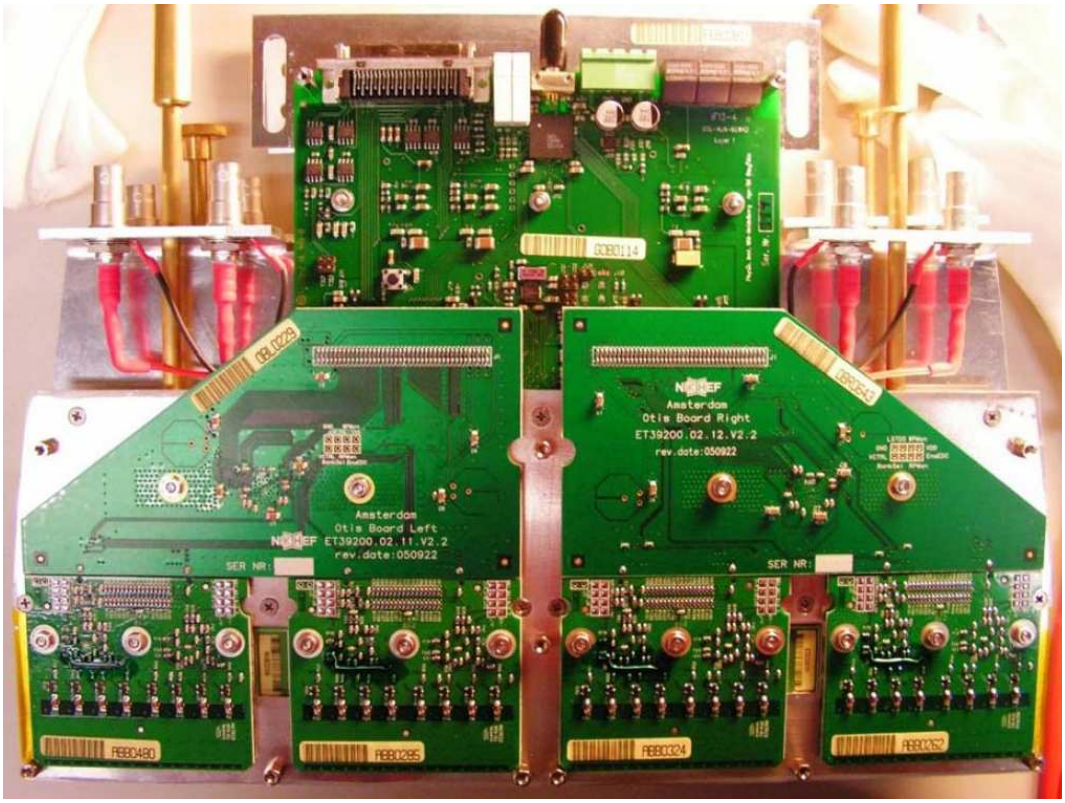

(b)

Figure 5.2: *(a) Schematic view of the OT FE Electronics for one channel. (b) A FE-Box reads out 128 channels and hosts 1 GOL/AUX Board, 4 OTIS TDC boards, 8 ASDBLR preamplifier boards and 4 HV boards. In the picture a FE-box is shown without cover and some of the boards are visible. From top to bottom: GOL /AUX Board, two OTIS board and 4 ASDBLR boards. The HV boards are not visible because they are beneath the ASDBLR boards on the other side of the aluminum chassis.*

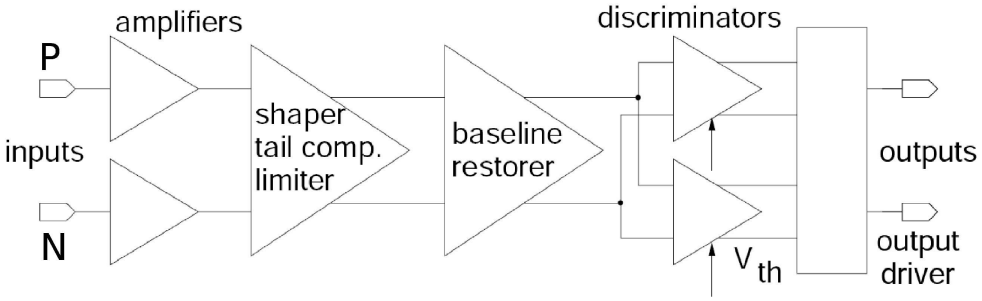

Figure 5.3: *Block diagram of the ASDBLR chip (one channel). Two amplifiers receive the analog input signal, followed by the shaper, tail compensator, limiter and baseline restorer. The baseline restorer is then fed into two discriminators (see text).*

took place in the second half of 2003, as a common project between the ATLAS TRT and the LHCb OT, leading to the production of 143 six-inch wafers, with 1042 elements each. Packaged ASDBLRs were delivered in trays with laser engraved, 2-D bar-coded serial numbers. All chips were tested at the University of Pennsylvania Chip Testing Facility using an 80 pin, 400 MHz, [1] IMS chip tester, fed by a custom adapted Exatron robotic chip handler.

In the ASDBLR, the signal processing is split in four separate parts as shown in Fig. 5.3. The preamplifier converts a charge at the input into a voltage output, minimizing the noise added to the signal. The shaper eliminates both the ion tail of the current signal and the preamp tail using the pole-zero cancellation circuit. The result is an output pulse exhibiting a simple exponential decay with a short time constant and without the undershoot of a simple CR differentiator. The shaped signal is then AC coupled into the two discriminator inputs: the chip allows to set two independent thresholds per channel, but this functionality has not been implemented in the OT FE, where only the low-threshold discriminator is used. For debugging a monitor is provided to examine the shaper output.

5.3.1 ASDBLR chip preselection cuts

Each chip was DC tested for input channel resistance, power supply currents, input diode voltage, input/output current, output switch current, and hit efficiency.

[1] Integrated Measurement Systems (IMS) mixed analog/digital integrated circuit tester.

Input resistance test

The input resistance is measured on the power supply connectors in order to check if there are shorts or open connections. The expected value of 38kΩ is verified on the Positive and Negative supply (R_P,R_N). For an accepted chip, the R_P and R_N have to range between 10 and 50kΩ: 498 out of 28514 chips fail the cut.

Power supply test

The power consumption of the chip has to be within the specification. The current values (positive and negative) are measured on the power supply connection. They have to be between 64 and 76 mA to be accepted. 2065 out of 28514 chips fail the requirement on the positive current and 1495 out of 28514 chips fail the requirement on negative current.

Baseline restoration monitor

The working point of the baseline restoration is expected to be 700 mV. Large deviations indicate malfunctioning. The monitor value was measured and chips within 380 mV and 1340 mV are accepted. 1099 out of 28514 chips fail the criterion.

Input diode test

Each channel is provided with a diode at the input. The voltages on both sides of the input diode were measured for each channel (two measurements per channel). The expected difference among the two measurements is of about 700 mV. A cut between 500 mV and 1050 mV was applied. 1408 out of 28514 chips fail this cut.

Input current test

The threshold input normally draws only a few μA current and should not load the OTIS DAC. A selection cut is imposed on the measured input current and voltage for both the high and low discriminators thresholds ($I_{thr}^{low/high}$ and $V_{thr}^{low/high}$):

$$I_{thr}^{min} + G_{thr} \;\; V_{thr}^{low/high} < I_{thr}^{low/high} < I_{thr}^{max} + G_{thr} \;\; V_{thr}^{low/high}, \tag{5.1}$$

where $I_{thr}^{min} = -1$ mA are $I_{thr}^{max} = 2.5$ mA (current offsets at V_{thr}=0) and $G_{thr} = 2$ mA/V quantify the current gain which increases with the threshold since the ASDBLR is a current driven amplifier. 1424 out of 28514 chips fail this test.

Output current test

The discriminators output current was measured for all channels on both N and P junctions $O_{N/P}^{low/high}$. The sum $O_N^{low/high} + O_P^{low/high}$ is expected to be about 1.6 mA for both discriminators. Chips with a single channel out of the range between 1.2 mA and 2.1 mA were rejected: 1271 out of 28514 chips fail this test.

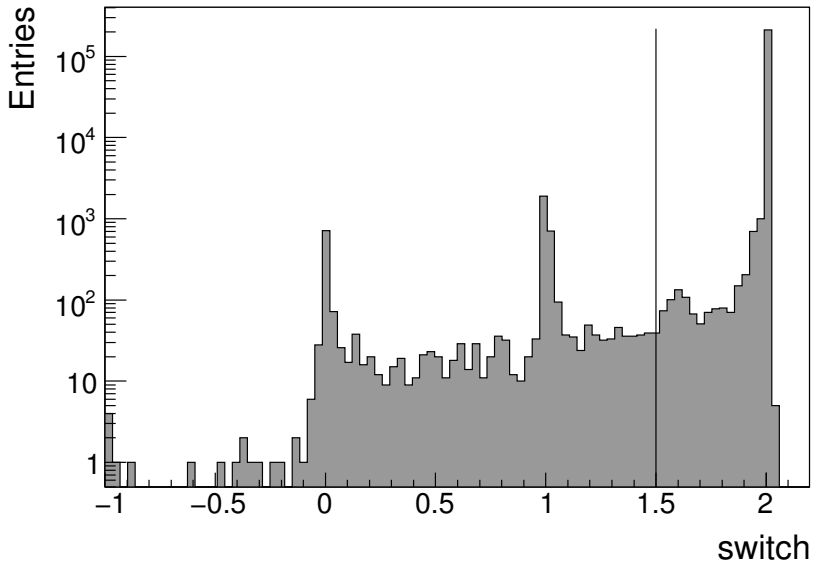

Figure 5.4: *Distribution of the variable "Switch" defined in Eq. 5.2. Entries above the vertical line corresponds to accepted chips. The peak at zero corresponds to channels in which all the measured currents were zero. The peak at one corresponds to channel in which the current measured on one of the P or N junctions was zero.*

Output switch test

This test is aimed at verifying if an output is "toggling". This is done through a pair of switches (one for the high and one for the low threshold level). From the measured discriminator output current, a cut on the following variable is applied:

$$Switch \equiv \frac{O_N^{low} - O_P^{low}}{O_N^{low} + O_P^{low}} - \frac{O_N^{high} - O_P^{high}}{O_N^{high} + O_P^{high}}. \tag{5.2}$$

The distribution of the variable "$Switch$" over all channels of the chips is shown in Fig. 5.4. A chip passes this acceptance test if all of its eight channels have Switch>1.5. 4015 out of 28514 chips fail this test.

Damaged channels

This last pre-selection cut provides a selection of working channels based on the hit efficiency values measured by injecting known input charges (5 fC and 30 fC). Broken channels with abnormally low hit efficiency were spotted and 7604 out of 28514 chips rejected.

Summary of preselection

The results of the pre-selection cuts are summarized in Tab. 5.1. A total of 8576 chip does not pass the preselection. The remaining 19938 chips are further selected according to their threshold characteristics.

cut	rejected/total	rejected/remaining
Input Resistance	498	498
Power Supply (+)	2065	1903
Power Supply (-)	1495	95
Baseline Restored Monitor	1099	46
Input Diode Voltage	1408	117
Input Current	1424	248
Output Current	1271	125
Output Switching	4015	2487
Damaged Channels	7604	3057
all cuts	/	8576

Table 5.1: *Chip rejections in the pre-selection. In the 2^{nd} column the number of chips rejected by the single cut over the total of 28514 chip is shown. In the 3^{rd} column the number of chips rejected by the single cut over the total of the remaining chips after the previous cuts (in sequence) is shown.*

5.3.2 Threshold characteristic

Stringent requirements are set on the channel-by-channel uniformity response for the same input charge Q. The threshold must be chosen such that the uniformity between channels is guaranteed in a wide range of input charges. A good uniformity of the amplifiers allows to use a common threshold for all the readout without significant loss of efficiency.
The function $g(Q)$, representing the voltage which needs to be applied to the ASBLR threshold input in order to obtain the threshold charge value of Q, must to be known for a given channel. In a digital system, this is done through measuring the hit efficiency as a function of threshold [65–67]. Varying the threshold from low to high, the hit-efficiency goes from 1 to 0. In the ideal conditions of absence of noise, the hit-efficiency versus threshold would be a step function. Assuming Gaussian noise, the expression for the hit-probability for a given threshold V_{thr} and the input charge

Q is

$$Pr(V_{thr}, Q) = N \int_{V_{thr}}^{+\infty} e^{-\frac{1}{2}\left(\frac{V-g(Q)}{\sigma_{noise}}\right)^2} dV, \tag{5.3}$$

where N is a normalization factor and σ_{noise} is the Gaussian noise amplitude. Eq. 5.3 can be rewritten in terms of the so called "*error function*":

$$Pr(V_{thr}, Q) = \frac{1}{2} \; - \; \frac{1}{2} Erf\Big(\frac{V_{thr} - g(Q)}{\sqrt{2}\ \sigma_{noise}}\Big). \tag{5.4}$$

The resulting noise model is shown in Fig. 5.5. The hit-efficiency is 50% for $V_{thr} = g(Q)$. The threshold at which this condition is realized is called "half efficiency threshold" $V_{thr}^{50\%}$. By measuring the hit-efficiency versus threshold and fitting Eq. 5.4 to the data, the channel-by-channel $V_{thr}^{50\%}$ and σ_{noise} can be determined.
Analogously, if the discriminator threshold is kept fixed while varying the input charge Q, the probability becomes:

$$Pr(Q, V_{thr}) = \frac{1}{2} \; + \; \frac{1}{2} Erf\Big(\frac{g(Q) - V_{thr}}{\sqrt{2}\ \sigma_{noise}}\Big). \tag{5.5}$$

Selection on threshold characteristic

After the pre-selection, chips are classified on the basis of the uniformity of their response. All channels were tested by injecting known input charges (0 fC, 3 fC, 5 fC, 30 fC and 50 fC) and determining the threshold values $V_{thr}^{[50\%]}(\text{chip}, \text{ch})$ for all the channels on each chip [65,66]. The 30 fC and 50 fC input charge are specific for testing the high-threshold discriminator. The test is valid for the chip characterization, although its functionality is not implemented in the OT readout. All results were stored in the chip test database.

The threshold uniformity of the ASDBLR channels can be evaluated per chip (differences among the eight channels of each chip) or globally (differences among all channels of all chips), for each values of the injected charge. If one defines the chip average response as

$$\tilde{V}_{thr}^{[50\%]}(\text{chip}) \equiv \frac{1}{8} \sum_{ch=1}^{8} V_{thr}^{[50\%]}(\text{chip}, \text{ch}), \tag{5.6}$$

and the per-chip channel deviation as

$$\begin{aligned} \Delta V_{thr}(\text{chip}, \text{ch}) &\equiv \tilde{V}_{thr}^{[50\%]}(\text{chip}) - V_{thr}^{[50\%]}(\text{chip}, \text{ch}) \\ &= \frac{1}{8} \sum_{ch=1}^{8} V_{thr}^{[50\%]}(\text{chip}, \text{ch}) - V_{thr}^{[50\%]}(\text{chip}, \text{ch}), \end{aligned} \tag{5.7}$$

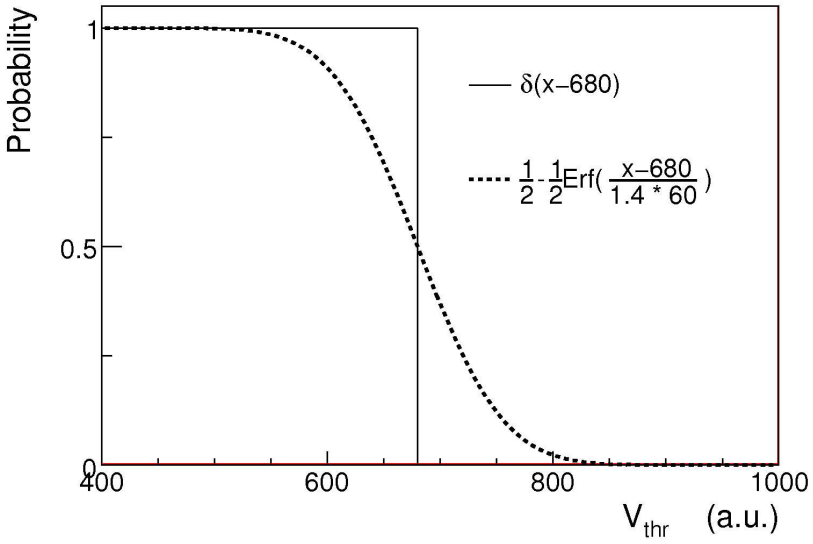

(a)

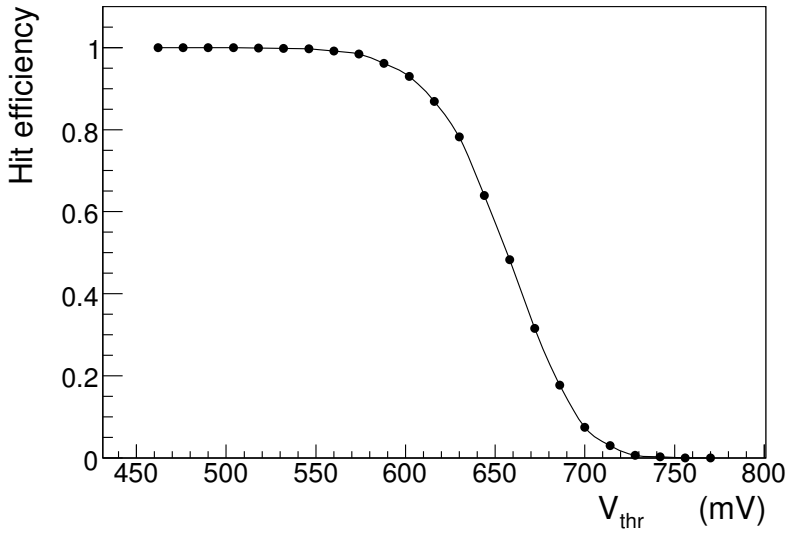

(b)

Figure 5.5: *Model for hit efficiency versus threshold. (a) In absence of noise the efficiency curve is a step function (continuous curve). In presence of gaussian noise the resulting efficiency is denoted by the dashed curve. (b) Example of hit-efficiency as function of threshold for a fixed input charge of 3 fC.*

then chips can be sorted according to the value of ΔV_{thr}^{max}, defined for each chip as the largest of the deviations in Eq. 5.7 taken with its sign. Analogously, if one substitutes the single-chip average in Eq. 5.7 with the global average:

$$\begin{aligned} \tilde{V}_{thr}^{[50\%]} &\equiv \frac{1}{(8\,\mathrm{N}_{chip})} \sum_{chip} \sum_{ch=1}^{8} V_{thr}^{[50\%]}\,(\mathrm{chip},\mathrm{ch}) \\ &= \frac{1}{\mathrm{N}_{chip}} \sum_{chip=1}^{N_{chip}} \tilde{V}_{thr}^{[50\%]}\,(\mathrm{chip})\,, \end{aligned} \tag{5.8}$$

then a more stringent selection based on the global threshold uniformity can be made, by placing cuts on the global deviation:

$$\begin{aligned} \Delta V_{thr}^{G}(\mathrm{chip},\mathrm{ch}) &\equiv \tilde{V}_{thr}^{[50\%]} - V_{thr}^{[50\%]}\,(\mathrm{chip},\mathrm{ch}) \\ &= \frac{1}{(8\,\mathrm{N}_{chip})} \sum_{chip} \sum_{ch=1}^{8} V_{thr}^{[50\%]}\,(\mathrm{chip},\mathrm{ch}) - V_{thr}^{[50\%]}\,(\mathrm{chip},\mathrm{ch})\,. \end{aligned} \tag{5.9}$$

An element of complication is introduced by the fact that the measured half-efficiency points have to be corrected for systematic differences (offsets), because each of the eight channels of the chip were tested simultaneously using eight independent injectors. Furthermore, due to retuning of the charge injector, these offsets may change considerably and therefore have to be re-evaluated for each test "*lot*" of 208 chips. The offset determination is based on a Gaussian fit to the 8 distributions of $V_{thr}^{[50\%]}\,(\mathrm{chip},\mathrm{ch})$ measured in the test of a chip lot. The values of the means $\{\mu\,(\mathrm{ch}) : \mathrm{ch} = 1, ..., 8\}$ from the Gaussian fits are then used to calculated the offsets:

$$\epsilon(\mathrm{ch}) \equiv \frac{1}{8} \sum_{k=1}^{8} \mu(k) - \mu(\mathrm{ch}), \tag{5.10}$$

which are in turn used to correct the values of $V_{thr}^{[50\%]}$ measured in the test of that chip lot:

$$V_{thr}^{[50\%]}\,(\mathrm{chip},\mathrm{ch}) \rightarrow V_{thr}^{[50\%]}\,(\mathrm{chip},\mathrm{ch}) + \epsilon(\mathrm{ch}). \tag{5.11}$$

The distributions of the maximum response deviation within a chip is shown in Fig. 5.6 (after the offset correction) and the distributions of the global response deviation is shown in Fig. 5.7 (after the offset correction). Further chip selection is based on cuts placed on these distributions.

ASDBLR classification

All threshold uniformity selections were based on the values of the ΔV_{thr}^{max} and ΔV_{thr}^{Gmax} (from the 5 fC tests for the low threshold and the 30 fC tests for the high threshold). Moreover, the maximum accepted deviation is about 0.4 fC [66], corresponding to about 30 mV. Only chips that passed the pre-selection were used, subdivided in the following four classes:

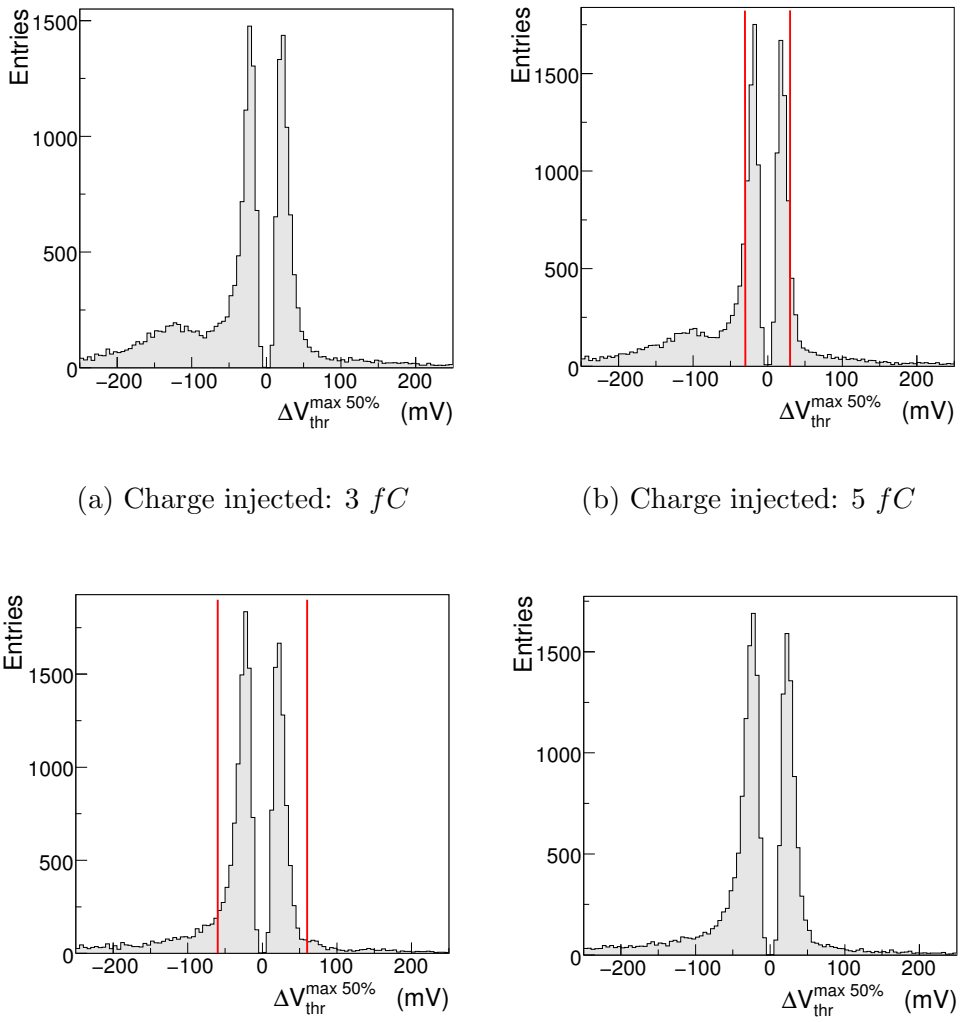

(a) Charge injected: 3 fC

(b) Charge injected: 5 fC

(c) Charge injected: 30 fC

(d) Charge injected: 50 fC

Figure 5.6: *Distributions of the maximum per-chip deviations ΔV_{thr}^{max}. Offset corrections were applied to the data. Each entry corresponds to one pre-selected chip. The vertical lines indicate the class A selection cuts (see text).*

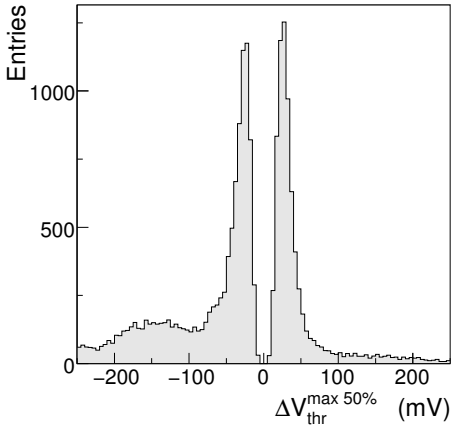

(a) Charge injected: 3 fC

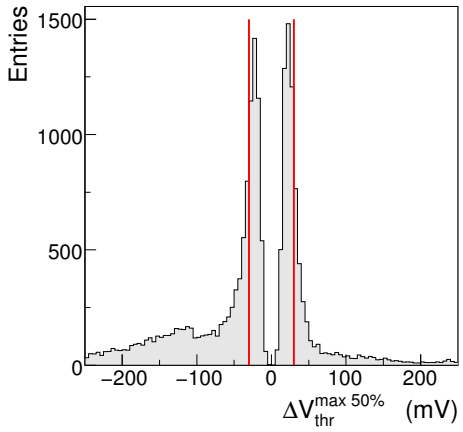

(b) Charge injected: 5 fC

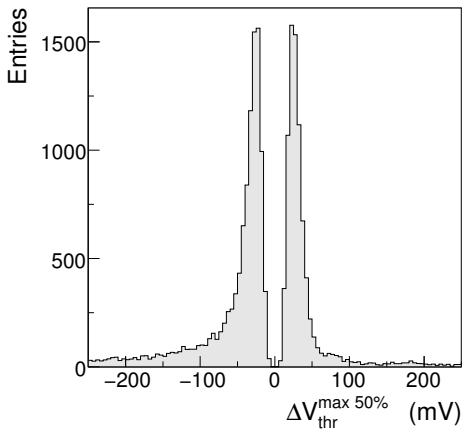

(c) Charge injected: 30 fC

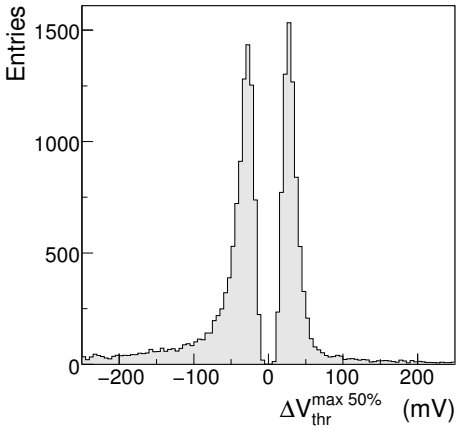

(d) Charge injected: 50 fC

Figure 5.7: *Distributions of the maximum global deviations ΔV_{thr}^{Gmax}. Offset corrections were applied to the data. Each entry corresponds to one pre-selected chip. The vertical lines indicate the class A selection cut (see text).*

- "*Class A*", (8158 chips out of 19938)
  Cut on Low Threshold: $|\Delta\ V_{thr}^{max}[5\ fC]| \leq 30\ mV$.
  Cut on High Threshold: $|\Delta\ V_{thr}^{max}[30\ fC]| \leq 60\ mV$.
  Cut on Low Threshold: $|\Delta\ V_{thr}^{Gmax}[5\ fC]| \leq 30\ mV$.

- "*Class B′*", (1248 out of 19938 chips, excluding "*Class A*")
  Cut on Low Threshold: $|\Delta\ V_{thr}^{max}[5\ fC]| \leq 30\ mV$.
  Cut on High Threshold: $|\Delta\ V_{thr}^{max}[30\ fC]| \leq 60\ mV$.
  Cut on Low Threshold: $|\Delta\ V_{thr}^{Gmax}[5\ fC]| \leq 36.5\ mV$.

- "*Class B*", (2133 out of 19938 chips, excluding "*Class A and B′*").
  Cut on Low Threshold: $|\Delta\ V_{thr}^{max}[5\ fC]| \leq 45\ mV$.
  Cut on High Threshold: $|\Delta\ V_{thr}^{max}[30\ fC]| \leq 100\ mV$.
  Cut on Low Threshold: $|\Delta\ V_{thr}^{Gmax}[5\ fC]| \leq 45\ mV$.

- "*Class C*", (698 chips out of 19938, excluding "*ClassA, B′ and B″*").
  Cut on Low Threshold: $|\Delta\ V_{thr}^{max}[5\ fC]| \leq 60\ mV$.
  Cut on High Threshold: -140 mV $\leq \Delta\ V_{thr}^{max}[30\ fC] \leq 100\ mV$.
  Cut on Low Threshold: $|\Delta\ V_{thr}^{Gmax}[5\ fC]| \leq 60\ mV$.

- "*Class D*", (7701 chips out of 19938, excluding "*Class A, B′, B″ and C*").
  Remaining chips (that passed the pre-selection).

- "*Class E*", (8576 chips).
  All Others.

In the ASDBLR Board produced for the OT FE Electronics, only chips of class A and B' were used.

5.4 OTIS production and test

The OTIS digitizes the time difference between a hit and the LHC bunch crossing clock. The architecture of the OTIS TDC core is shown in Fig. 5.8. At the inputs, level comparators receive the hit signals from the ASDBLR chips. A programmable channel mask register blocks channels from entering the data stream (hot or noisy channels). The actual time measurement is performed by means of a Delay Locked Loop (DLL), providing fine time steps of 150 ps within a 25 ns clock cycle. The state of the DLL is copied to the corresponding Hit Register (HR), translated to a 6 bit time word by the Decoders (D), and written to the pipeline buffer. The pipeline is 160 cells deep and covers the L0 trigger latency of 4 μs. The bunch counter (BX)

value is written into the buffer as well, to check the buffer synchronization. Upon an L0 trigger, the corresponding hits and the BX value are copied to the derandomiser buffer. This buffer, accommodating for instantaneous variations of the L0 rate, is 48 cells deep to store up to 16 consecutive L0's while allowing a maximum of 3 BX to be searched (see Sec. 4.1) upon a single trigger signal. The sparsified event data is stored in a readout buffer before being transferred off the chip through the 8-bits wide readout interface in 36 clock cycles. An additional feature of the OTIS are 4 independent DACs, to provide threshold levels to the ASDBLR chips. The OTIS settings and DAC levels are programmable through an I^2C interface. The chip is implemented in 0.25 μm CMOS technology using radiation hard design techniques. A dedicated test

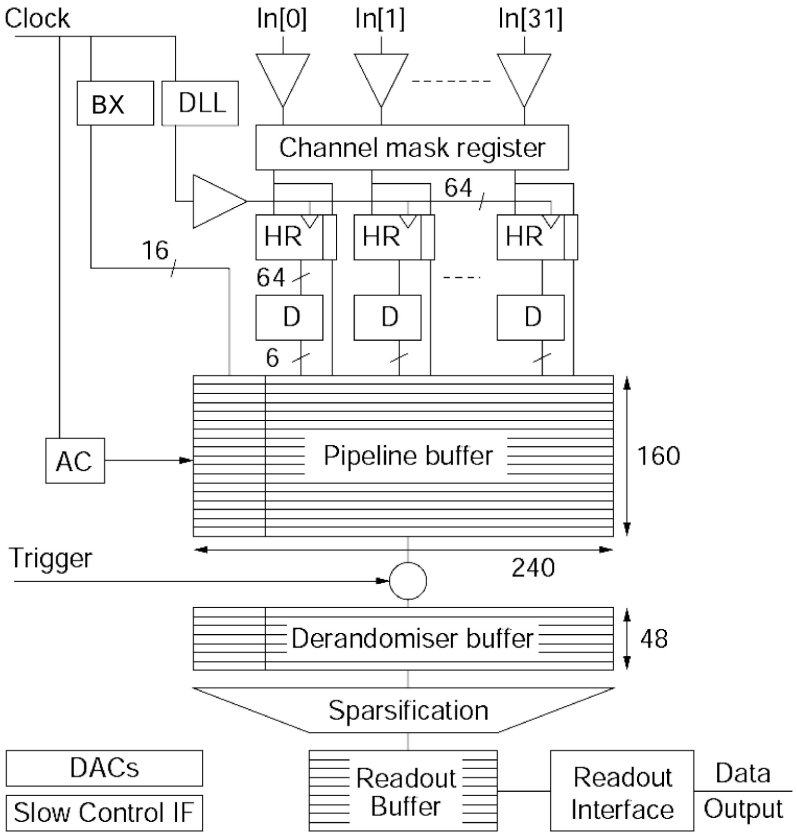

Figure 5.8: *Architecture of the OTIS TDC core. At the input, the level comparators receive the hit signal from the ASDBLR chips. Next is a programmable channel mask register to block noisy channels. Upon a hit signal the DLL state is copied to the Hit Register (HR), then translated into a 6 bit time word by the decoders, and finally written to the pipeline buffer. This is 160 stages deep corresponding to the 4 μs L0 latency. Upon an L0 trigger, the data is copied to the derandomiser buffer, which accommodates for instantaneous rate variations, accepting up to 16 consecutive L0's.*

setup was built to validate all OTIS chips produced. The TFC signals (clock, resets

and trigger) and the discriminated detector signals were produced by a pattern and a waveform generator. This system allowed to selectively store triggered data output sequences, to examine transferred header and data bytes and to build histograms of single-channel drift time data.
Input signals with random timing were sent to the OTIS and the corresponding "drift-times" measured. Deviations from the expected flat hit distribution reflect the width of the TDC time bins. The Δ_i-value for a given time bin i is defined as,

$$\Delta_i = \frac{N(i) - N(i-1)}{< N >}, \tag{5.12}$$

where $N(i)$ is the number of entries in the time bin i and <N> is the average number of entries per bin. The Differential Non Linearity (DNL) is defined as the sum of the absolute values of the minimum and the maximum deviations:

$$DNL \equiv |max\Delta_i| + |min\Delta_j| \tag{5.13}$$

The OTIS DNL was found to be of the order of 0.5 bin size (1 bin $\approx$ 390 ps).

5.5 HV board production and test

Each HV PCB was visually inspected to detect production faults (misaligned connectors, defects in the gold-plating, etc.). Due to the tight mechanical requirements of the FE-Boxes, a deviation in thickness from the nominal design value larger than 300 μm would result in a misalignment of the connector pins fitting to the straw tube modules. The thickness of each board was measured in three points: few boards having an average thickness below 2.74 mm or above 3.04 mm were rejected.

Long term tests under HV were done for all HV boards: 64 HV boards at a time were supplied with 2500 Volt (nominal 1600 Volt) at 70° for 48 hours. A dedicated test system was developed to monitor the leakage current (typically few nA for 32 channels) and the capacitance (nominal 330 pF) as shown in Fig. 5.9. The setup needs about one hour to reach a stable temperature and humidity, and the monitoring of the leakage current and capacitance shows a corresponding variation. Then, the leakage current decreases until it reaches a stable value. Capacitors breakdowns can be detected as reductions of the capacitance by 1/3, 2/3 or 100%, due the capacitors internal structure. After this test, about 10% of the HV boards were rejected, mainly due to high or unstable leakage currents.

5.6 ASBDLR board production and testing

The ASDBLR board hosts two ASDBLR chips. After a visual inspection of the PCB, chips were Ball-Grid-Array (BGA) mounted. The ASDBLR chip serial number was optically scanned and the information stored in the production DB for each ASDBLR board.

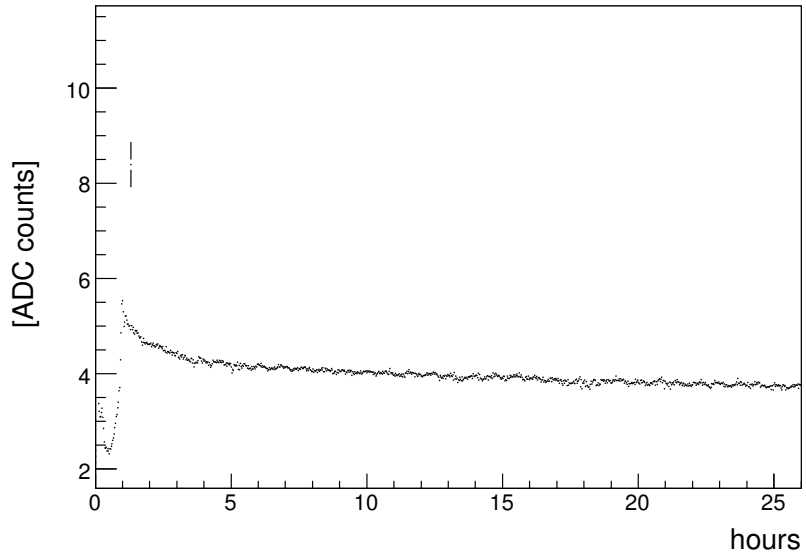

(a) Leakage current profile

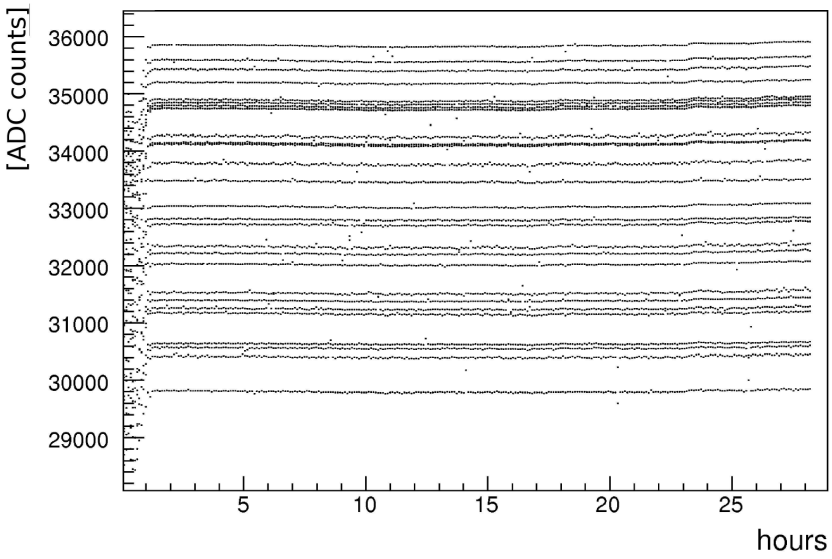

(b) Capacitance profile

Figure 5.9: *Typical results from the HV board test. (a) The leakage current of an HV board versus time (10 ADC counts ≈ 1 nA). (b) Monitor of 32 capacitances of an HV board versus time (100 ADC counts ≈ 1 pF). The variations of the leakage current and the capacitance during the first hour of test are due to temperature and humidity variations in the test setup.*

5.7 OTIS board production and testing

The OTIS board hosts one OTIS chip bonded on the PCB. In addition, it converts digital test-pulse lines into analog pulses of two different heights (high/low) that are then injected into the ASDBLR test inputs.
Prior to bonding, the bare PCBs underwent visual inspections to verify the absence of defects in the ground plane and the bonding pads. The inspections resulted in a significant rejection rate of about 15%.
The OTIS bonding was carried out in a semi-automatic way, at a rate of about 40 boards per day including the visual inspection of the bonded chip and the testing of the board functionality. The OTIS board functionality was tested using a dedicated setup providing bias voltages, slow control and data acquisition. The OTIS board under test was connected to two ASDBLR boards and the following checks were performed:

- The I^2C was checked writing an 8 bit sequence into the OTIS registers and reading them back.
- The ADC generating the ASDBLR thresholds were checked by scanning from 10 to 170 ADC counts in steps of 10 (9 mV). For each step, the difference between the set and the read-back voltage had to be within ± 15 mV.
- Random triggers were sent and the bunch crossing ID and Event ID distributions verified. The chip reset sequences were also checked.
- 10^4 test-pulses were generated and it was checked that none was missed.
- 10^6 random test-pulses were generated and the DNL calculated for channels: 0, 15, 16 and 31. The test failed if the DNL was equal to zero or higher than 9.

5.8 FE-Box global tests

Once the quality of the individual boards was checked and all data stored for tracing, FE-Boxes were assembled and commissioned using a special FE-Tester. The FE-Tester is a programmable pulser with a time resolution of 150 ps capable of testing all the functionalities of the readout, mimicking the real detector [68]. The block diagram of the setup is shown in Fig. 5.10. The heart of the setup is a PCB with an ALTERA programmable logic chip. To interface the FE-Box a specific connection board was developed ("*Flipper box*") with the additional required electronics to individually control the input signals to the 128 channels of the FE-Box. The setup is controlled by a LabView program on a PC connected via a [1]JTAG interface to the ALTERA board. For the communication with the FE-Box the I^2C bus is used.

[1]Joint Test Action Group.

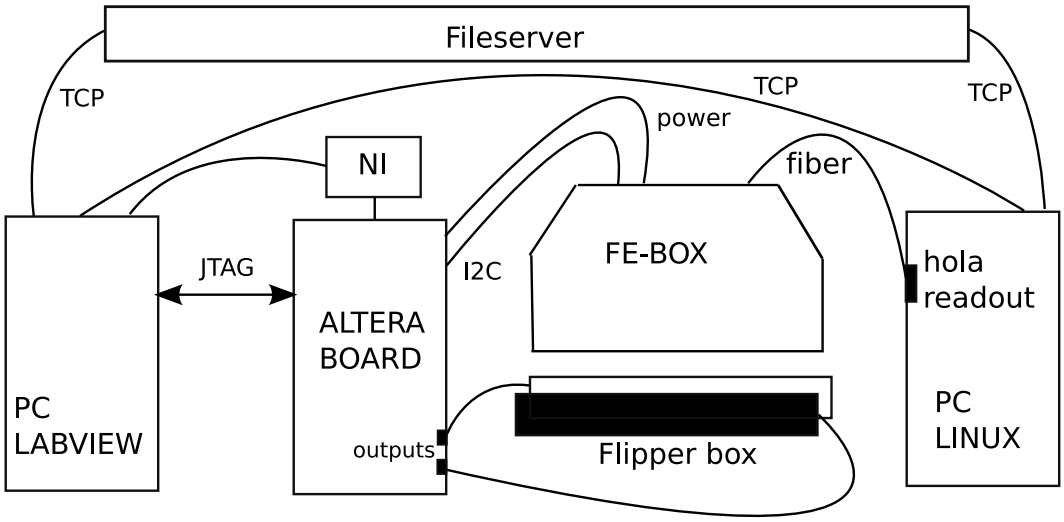

Figure 5.10: *Block diagram of the FE Test Setup. See the text for an explanation of the functionality of the parts.*

The FE-Box output data is collected by the HOLA acquisition board [69]. The FE-Tester functionalities are summarized here:

- Generation of input signals tunable in intensity and in time with a resolution of $\sim$0.5 fC and 150 ps, respectively.
- Generation of the Time and Fast Control (TFC) signals.
- Generation of the Slow Control through I^2C bus.
- Low voltage power supply.
- Data readout by using a HOLA acquisition board.

The following tests were performed:

- Threshold Characteristics. A threshold scan is done for fixed input charge, followed by an input scan at fixed threshold. The half-efficiency points are measured for all channels: relative variations are expected to be less than 60 mV (see Sec. 5.3.2). Threshold scans are also performed firing the test-pulse inputs (low and high) of the ASDBLR chip.
- Timing. The time conversion is probed by means of a delay scan.
- Noise. Noise is studied as a function of threshold.
- Synchronization. Synchronization of all channels is probed through a scan of the phase of the (L0) readout signal.

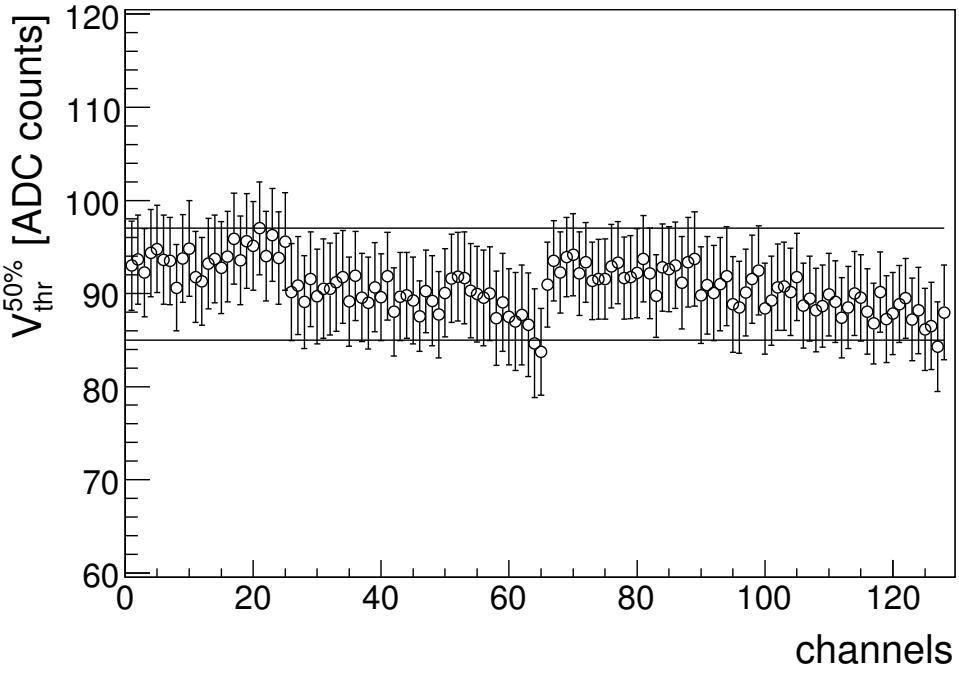

Figure 5.11: *$V_{thr}^{50\%}$ versus channel for one FE-box. The area within the lines indicates the acceptance window (1 ADC count $\approx$ 10 mV).*

5.8.1 $V_{thr}^{50\%}$ uniformity

The ASDBLR chips used in assembly were of the class A and B' as described in Sec. 5.3.2. After assembly, the $V_{thr}^{50\%}$ of each channel was measured by using the functionalities of the FE-Setup performing a threshold scan and injecting signals through the HV board, thus mimicking a detector module and therefore testing the whole FE electronics chain. The hit efficiency profile is measured for each channel and $V_{thr}^{50\%}$ is determined by fitting Eq. 5.4 to the data as described in Sec. 5.3.2. An example of summary plot showing $V_{thr}^{50\%}$ of the 128 channels of a FE-Box is shown in Fig. 5.11. The lines indicate the range of $\pm$ 6 ADC counts (1 ADC counts $\approx$ 10 mV) of the accepted deviation. About 2% of the ASDBLR chips showed a channel broken or had a large deviations. This was mainly due to problems in the chip soldering, missing components or damaged ASDBLR board input/output connector pins. Systematic uncertainties due to the setup (in particular the flipper box which fan out the input signal) are corrected for by adding an offset to each channel (typically $\leq$ 4%), deduced (see Eq. 5.10) from the mean values $\{\mu\,(\mathrm{ch}) : \mathrm{ch} = 1, ..., 128\}$:

$$\epsilon(\mathrm{ch}) \equiv \frac{1}{128}\sum_{k=1}^{128}\mu(k) - \mu(\mathrm{ch}). \tag{5.14}$$

5.8.2 Timing

The aim of the timing test is to measure the channel-by-channel time response. The FE-Setup provides an input signal with precise timing (0.15 ns). Tuning the delay between the clock and the input signal (for fixed threshold and input charge) a delay scan is performed over a range of 192 TDC channels corresponding to a window of 3 BX (75 ns). For each step, the distribution of the TDC time is obtained (see Fig. 5.12(a)) and the mean and RMS measured. The mean versus the delay set is shown in Fig. 5.12(b). A linear fit to the data is performed. All OTIS boards from the selection (see Sec. 5.4) showed a uniform time response.

5.8.3 Noise

A noise check is performed by means of a threshold scan in the absence of input charge. Channels are considered noisy if they exceed 0.1% occupancy (≈13 kHz) at a threshold of 760 mV. The OT operational threshold is 800 mV, roughly corresponding to 3.5 fC. Noisy channels or problems due to bad shielding were detected and repaired.

5.8.4 Synchronization

Time information per event is stored in the 4 μs pipeline buffer of the OTIS chip waiting for the L0 trigger decision (see Sec.5.4). It is crucial that all channels of a FE-Box are readout synchronously. Varying the L0 phase in steps of 0.75 ns a scan is performed to verify the overall synchronization through the read-out windows of 75 ns. A few OTIS boards showing a faulty behavior were replaced.

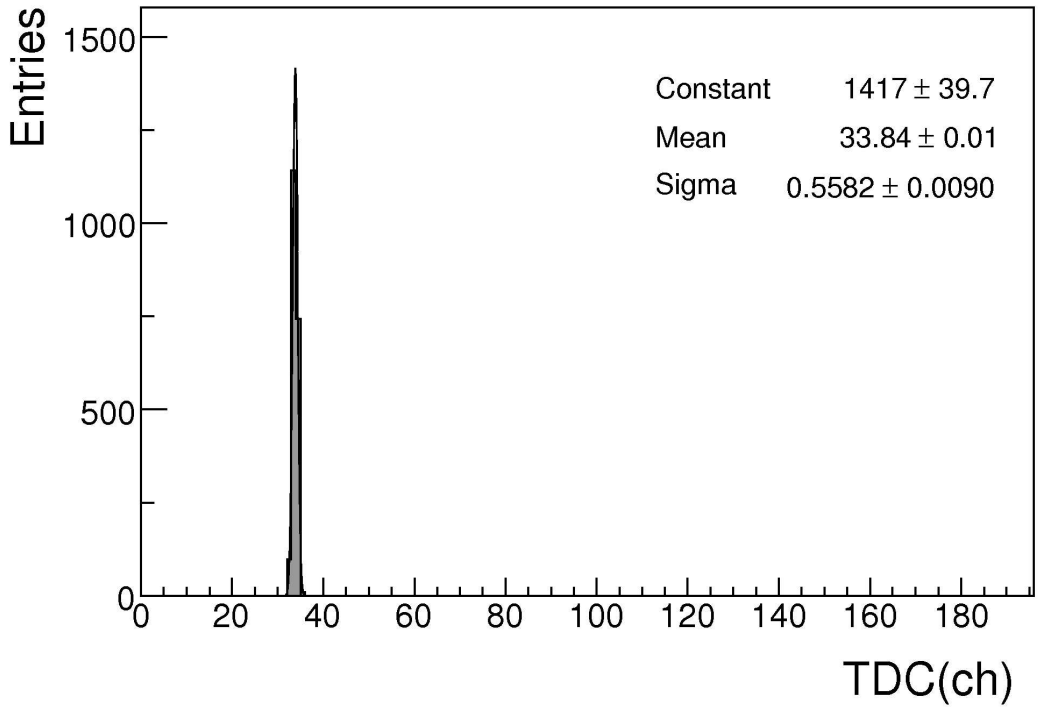

(a) TDC time distribution (delay of 33.86 TDC)

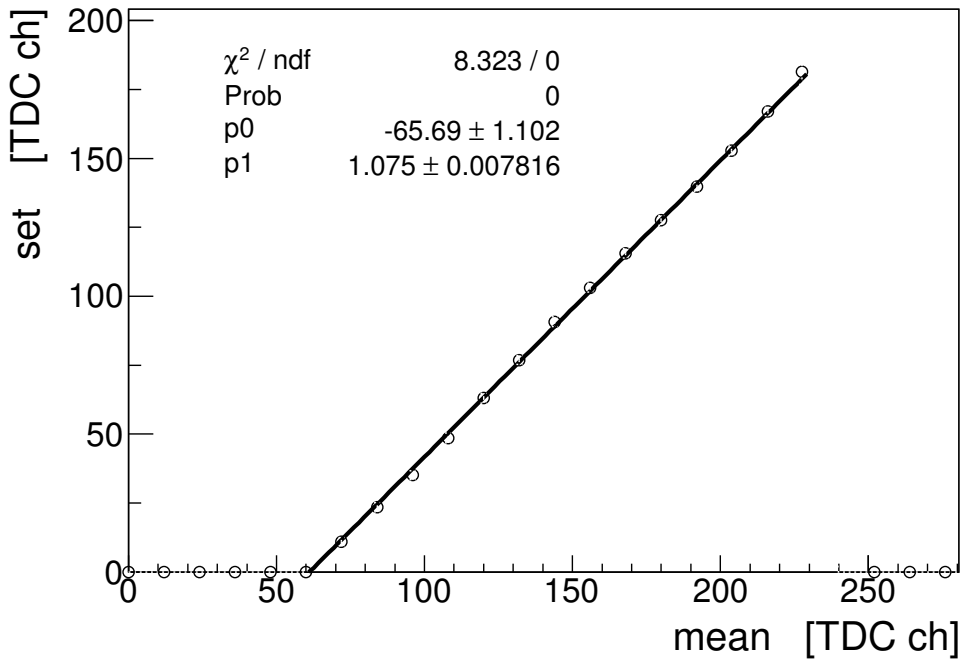

(b) Time linearity

Figure 5.12: *Timing tests. (a) Example of test-pulse time distribution at a given delay. (b) Linear fit to a delay scan.*

5.9 Outlook

The OT Electronics was installed and successfully commissioned. The strict ASDBLR and OTIS selection criteria (at the chip, board and global level) guarantee a high uniformity in the preamplifier and TDC responses. In particular, all ASDBLR chips can be operated with a unique threshold values without significant noise increase or efficiency loss, while the TDC resolution (± 0.5 bin) is well above the required drift time resolution ($\approx 2\ ns$).

Chapter 6

Effect of misalignment and B-field miscalibration on the momentum resolution

While the detector and the electronics discussed in the previous chapters have been installed and are being commissioned for data taking, preparations for data analysis based on MC studies are ongoing. In particular, detailed studies of the systematic uncertainties of the detector geometry description are of paramount importance in the calibration. A misaligned detector leads to a deterioration of the performance of the track reconstruction. This deterioration can be quantified in terms of an efficiency loss and reduced track parameter resolutions. In this chapter, the degradation of the momentum resolution due to the OT and IT misalignment is investigated. The study concentrates on common movements of detector elements that are hard to identify with tracks alone.

Another source of biases in the reconstructed momentum is errors in the magnetic field parametrization. The effect of a B-field scale transformation and its relation with a common position translation in the z-direction of the tracking stations are also studied.

A parametrization of these systematic effects is performed on long charged tracks in order to predict the effect on physics performance. Two decay channels are studied, namely: $J/\psi \to \mu\mu$ and $B_d \to \pi\pi$. Both these decays are important as control channels for the $B_s \to \mu^+\mu^-$ analysis.

6.1 Geometry and survey measurements

A detailed study of the tracking system misalignment requires a careful analysis of the infrastructure supporting the tracking system.

The OT and IT stations hang from a common stainless steel structure ("Bridge"), as shown in Fig. 4.6. The Bridge is 18 meters long, 1.5 m wide and installed on 10 pillars that are 7 meters high. The pillars of the bridge are anchored to a concrete platform. The accuracy in the Bridge construction is of the order of 2 mm in the nominal detector position. At the top, the Bridge is connected to the magnet yoke. The movement of the OT Bridge due to the magnet activity was monitored during a dedicated magnet test using the RASNIK system. When the magnet ramps up the Bridge moves by about 200 μm in the z direction (see Fig. 6.1). This movement is reproducible.

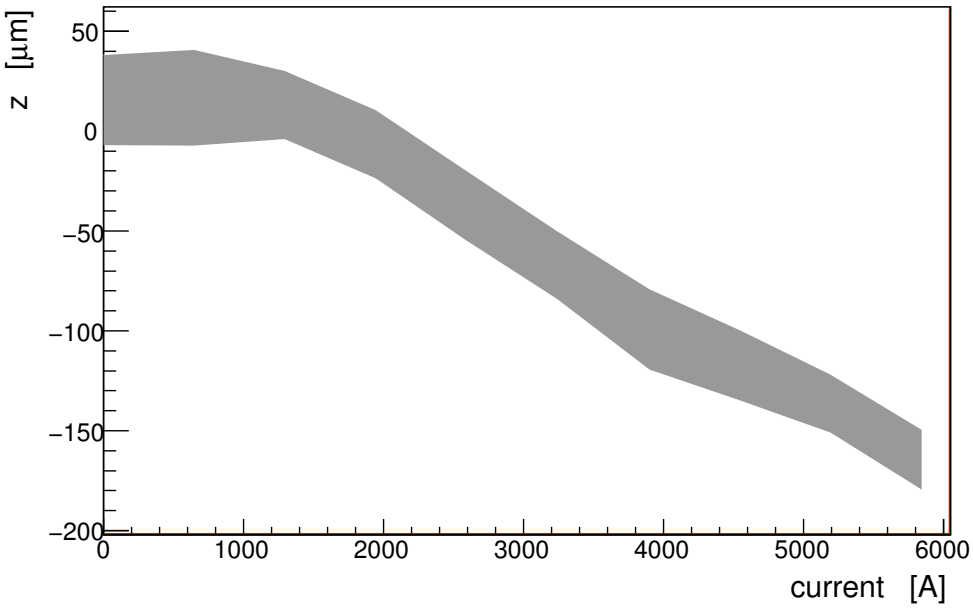

Figure 6.1: *Translation in z of the quadrant Q13 of T3 as function of the current in the magnet during the ramping operations.*

All OT C-Frames were surveyed by means of theodolites, in combination with reflective targets that are mounted onto each straw-tube module dowel pin. As a result, the positions of all dowel pins are known with 0.5 mm accuracy. Therefore, in the remainder of this chapter, the effect of misalignments of this order of magnitude will be studied.
The relative measurement between sub-detectors (i.e. OT and VELO) are known with a larger uncertainties of about 1 mm, since the survey measurements of the OT and the VELO are mostly based on different reference points.

6.2 Tracks, software alignment and weak modes

The track model is here shortly summarized and the basic idea of the alignment method is given.

6.2.1 Track model and momentum measurement

The track model is the parametrization of the charged particle trajectory. In a stationary field in vacuum, the motion of a charged particle is completely described by its initial position, charge and momentum. For a given value of z, the track parameters are:

$$x;\ y;\ t_x;\ t_y;\ \frac{q}{pc} \tag{6.1}$$

where x and y are the coordinates orthogonal to the beam, t_x and t_y are the track slopes in the xz and yz-plane respectively and q/pc is the ratio between the charge and the momentum.

The particle momentum is measured by its curvature in the magnetic field. Since the y component of the field is dominant, the charged particle bends mainly in the the xz-plane and therefore the variation of t_x is the most significant. In the approximation of small curvature, the change of slope can be written as:

$$\Delta t_x \ \approx\ \frac{q}{c\sqrt{p_x^2+p_z^2}}\ I_B, \tag{6.2}$$

where $I_B = \int B_y dz$ is the integral of the y component of the B-field along the trajectory.

The curvature measurement resolution is proportional to the hit resolution of the tracking detectors and inversely proportional to the field integral. Since the curvature decreases for increasing momentum, the momentum resolution [1]deteriorates for high energy tracks. This is illustrated in Fig. 6.2, which shows the momentum resolution of the reconstructed π^+ in the $B_d \to \pi\pi$ decay as function of its momentum. The momentum resolution is obtained by comparing the reconstructed and the "true" momentum, namely from the width of the distribution of:

$$\frac{\Delta p}{p}(\%) = 100\ \frac{p_{rec}-p_{true}}{p_{true}}, \tag{6.3}$$

where p_{rec} and p_{true} are the reconstructed and true momentum respectively.

6.2.2 Alignment strategy

Misalignments between detector elements can be resolved and corrected via software, updating their geometric position. To determine those corrections a minimum χ^2

[1]For low momentum tracks, the curvature resolution is dominated by the effect of multiple scattering.

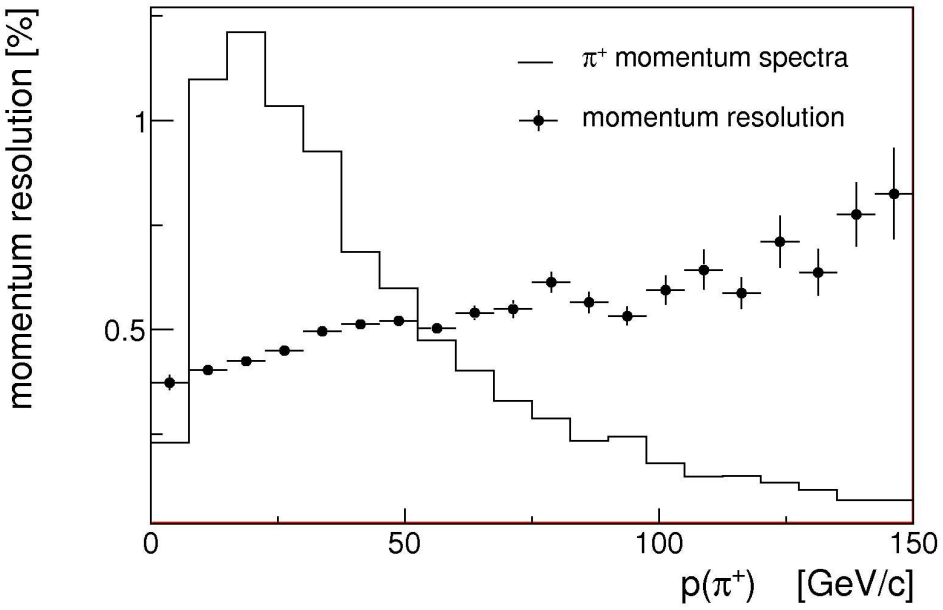

Figure 6.2: *Momentum resolution for the reconstructed muons in $B_d \to \pi\pi$ as function of π^+ momentum, superimposed on the π^+ momentum distribution.*

alignment method is adopted [70–73]. The alignment method takes a sample of tracks and minimizes the total χ^2 with respect to the alignment parameters.

To illustrate the performance of the software alignment, in Fig. 6.3 the mass resolution for the $J/\psi \to \mu\mu$ is shown as a function of the J/ψ momentum in three different scenarios:

- Default geometry (open stars). About 40k $J/\psi \to \mu\mu$ events were reconstructed with the ideal geometry, which implies that all detector elements are positioned at their exact design location.

- Random misalignment scenario of OT and IT (full dots). About 40k $J/\psi \to \mu\mu$ events were reconstructed with a misaligned geometry, obtained by adding corrections extracted by a Gaussian distribution having a width as large as the single-hit resolution of the sub-detectors. For low momentum the mass resolution is about 10 MeV which is comparable with the one measured with default geometry, (because the curvature of low momentum particle is large compared to the misalignment scale). For high momentum the curvature of the muon is small and the effect of misalignment leads to a degradation in the mass resolution up to ≈ 30 MeV.

- Alignment of OT and IT (open circle). The alignment algorithm was used to determine and correct the OT and IT misalignments in the scenario above.

The mass resolution after alignment well approximates the ideal scenario over the full J/ψ momentum range.

The result in Fig. 6.3 shows how the degradation of the mass resolution due to random misalignment can be corrected.

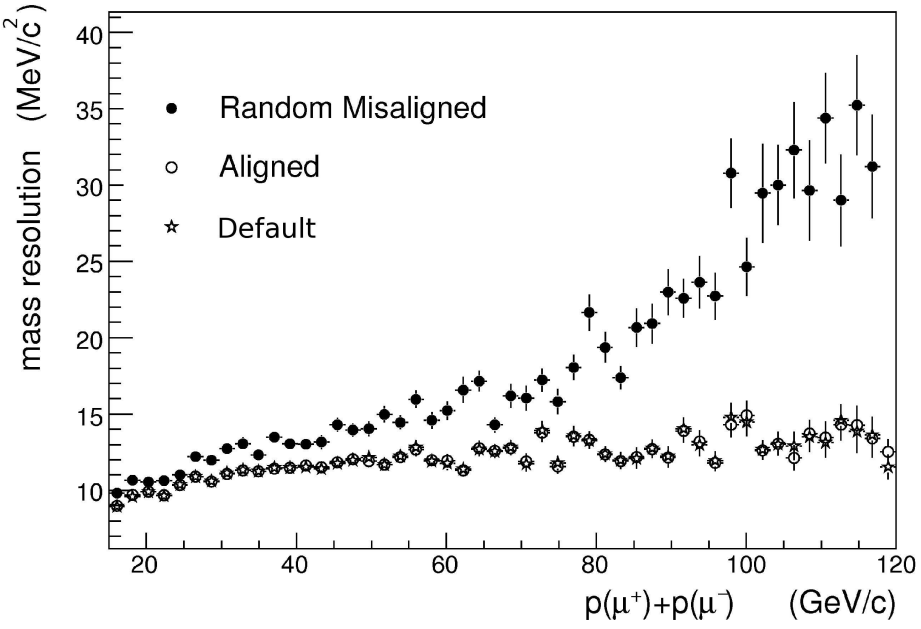

Figure 6.3: *J/ψ mass resolution for $J/\psi \to \mu\mu$ as function of the sum of the muons momentum. Full dots: events reconstructed with a random misalignment geometry. Open dots: events reconstructed after alignment. Open stars: events reconstructed in default geometry.*

6.3 Weak modes relevant for momentum measurement

The minimum χ^2 method cannot resolve misalignments to which the track χ^2 is insensitive. Such scenarios generally correspond to common movements of detector elements. They are sometimes called weak modes because they can be identified by an eigenvalue analysis of the linear system that is solved to compute the alignment constant [70]. Weak modes are an important challenge for track-based alignment algorithms. The best known weak modes are global transformations; rotations and shearings of the detector which mildly affect physics measurements. In this chapter, however, weak modes that do affect the momentum measurement, and therefore the physics potential of LHCb, are studied. As explained in Sec. 6.2.1, charged particle momenta in LHCb are essentially measured by the change of their the slope

("kick" of the particle) in the xz-plane when they traverse the magnet. Consequently a displacement of the tracking system behind the magnet relative to the VELO, affects the momentum measurement. By an eigenvalue analysis [70] the following weak modes relevant to the momentum measurement were identified:

- Common x-translation of the tracking station (OT and IT) with a scale factor 1, 0.85 and 0.625 for stations T3, T2 and T1 respectively. The scale factors correspond to the geometrical configuration with which the tracking stations are pointing to the focal plane of the magnet (z_{magnet}=5.15 m [74]).

- Common z-translation of the tracking station (OT and IT) with a scale factor 1, 0.5 and 0.25 for stations T3, T2 and T1 respectively. If the detector is stretched along z, the curvature is reduced and therefore the assigned particle momentum is overestimated. The expected behavior is a change in the momentum scale and as such this effect is similar to the one resulting by a B-field rescaling (see 6.7).

A schematic view of the weak modes is shown in Fig. 6.3. For these weak modes several different misaligned scenarios were considered. Those are described in Tab. 6.1. To illustrate that these are really weak modes for the alignment method, the χ^2 of the track fit is compared for a sample of 40000 tracks reconstructed in four different alignment scenario: unbiased sample, misaligned sample corresponding to the scenario 5 in Tab. 6.1(a), misaligned sample corresponding to the scenario 5 in Tab. 6.1(b) and the misaligned realistic random scenario described in Sec. 6.2.2. The scale involved in all of those three misalignment scenarios is comparable. In Fig. 6.5, the distribution of the track χ^2 divided by the number of degrees of freedom is shown for each scenario. The scenarios corresponding to the weak modes almost perfectly overlap with the unbiased sample while in the case of the random misalignment the distribution differs significantly. This illustrates why a minimum χ^2 alignment method cannot resolve the weak modes.

Δx Scenarios	$T_3(\mu m)$	$T_2(\mu m)$	$T_1(\mu m)$
0	0	0	0
1	100	85	62
2	200	170	125
3	300	255	187
4	400	340	250
5	500	425	312

Δz Scenarios	$T_3(\mu m)$	$T_2(\mu m)$	$T_1(\mu m)$
0	0	0	0
1	100	50	25
2	200	100	50
3	300	150	75
4	400	200	100
5	500	250	125

Table 6.1: *From left to right, table (a) and (b): misalignment scenarios used for common translation in x and z respectively.*

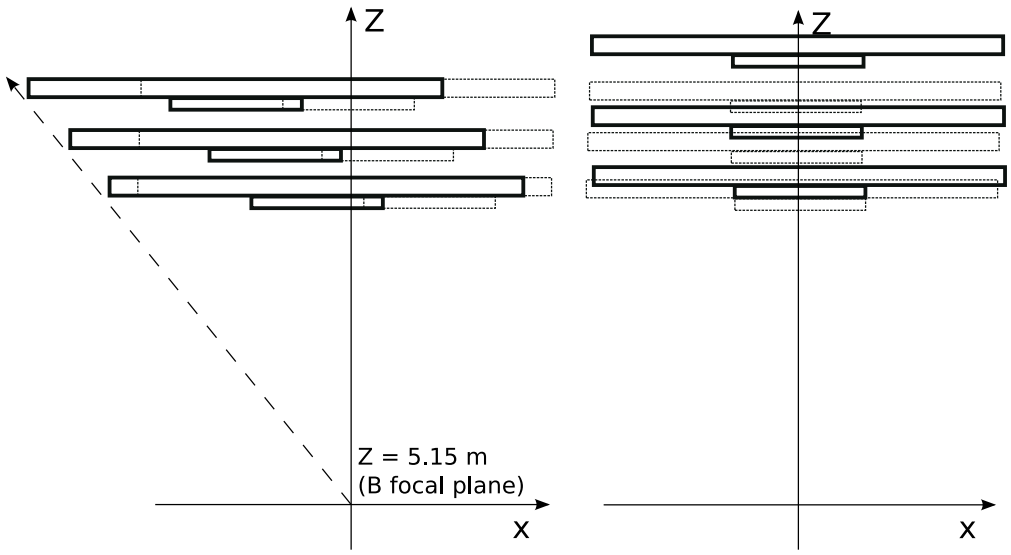

(a) Common translation in x (b) Common translation in z

Figure 6.4: *Illustration of the weak modes of the spectrometer on an exaggerated scale. On the left: common translation in x with a scale factor 1, 0.85 and 0.625 for stations 3, 2 and 1 respectively. The scale factor is such that the whole system is pointing to the focal plane of the magnet. On the right: common translation in z with a scale factor 1, 0.5 and 0.25 for stations 3, 2 and 1 respectively.*

6.4 Bias in the invariant mass

To understand the effect of the weak modes on the mass resolution the effect on the track parameters needs to be analyzed first. The relevant track parameter sensitive to the misalignment is the curvature ω, which is defined as:

$$\omega = \frac{q}{p}. \tag{6.4}$$

Due to the chosen units, $\omega_+ = 1/p_+$ for positive tracks and $\omega_- = -1/p_-$ for negative tracks. The aim of this section is to provide a formal way to add the effect of an ω bias on the invariant mass.
For the remainder of this chapter c=1 and q is measured in units of the electron charge. The momentum is measured in GeV.

6.4.1 Track sample

In Fig. 6.6 the distribution of ω for a sample of long charged tracks is shown. By definition the distribution is split in two halves for negative and positive tracks. Low energy tracks have a large value of ω while for high energy tracks ω is close to zero. The study in this section is performed only on high energy tracks with

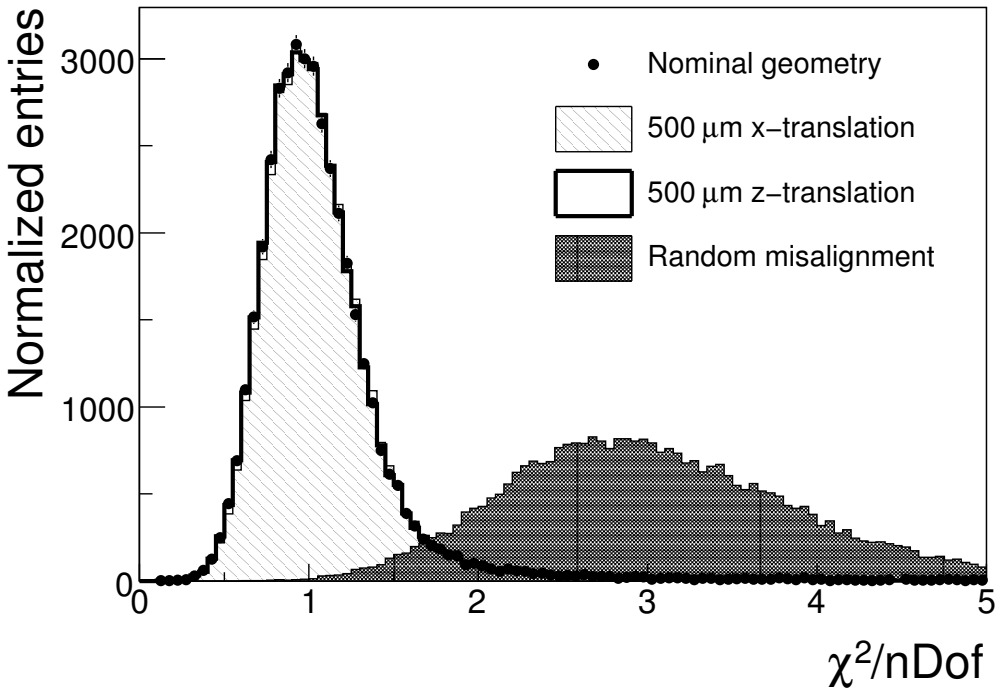

Figure 6.5: *The $\chi^2/Ndof$ distribution of the track fit for $J/\psi \rightarrow \mu\mu$ in four different scenarios: default geometry (full dots), common x-translation of 500 μm (hatched), common z-translation of 500 μm (filled) and realistic random misalignment (grey).*

a value of ω ranging between $\pm 0.2\ GeV^{-1}$, which correspond to tracks having at least a momentum of 5 GeV. The reason of this cut is to select tracks relevant for B-physics. Moreover, low energy particles are significantly affected by multiple scattering which can hide misalignment effects.

6.4.2 Bias in ω

When the detector is misaligned, the reconstructed value of ω is biased. Let us indicate the biased value with $\omega^{'}$ and the one measured with an default geometry with ω_0. No Monte Carlo information is used in this study but only the variation in the reconstructed ω with different alignment scenarios. The following 2-parameter model to study the effects of misalignment is considered:

$$\omega^{'} = \omega_0 + \Delta\omega + \omega_0\alpha. \tag{6.5}$$

The term $\Delta\omega$ corresponds to an offset and α is dimensionless. The bias $\Delta\omega$ is referred to below as "curvature bias"; the bias $\omega_0\alpha$ is referred to as "curvature scale" bias.

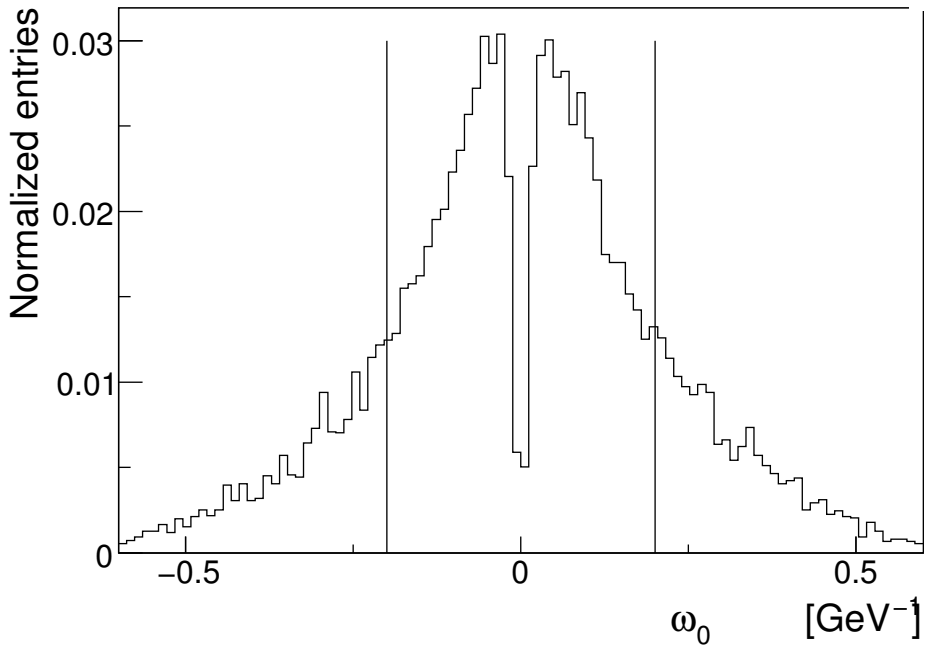

Figure 6.6: *Distribution of ω for an unbiased sample (default geometry) of long tracks coming from a B event. The lines indicates the range in ω_0 for the tracks used in this study.*

6.4.3 Curvature bias

The two body decay invariant mass is:

$$m_{inv}^2 = m_-^2 + m_+^2 + 2(E_-E_+ - p_-p_+cos\theta) \tag{6.6}$$

where m_- and m_+ are the rest mass of the daughters particles, p_- and p_+ their corresponding momenta and θ the opening angle (the label $+$ and $-$ is used to indicate positive and negative tracks). Since only tracks with momentum larger than 5 GeV are taken into account, the mass is negligible to a very good approximation. Therefore the Eq. 6.6 simplifies:

$$m_{inv}^2 \approx 2p_-p_+(1 - cos\theta) \tag{6.7}$$

From the definitions given in Eq. 6.5 and Eq. 6.6 a curvature bias $\Delta\omega$ on ω_0 can be translated into a bias in the invariant mass. Using the definition given in 6.4 the biased momentum is:

$$p_\pm^{'} = \frac{\pm 1}{\omega_0 + \Delta\omega}, \tag{6.8}$$

which for $|\Delta\omega| \ll |\omega_0|$ can be approximated by

$$p_\pm^{'} \approx p_\pm(1 \mp \frac{\Delta\omega}{\omega_0}). \tag{6.9}$$

From the equation above, the biased value of the invariant mass $m^{'}$ can be determined. For a two body decay, substituting $p^{'}_{-}$ and $p^{'}_{+}$ in Eq. 6.7 the biased invariant mass $m^{'2}$ is:

$$m^{'2} \approx (1 + (p_{-} - p_{+})\Delta\omega)\ m^2, \tag{6.10}$$

which result in a bias in the mass

$$m^{'} \approx \left(1 + \frac{(p_{-} - p_{+})}{2}\Delta\omega\right)\ m. \tag{6.11}$$

Consequently, $\Delta\omega$ leads to an observable bias on the invariant mass proportional to the difference in momentum between the daughter particles in a two body decay.

6.4.4 Curvature scale bias

The term α leads to a bias in the momentum and mass scale. As done previously, let us indicate with p the track momentum. The biased momentum is:

$$p^{'}_{\pm} = \frac{\pm 1}{\omega_0 + \omega_0\ \alpha}. \tag{6.12}$$

Following the same steps as in Sec. 6.4.3, the expression for the biased invariant mass is:

$$m^{'2} \approx (1 - 2\alpha)\ m^2 \tag{6.13}$$

and therefore:

$$m^{'} \approx (1 - \alpha)\ m \tag{6.14}$$

6.5 Parametrization of $\Delta\omega$ and α as function of misalignment

In the previous section the model to characterize misalignment scenarios was described. To give this model predictive power the model parameters are here measured for the weak mode misaligned scenarios introduced in Sec. 6.3. The adopted misalignment scenarios are described in Tab. 6.3. Those scenarios were chosen according to the intrinsic sub-detector resolution and the sub-detectors alignment's precision. The misalignment applied at T3 defines the misalignment scale.

6.5.1 Method

To study the bias in track curvature ω for a given misalignment scenario, the difference $\omega^{'} - \omega_0$ as function of ω_0 for a set of selected tracks is considered. The study was performed using a sample of 95000 long tracks with the quality requirements described in 6.4.1. The value of $\omega^{'}$ was determined per track after refitting with a modified geometry.

6.5.2 Common x translation

The correlation between $\omega^{'} - \omega_0$ and ω_0 was studied using the misalignment scenarios from 0 to 5 in Tab. 6.1(a). In Fig. 6.7(a) the 2D distributions is illustrated for scenario 5, corresponding to the larger translation on x. The horizontal line correspond to the unbiased ω. For each scenario, this 2D distribution was sliced in 24 bins in x and each slice was fitted with a Gaussian. The mean and the sigma of each Gaussian fit are plotted in Fig. 6.7(b). A linear fit was finally done to measure $\Delta\omega$ and α (see Eq. 6.5).

No significant slope is observed and consequently α is negligible. Using all the off-

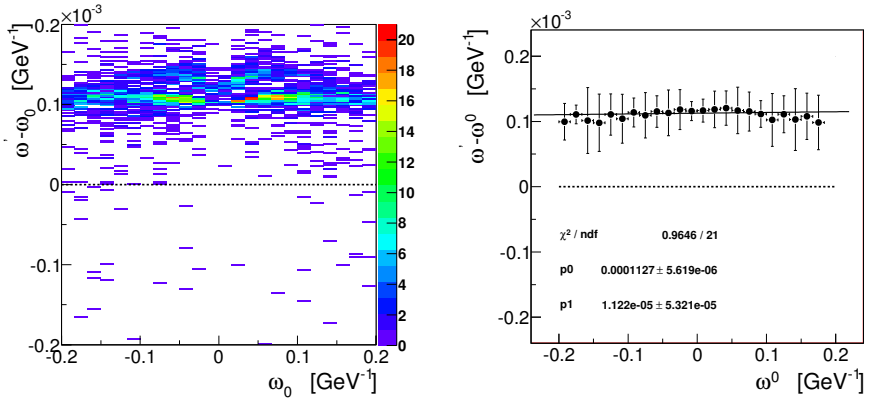

(a) Scatter plot (b) Fit of slices

Figure 6.7: *Correlation between $\omega^{'} - \omega_0$ for common x translations of 500 μm at tracker station T3. (a) scatter plot of all entries. (b) Mean value and error of $\omega^{'} - \omega_0$ per bin in ω_0.*

sets obtained from the misalignment scenarios of Tab. 6.1(a) the correlation between $\Delta\omega$ and the misalignment scales was obtained and shown in Fig. 6.8(a). As can be seen in the figure, the offset ($\Delta\omega$) increases with the misalignment scale.

The relation between the curvature bias and the x-translation is linear with a slope

$$\frac{\mathrm{d}\Delta\omega}{\mathrm{d}\Delta x} = (2.20 \pm 0.05) \times 10^{-7} (\mu m^{-1} GeV^{-1}). \tag{6.15}$$

This result has to be interpreted in this way: if for example a translation in x of the T stations of 300 μm is applied, the corresponding value of $\Delta\omega \approx 0.06 \times 10^{-3}\ GeV^{-1}$. The bias in the reconstructed mass is then $(p_- - p_+)\Delta\omega\ m$. The argument can be also turned around: from an observed bias on the mass, one can estimate the x-translation at T3 responsible for the measured bias.

Translation towards negative value of x result in a negative value of $\Delta\omega$ with the same dependence on the misalignment scale as in Eq. 6.15. If the B-Field polarity

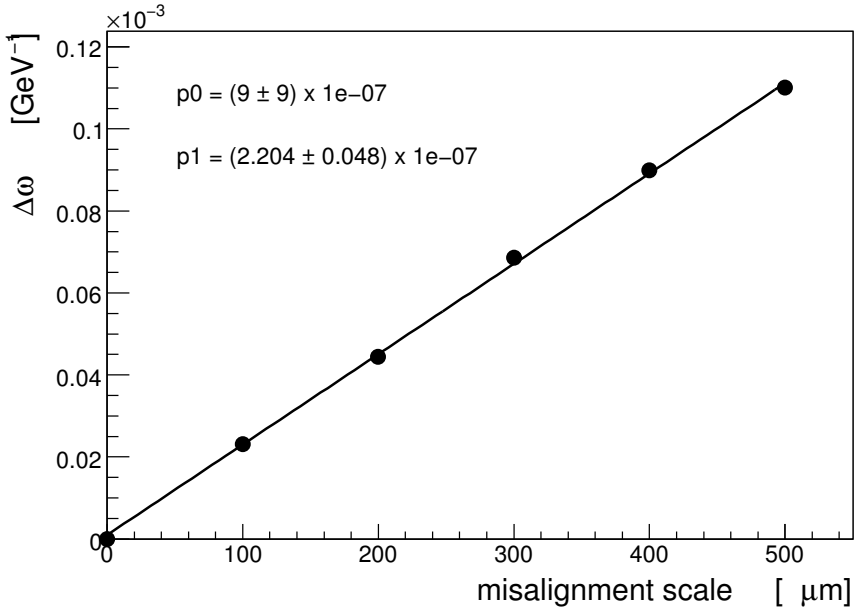

(a) x translation

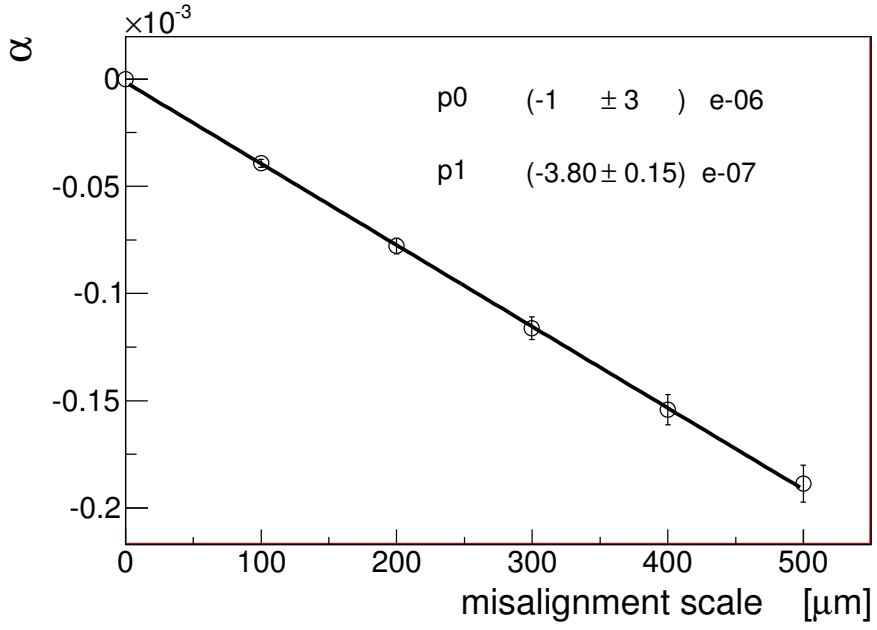

(b) z translation

Figure 6.8: *Misalignment parameters as function of the misalignment scale. (a) $\Delta\omega$ versus x translation. (b) α versus z translation.*

is flipped $(B_x, B_y, B_z) \rightarrow (B_x, -B_y, B_z)$ the sign of the bias is inverted.

6.5.3 Common z translation

In a similar way as described in Sec. 6.5.2 the z-translation was studied using the misalignment scenarios from 0 to 5 in Tab. 6.1(b). In Fig. 6.9(a) the 2D distributions is illustrated for scenario 5, corresponding to the larger translation on z. The horizontal line correspond to the unbias ω. For each scenario, this 2D distribution was sliced in 24 bins in z and each slice was fitted with a Gaussian. The mean and the sigma of each Gaussian fit are plotted in Fig. 6.9(b). A linear fit was finally done to measure $\Delta\omega$ and α (see Eq. 6.5).

Since there is no offset at $\omega_0 = 0$ but an increasing slope, the dominant effect is

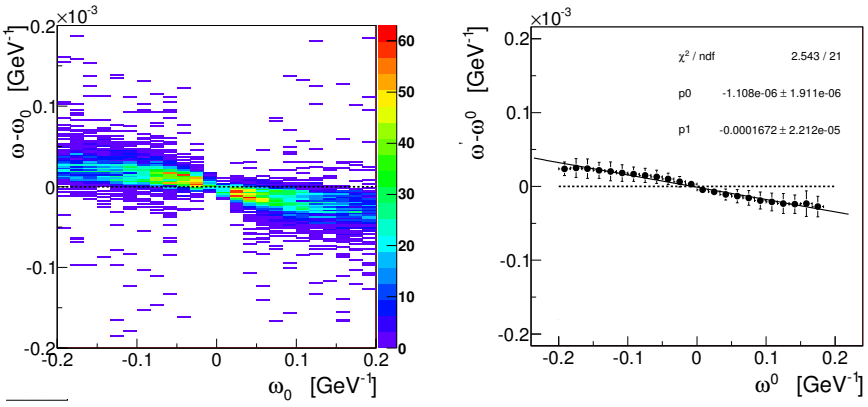

(a) Scatter plot (b) Fit of slices

Figure 6.9: *Correlation between $\omega' - \omega_0$ for common z translations of 500 μm at tracker station T3. (a) scatter plot of all entries. (b) Mean value and error of $\omega' - \omega_0$ per bin in ω_0.*

due to α. Using the information from all the 6 scenarios, the correlation between α and the scale of the applied misalignment was obtained and shown in Fig. 6.8(b). The error bars reflect the width of the $\omega - \omega_0$ distribution. The fact that the error bars increases with increasing misalignment scale, shows that the dependence on $\Delta\omega$ on the misalignment is more complex that the simplified model used in this study: besides an ω bias, there is also an effect on the resolution. However, for such small misalignment this effect is negligible compared to the actual curvature resolution. From the linear fit the relation obtained is:

$$\frac{\mathrm{d}\alpha}{\mathrm{d}\Delta z} = (-3.80 \pm 0.15) \times 10^{-7} (\mu m^{-1}). \tag{6.16}$$

This result has to be interpreted in this way: for a translation in z of the T station of about 300 microns, the corresponding value of $\alpha \approx -0.1 \times 10^{-3}$. This leads to a bias in the reconstructed mass of αm, which mean a positive mass shift proportional

to the mass of the reconstructed mother particle.
Translation towards negative value of z result in a positive value of α with the same dependence on the misalignment scale as in Eq. 6.16. If the B-Field polarity is flipped $(B_x, B_y, B_z) \rightarrow (B_x, -B_y, B_z)$ the bias remain the same.

6.6 Effect on $J/\psi \rightarrow \mu\mu$ and $B_d \rightarrow \pi\pi$ mass

In the previous section the systematic effect of misalignment was studied on long tracks of high momentum charged particles. The effect on the invariant mass for two body decays was predicted as function of $\Delta\omega$ (curvature bias, see Eq. 6.11) and α (curvature scale bias, see Eq. 6.14) which are the two parameters of the adopted misalignment model.

In this section the effect on the mass resolution is studied on reconstructed two body decays. Two channels are chosen:

- $J/\psi \rightarrow \mu\mu$, important for calibration of the detector with first data. The expected number of events per year is 2.29×10^9 [75]. A standard preselection is applied.
- $B_d \rightarrow \pi\pi$, important as a control channel for the $B_s \rightarrow \mu^+\mu^-$ analysis. The expected number of events per year is about 1.7×10^4 events [76]. A standard preselection is applied.

6.6.1 Common translation along x of OT/IT (curvature bias)

Due to geometry of the tracking system and B-field, in a two body decay (i.e. $B_d \rightarrow \pi\pi$) a positive translation along the x direction of the tracking stations leads to a overestimation of the π^- momentum and an underestimation of the π^+ momentum. This imbalance in the momentum is clearly shown in Fig. 6.10 in which the quantity defined in Eq. 6.3 is plotted separately for negative and positive pions for default geometry (grey) and a translation along x of 500 μm (continuous line). The distributions for events reconstructed with default geometry for π^- and π^+ are symmetric and peaked at zero. The first order effect is therefore an offset in the particle momentum but a second order effect is responsible of the formation of a asymmetrical tail, which mildly affect the momentum resolution.

On Fig. 6.10(c) the mean invariant mass is shown as function of $p_- - p_+$ for $B_d \rightarrow \pi\pi$ events: the open circles correspond to the default geometry and the full circles to a translation along x of 500 μm. The slope corresponds to $\frac{\Delta\omega}{2}m$ and the value of $\Delta\omega$ in this particular scenario is $(1.1 \pm 0.2) \times 10^{-4}\ GeV^{-1}$. A bias affects the average mass resolution if integrated over the momentum difference. Using all the scenarios of Tab. 6.1(a) the average mass resolution can be studied as function of the misalignment scale. The mass resolution σ_m was measured by fitting the mass

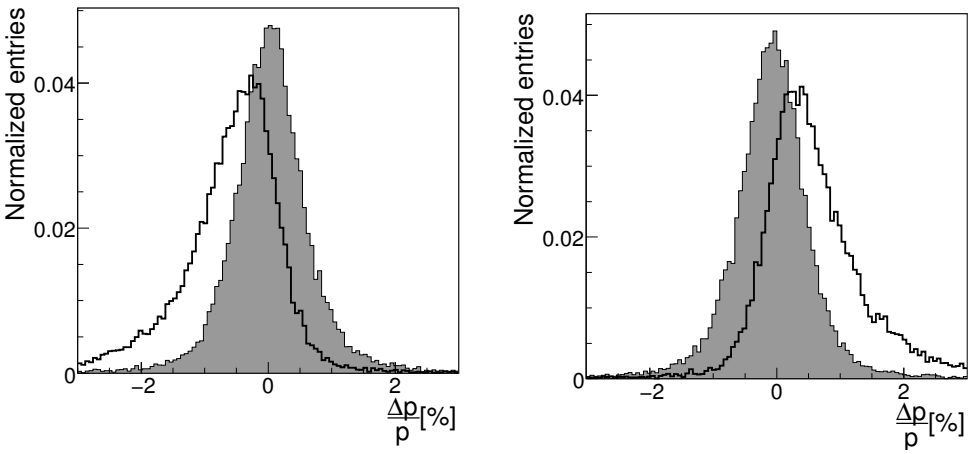

(a) π^- (b) π^+

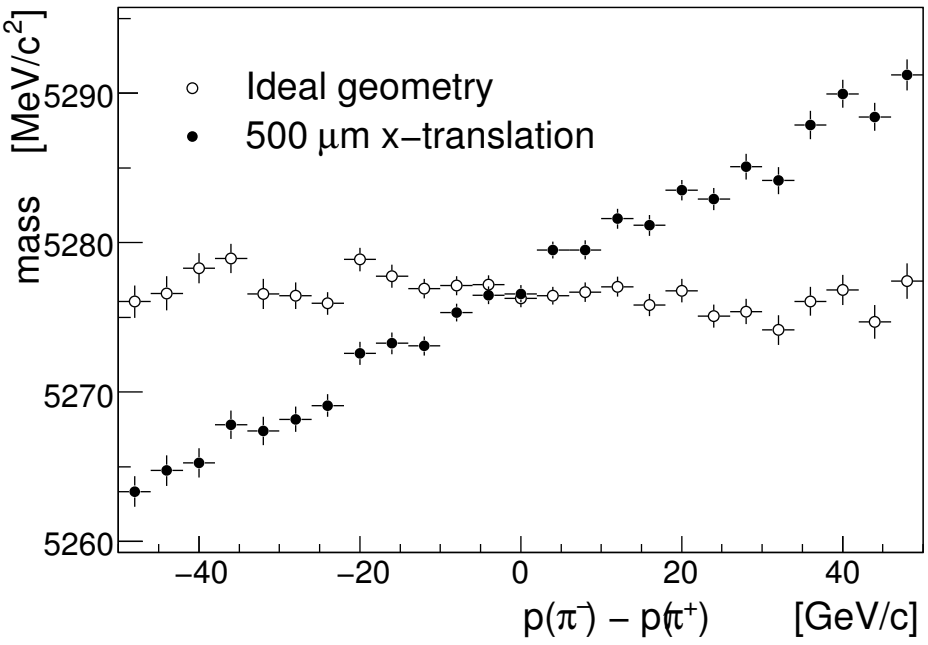

(c) $B_d \to \pi\pi$

Figure 6.10: *Upper panel: Comparison of the reconstructed momentum with default geometry (grey area) and a translation along x of 500 μm (thick line). (a): $\frac{\Delta p}{p}$ for π^- in $B_d \to \pi\pi$. (b): $\frac{\Delta p}{p}$ for π^+ in $B_d \to \pi\pi$. Lower panel: Mass as function of p1-p2 with default geometry (empty dots) and a translation along x of 500 μm (full dots) for $B_d \to \pi\pi$ events.*

distribution with a Gaussian and the associated error is the one returned by the fit. The resulting correlation is shown in Fig. 6.11 for $B_d \to \pi\pi$ and $J/\psi \to \mu\mu$. The points follow a straight line.

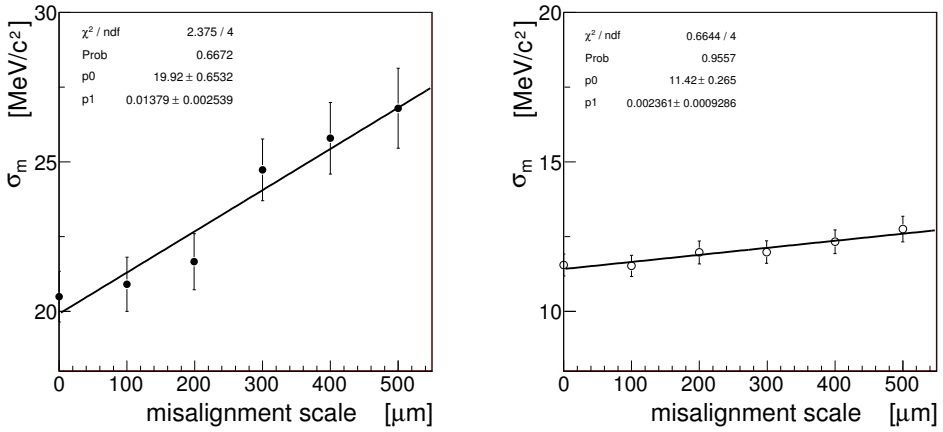

(a) $B_d \to \pi\pi$ (b) $J/\psi \to \mu\mu$

Figure 6.11: *Mass resolution of B_d (a) and J/ψ (b) as function of the misalignment scale for a common x translation.*

6.6.2 Common translation along z of OT/IT (curvature scale bias)

A common translation of the T stations along z (namely an increase in the distance between the VELO and the T stations) stretches the reconstructed particle trajectory in the xz-plane and rescales the momentum independently from the charge. For instance, in Fig. 6.12 the momentum resolution of $J/\psi \to \mu\mu$ candidates is shown for default geometry (full dots), a translation along z of 2 mm (thick line) and for a translation in z of 10 mm (dashed area). Two entries per event (μ^+ and μ^- are here distributed together). The last two extreme scenarios were chosen only to qualitatively show the effect on the momentum. With a shift of 2 mm the bias in the momentum is noticeable. The momentum is biased independently of the charge of the daughters. The third scenario shows that for large misalignment scale a resolution effect is also significant since the width of the peak becomes larger.

In the Fig. 6.12(b) the mean invariant mass is shown as function of $p_1 - p_2$ for a translation in z of 500 μm (full circle) and default geometry (open circle). In this example, the resulting mass shift is of 1.2 MeV for B_d (0.8 MeV for J/ψ).

Using all the scenarios of Tab. 6.1(b) the invariant mass can be studied as function

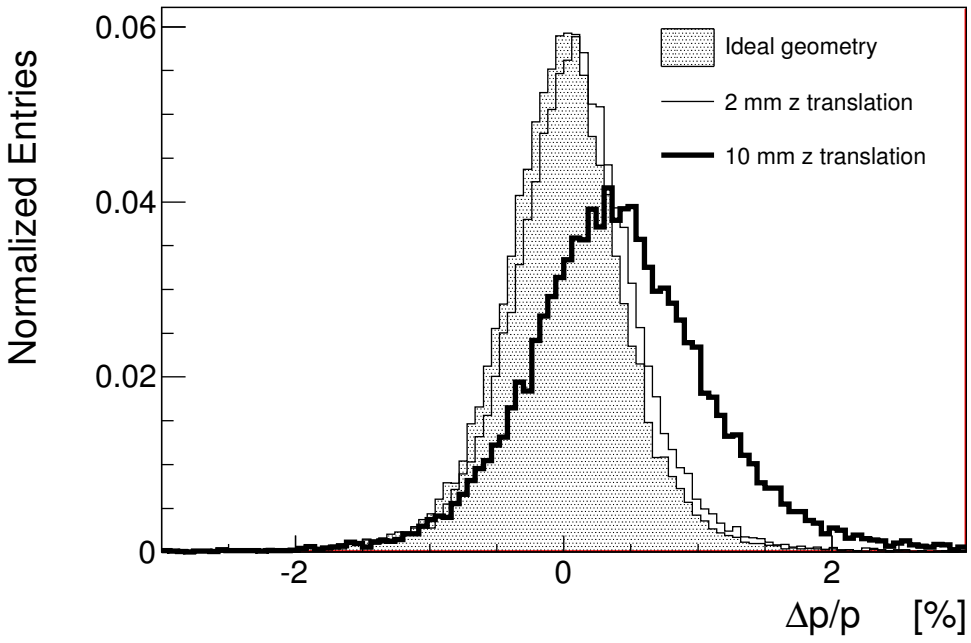

(a) Momentum bias

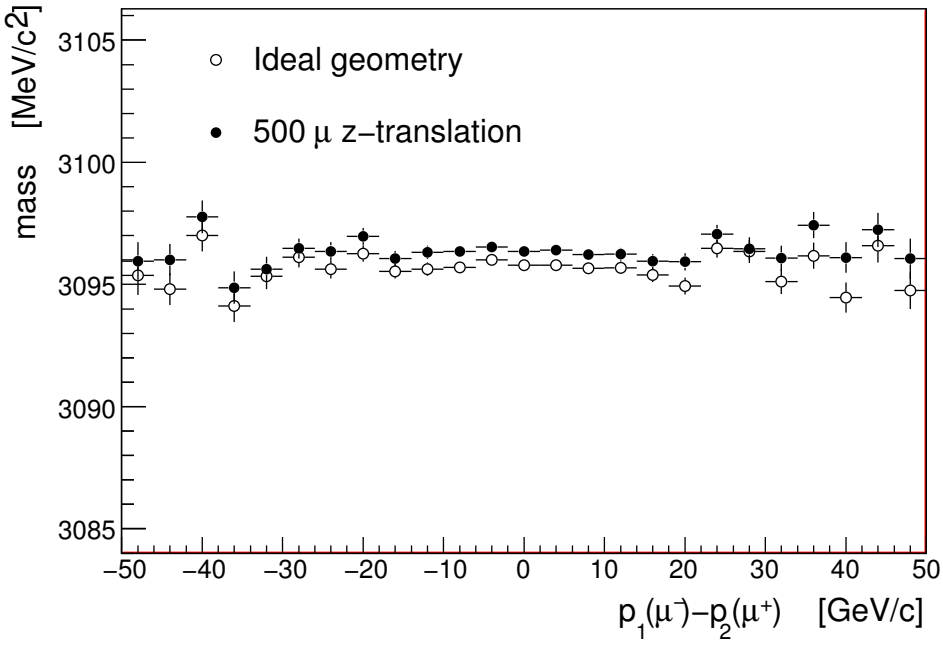

(b) Mass bias

Figure 6.12: *(a) Momentum resolution for $J/\psi \to \mu\mu$ in three scenarios: default geometry (shadow), a translation along z of 2 mm (continuous line) and 10 mm (thick continuous line). (b) Mass as function of $p(\pi^-)$-$p(\pi^+)$ with default geometry (empty dots) and a translation along z of 500 μm (full dots) for $J/\psi \to \mu\mu$ events.*

of the misalignment scale. The invariant mass m' is measured by fitting the mass distribution with a Gaussian, the associated error is the one returned by the fit. The resulting linear correlation is shown in Figs. 6.13(a) and 6.13(b) for $B_d \to \pi\pi$ and $J/\psi \to \mu\mu$.

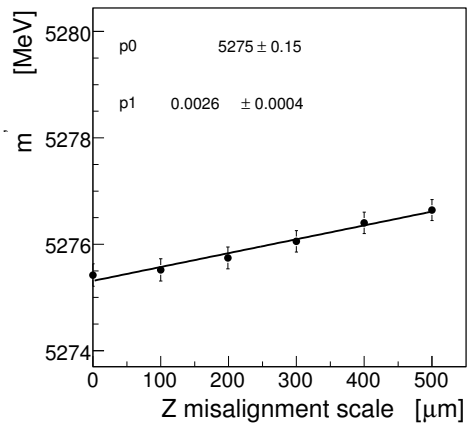

(a) $B_d \to \pi\pi$

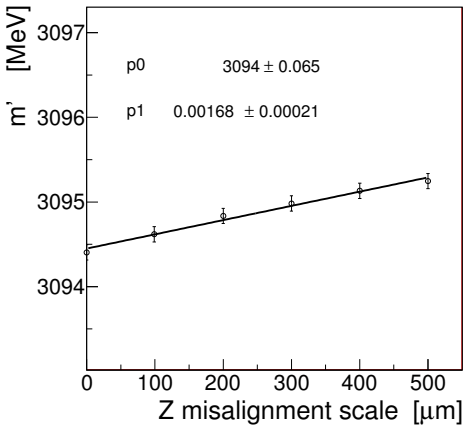

(b) $J/\psi \to \mu\mu$

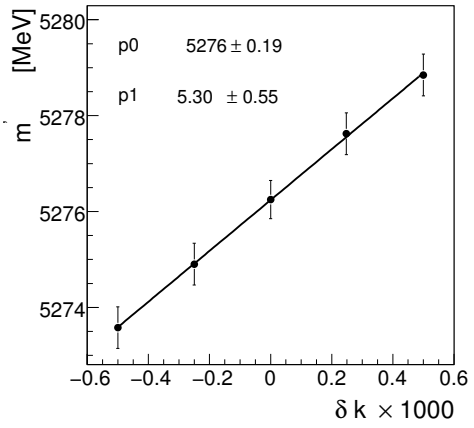

(c) $B_d \to \pi\pi$

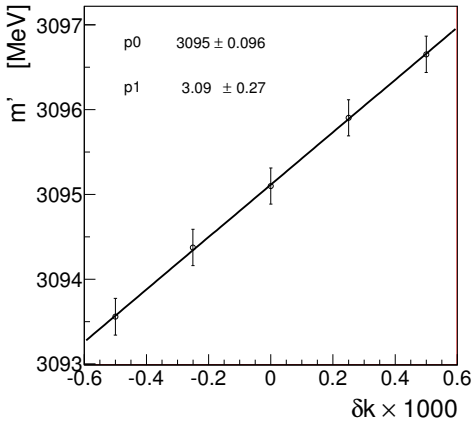

(d) $J/\psi \to \mu\mu$

Figure 6.13: *Invariant mass of B_d (full dots) and J/ψ (open circle) as function of the misalignment scale for a z translation (panels a and b) and the B-field scale (panels c and d).*

6.7 B-field scale and Z-Common translation

The magnetic field is usually measured on a grid. Numerical methods are used to interpolate the grid and to integrate the field along the trajectory. In LHCb initial studies of the field map were done using a grid of values built by combining a simulated B-field (using TOSCA [77]) and measurements performed with Hall probes. Using the simulation, the measured field was extrapolated in the region in which the probes positioning did not allow obtaining measurements. By an analysis of the discrepancy between the simulated field and the measurement, the accuracy of the magnetic field was estimated to be better than 10^{-3} T (see Sec. 3.1). However during the running operation the scale of the field is not constant and in the offline reconstruction several monitoring variables (e.g. the current) determine a different scale factor per run.

The aim of this section is to analyze the systematic effect on the mass due to a rescale of the magnetic field and its similarity with a z translation of the tracking stations behind the magnet.

6.7.1 Bias on the mass due to a B-field rescaling

The determination of the momentum of a charge particle was described in Sec. 6.2.1. The Eq. 6.2 show that the variation in the slope on the xz-plane is proportional to the integrated magnetic field. As a first approximation the effect of the B-field rescaling can be parametrized as:

$$I_B^{'} = (1 + \delta k) I_B \tag{6.17}$$

The variation of t_x is therefore:

$$\Delta t_x \;=\; \frac{q}{\sqrt{p_x^2 + p_z^2}} I_B^{'}. \tag{6.18}$$

Consequently the biased momentum becomes:

$$p^{'} = (1 + \delta k) p \tag{6.19}$$

Following the same steps described in 6.4.3 the invariant mass is:

$$m^{2'} \approx (1 + 2\delta k) m^2, \tag{6.20}$$

and therefore:

$$m' \approx (1 + \delta k) m. \tag{6.21}$$

The effect on mass due to a B-field scaling is qualitatively the same as a translation of the T stations along z. The bias is proportional to mass of the mother particles as shown in Figs. 6.13(c) and 6.13(d) and the ratio of the slopes comparable to the

	$B_d \to \pi\pi$	$J/\psi \to \mu\mu$
$\mathrm{d}\delta k/\mathrm{d}\Delta z$	$(4.9 \pm 1.0)10^{-7}$ $\mu\mathrm{m}^{-1}$	$(5.5 \pm 0.5)10^{-7}$ $\mu\mathrm{m}^{-1}$

Table 6.2: *Relation between mass bias due to a common z translation and B-field rescaling. The ratio of the slopes in Fig. 6.13 is shown for $B_d \to \pi\pi$ and $J/\psi \to \mu\mu$ events.*

ratio of the B_d and J/ψ invariant mass.

The relation between a B-field rescaling and a common z translation was determined for B_d and J/ψ by the ratio of the slopes in Fig. 6.13 (see Tab. 6.2):

$$\frac{\mathrm{d}\delta k}{\mathrm{d}\Delta z} = (5.3 \pm 1.7)10^{-7}(\,\mu\mathrm{m}^{-1}) \tag{6.22}$$

For example, a z translation of 500 μm of the T stations corresponds to a positive rescaling of 0.026% of the B-field. The bias on the invariant mass is identical, the only additional handle on z-scale is the possibility of aligning with magnet off.

6.8 Outlook

Two not obvious weak modes due to a common displacement of the LHCb tracking stations were studied on long tracks. The study was based on a simple parametrization of the ω bias estimated on the adopted misaligned scenarios.

The effect on the momentum resolution and the invariant mass were estimated on $J/\psi \to \mu\mu$ and $B_d \to \pi\pi$ events. Given the high annual yield, those decays can be used to resolve those common movements.

An extra complication arises from magnetic field scale, which adds an offset in the reconstructed mass of the resonances: this bias is indistinguishable from the bias due to a common translation in z of the tracking system. To a certain extend "magnet off" data can be used to disentangle the two offset contributions, although it requires understanding of how the detector moves in the magnet transition.

The calibration of the mass with control channels on data is important for the background rejection on rare decays analysis as $B_s \to \mu^+\mu^-$, to resolve the $B_d \to hh$ resonances (see Sec. 7.2.3). As a summary plot, the different effects on the J/ψ and B_d mass analyzed in this section are summarized in Figs. 6.14(a) and 6.14(b).

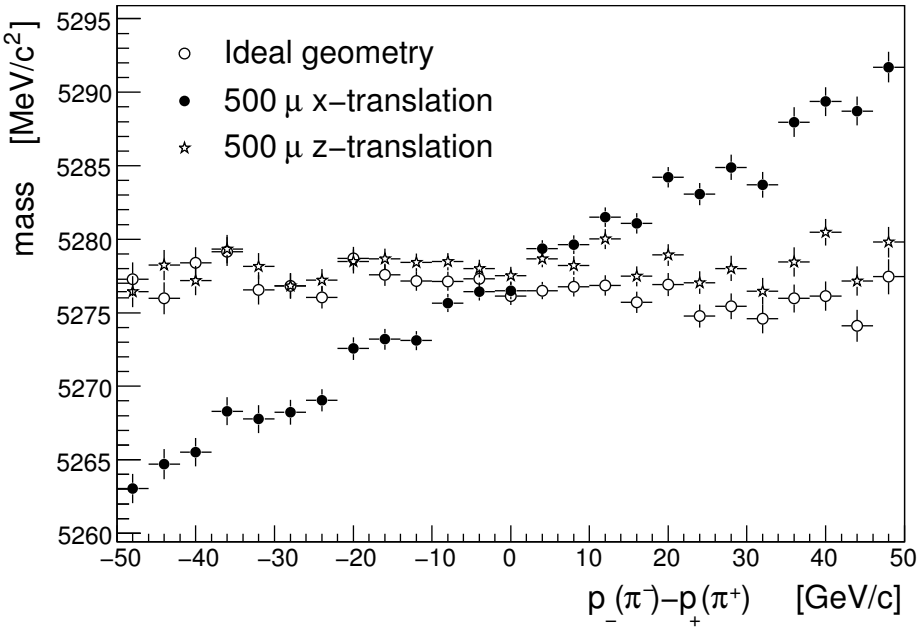

(a) $B_d \to \pi\pi$

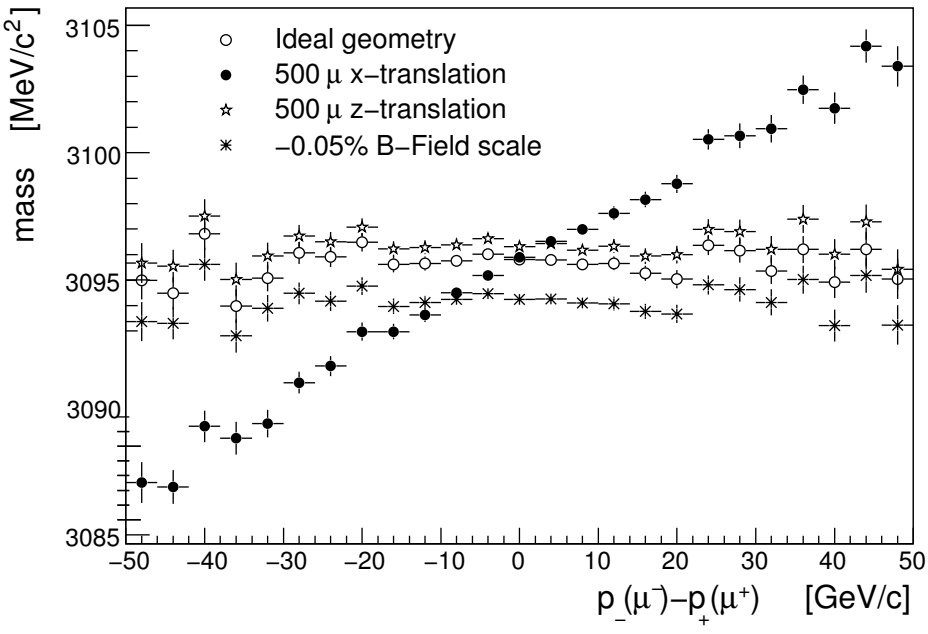

(b) $J/\psi \to \mu\mu$

Figure 6.14: *Summary of the studied mass biases. (a) $B_d \to \pi\pi$. (b) $J/\psi \to \mu\mu$.*

Chapter 7

$B_s \rightarrow \mu\mu$ discovery potential

7.1 Introduction

As discussed in Chapter 2, the SM prediction for the $B_s \rightarrow \mu^+\mu^-$ branching ratio is $(3.35 \pm 0.32) \times 10^{-9}$, and the world best result so far obtained sets an exclusion limit on the branching ratios of 4.7×10^{-8} at 95% confidence level [15]. In the Monte Carlo (MC) study described in this chapter, the LHCb potential of measuring the $B_s \rightarrow \mu^+\mu^-$ branching ratio is investigated.
The analysis consists of the following steps:

- In the first step a loose selection with a high efficiency on the signal is applied in order to reduce the sample to a manageable size (see Sec. 7.3).

- In the second step the selected signal and background events are separated with a likelihood method using three independent observables: a likelihood built with geometrical properties of the decay (Geometrical Likelihood, GL), a PID likelihood to account for mis-identification of muons with pions or kaons (Muon Identification Likelihood, MIL) and the B_s candidate invariant mass (see Sec. 7.4). The branching ratio exclusion limit is then determined using two different statistical techniques.

To make possible the measurement of the $B_s \rightarrow \mu^+\mu^-$ branching ratio on data, several control channels are needed. To normalize the number of B mesons produced the $B^+ \rightarrow J/\psi(\mu^+\mu^-)K^+$ decay is used. The ratio of efficiencies between $B_s \rightarrow \mu^+\mu^-$ and $B^+ \rightarrow J/\psi(\mu^+\mu^-)K^+$ is extracted with a precision of a few percent using a third decay process: $B^0 \rightarrow J/\psi(\mu^+\mu^-)K^{*0}(K\pi)$ (see Sect. 7.8). To calibrate the MC Probability Distribution Function (PDF) of the signal on real data, the $B^0 \rightarrow h^+h^-$ decay events are used. The PDF of the combinatorial background will be extracted using data from the sidebands. The calibration is not discussed here (for further details see [79, 80]).

Sources of systematic uncertainties, such as the B_s fragmentation fraction, the reconstruction efficiency and residual misalignments, are discussed in Sec. 7.9.

7.2 Event simulation and decay reconstruction

Events from proton-proton collisions are generated with the *Pythia* program (version 6.325.2) [82]. Decays of the B-mesons in channels of interest for the LHCb physics program are obtained by interfacing *Pythia* to a specialized decay package, *EvtGen* [83], originally designed for the BaBar collaboration, to model decays of B-hadrons. Pythia settings are tuned to reproduce particle multiplicities at lower energies [35]. Multiple pp collisions in the same bunch crossing (pile-up) are simulated assuming Poisson statistic and by running Pythia for each collision. In LHCb, event generation is performed with a software package called GAUSS which implements a full detector description using the GEANT program. For this analysis GAUSS v30r14 is used. The detector response is simulated in a procedure called digitization, performed with the software package BOOLE. For this analysis BOOLE v12r10 is used. The output has an identical format as the raw detector data.

From raw data, tracks associated to particles produced in the simulation, are reconstructed in the LHCb detector. The tracks are stored in a DST file. The analysis framework supports selection of events and analysis proceeding from further processing of the DST. Track reconstruction and physics analysis are done using the packages BRUNEL v30r17 and DAVINCI v19r13.

7.2.1 Signal

Signal decays are produced following these steps:

- Data samples are obtained from minimum bias events in which a B_s meson is generated.
- The B_s is then forced to decay into two muons using *EvtGen*.
- To accept the di-muon event, each of the two final state muons is required to be within a 10-400 mrad acceptance and pointing towards the detector ($p_z > 0$). The fraction of generated $B_s \rightarrow \mu^+\mu^-$ events that are accepted is $20.0 \pm 0.2\%$.

A total sample of 71200 events, with primary interactions corresponding to a nominal instantaneous LHC luminosity of $2{\times}10^{32}\mathrm{cm}^{-2}\mathrm{s}^{-1}$, are produced in the detector configuration DC06-phys-v2.

7.2.2 Inclusive di-muon background

The main background comes from combinatorial mis-reconstruction of semileptonic B-decays. The di-muon data sets are produced following these steps:

- Data samples are obtained from minimum bias events in which a b-quark is produced as well as two final state muons of opposite charge.
- As for the signal, the final state muons are required to be within the 10-400 $mrad$ acceptance and pointing towards the detector ($p_z > 0$). The fraction of generated events coming from inclusive B-decays that are accepted is 43.7±0.1%.

A total sample of 26.3M events, with primary interactions corresponding to a nominal instantaneous LHC luminosity of $2\times10^{32}\text{cm}^{-2}\text{s}^{-1}$, are produced in the detector configuration DC06-phys-v2. The available sample corresponds to an equivalent luminosity[1] of 0.005 fb^{-1} which ultimately corresponds to about 7 hours of data taking.

7.2.3 $B \to hh$ background

The $B_{d,s} \to h_i^+ h_j^-$ decays (with $h_i^\pm = K_i^\pm, \pi_i^\pm$) have a topology and a phase space of the final state particles similar to the signal. A breakdown of the branching ratios and annual event yields for the $B \to hh$ channels is given in Tab. 7.1 [76]. $B_d \to hh$ events can be mostly rejected with a cut on the invariant mass, due to the separation of 87 MeV between the B_d and B_s peaks, which are resolved with a mass resolution of about 20 MeV (see Sec. 6.6). In Fig. 7.1(a) the mass distributions of the expected $B \to hh$ and $B_s \to \mu^+\mu^-$ events in 2 fb^{-1} of data is shown, using the assumption that the observed final state particles are muons. The $B_s \to \pi\pi$ decay, due to the small mass difference between pions and muons, cannot be separated kinematically. This branching ratio was excluded up to 1.7×10^{-6} at 90%CL [7] and the SM prediction is 24×10^{-9} [84]. In LHCb the $B_s \to \pi\pi$ branching ratio will be measured and its contribution, if not negligible, subtracted.
Moreover, given a probability of ∼1% [45] for a hadron to be mis-identified as a muon, only 0.1 permil of the $B_{d,s} \to h^+h^-$ events could be wrongly reconstructed as $B_s \to \mu^+\mu^-$. In Fig. 7.1(b) the mass distributions of the expected $B \to hh$ and $B_s \to \mu^+\mu^-$ events in 2 fb^{-1} is shown as expected after the particle identification cut

[1]

$$Luminosity_{bkg}[fb^{-1}] = \frac{N_{bkg}}{\alpha_{bkg} \times \epsilon_{bkg}^{tot} \times \sigma} = \frac{26.3 \times 10^6}{0.437 \times 0.022 \times 0.5 \cdot 10^{12}} \tag{7.1}$$

where N_{bkg} is the number of events in the background sample, α_{bkg} is the acceptance, ϵ_{bkg}^{tot} is the total efficiency estimated from simulation for the background sample and σ is the $b\bar{b}$ cross section in fb.

(PID). The larger $B \rightarrow hh$ contribution is given by the $B_s \rightarrow K^+K^-$ decay. With a muon/hadron mis-identification rate of 1%, $B_{s,d} \rightarrow hh$ backgrounds are small in comparison to the contribution of the inclusive di-muon background (see also [80]) and will not be included in this study. When the mis-ID rate has been properly calibrated, these backgrounds can be subtracted.

Mode	$Br \times 10^6$	Yield ($2fb^{-1}$)
$B_s \rightarrow K^+K^-$	25.8 ± 4.2	71.9 × 10^3 events
$B_s \rightarrow \pi^+K^-$	5.27 ± 1.17	15.1 × 10^3 events
$B_s \rightarrow \pi^+\pi^-$	≤ 1.7 CL=90%	67 (SM) events
$B_d \rightarrow \pi^+K^-$	19.4 ± 0.6	216.6 × 10^3 events
$B_d \rightarrow \pi^+\pi^-$	5.16 ± 0.22	58.8 × 10^3 events
$B_d \rightarrow K^+K^-$	≤ 0.4 CL=90%	114 (SM) events
$B_s \rightarrow \mu\mu$	≤ 0.15 CL=95%	30 (SM) events

Table 7.1: *$B \rightarrow hh$ branching ratios corresponding to the knowledge at the time of these studies, and annual yields for selected events [76]. The yield for $B_s \rightarrow \pi^+\pi^-$, $B_d \rightarrow K^+K^-$ and $B_s \rightarrow \mu\mu$ is calculated using the branching ratio predicted by the SM, in the second column their experimental exclusion limit is given [7].*

7.3 Observables for selection

The lifetime of the B_s is $\tau = 1.47 \pm 0.03\ ps$ ($c\tau = 441\ \mu m$) [7]. Since the B_s particles are boosted, they fly about one cm from the primary vertex (PV) before decaying. The secondary vertex (SV) is therefore detached as shown in Fig. 7.2(a). Combinatorial background from prompt muons is rejected using this secondary vertex signature, by requiring large muon impact parameter (IP) and large decay length of the B (DL). Combinatorial background from double semileptonic decays (see Fig. 7.2(b)) have large impact parameter of the B candidate and are rejected by requiring a good vertex and small IP of the B_s candidate with the primary vertex.

7.3.1 Preselection cuts

For technical reasons, the selection of events is performed in two steps. To reduce the data sample to a size that is suitable for analysis, a so-called *preselection* is applied. The B_s candidate is asked to form a vertex with a $\chi^2 < 14$, have an impact parameter significance smaller than 6 and an invariant mass within $\pm 600\ MeV$ of the B_s mass. The z-position of the SV is required to be downstream with respect to the reconstructed PV. The signal preselection efficiency is (80.8 ± 0.6)% (not including acceptance). The number of pre-selected di-muon inclusive background events in

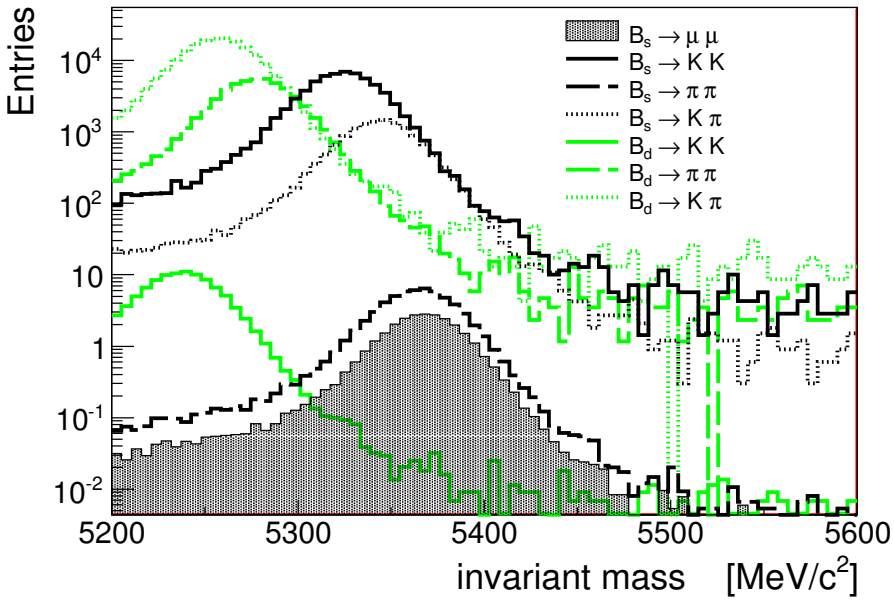

(a) No PID applied

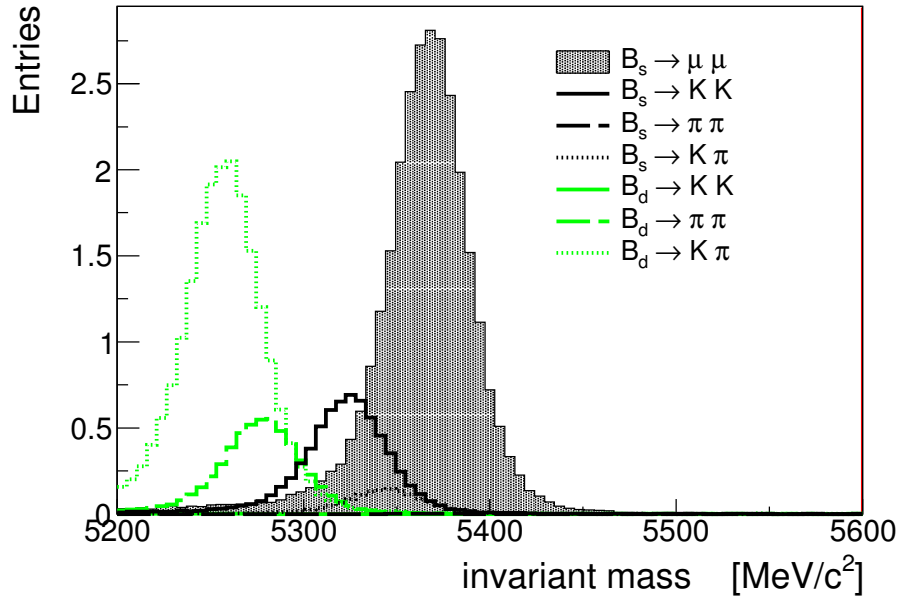

(b) PID applied

Figure 7.1: *Invariant mass distributions of $B_{d,s} \to h^+h^-$ and $B_s \to \mu^+\mu^-$. (a) No PID cut applied. (b) Assuming a 1% mis-id for the hadrons and 100% efficiency for the muons.*

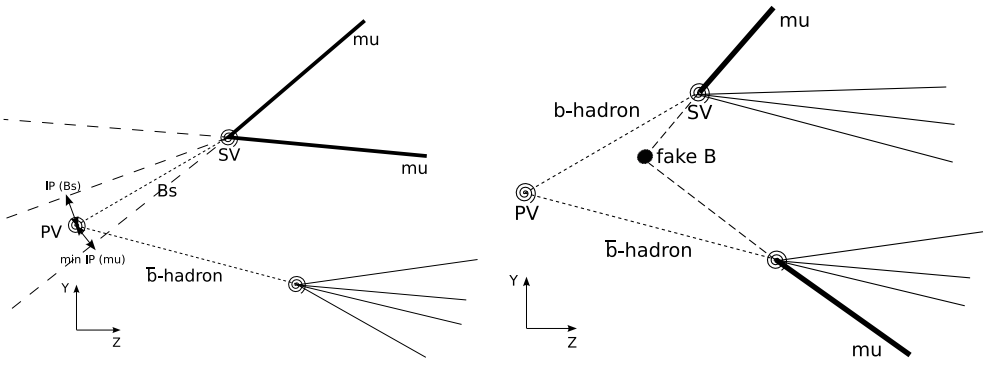

(a) Signal decay (b) $B \rightarrow \mu X; B \rightarrow \mu Y$

Figure 7.2: (*a*) *Signal decay topology.* (*b*) *Background from semileptonic B-decays.*

the acceptance is 42817, which corresponds to about 17M preselected background events per $2fb^{-1}$.

7.3.2 Selection cuts

The final selection cuts are optimized by applying a cut on the decay length significance of the B_s (DLS), a cut on the minimum IP significance of the final state muons (MIPS) and a cut on the invariant mass. The use of the DLS and MIPS instead of the DL and IP accounts for the uncertainties returned by the reconstruction and improves the background suppression.

Refit of the PV

The choice of the PV with respect to which the MIPS and DLS are calculated may be ambiguous. At a luminosity of $2{\times}10^{32}\mathrm{cm}^{-2}\mathrm{s}^{-1}$, the number of primary interactions per events is Poisson distributed with an average of 1 interaction per event as shown in Fig. 3.3. Therefore, about one third of the events contain more than 1 reconstructed interaction. The MIPS of the muons and the DLS of the B are calculated to the PV closest to the SV (the one with the smallest IP). Moreover, since the primary vertex finding collects all tracks with a χ^2 contribution to the vertex smaller than 16, the PV position is biased when a muon track from the $B_s \rightarrow \mu^+\mu^-$ candidates is included due to a systematic reduction of the distance between the PV and the SV. Consequently, the PV is refitted excluding the final state muon tracks when necessary.

Distributions

The distribution of the muon MIPS for preselected signal events (thick line) and for preselected background events (grey area), before and after the PV refit, are shown in Figs. 7.3(a) and 7.3(b). For the MIPS the vertex bias shows up as a dip at MIPS ≈4, which disappears after refitting. The distribution of the MIPS for signal events has a long tail while background events shows a peak at low value. The distributions of the DLS for signal (thick line) and for inclusive di-muon background events (grey area) are shown in Fig. 7.3(c) after PV refitting. The background events fall mostly within the first bins of the distribution, while signal events spans over a wider range.
A cut on the B_s invariant mass of $\pm 60\ MeV$ is applied to reduce the combinatorial background due to fake candidates and to reduce the $B_d \to hh$ background. The invariant mass distributions for signal (thick line) and for inclusive di-muon background events (grey area) are shown in Fig. 7.3(d). The mass peak has a radiative tail on the left due to (QED) emission of soft photons. The background follows a linearly decreasing distribution.

Selection efficiencies

In Tab. 7.2 the numbers of events surviving after preselection and each selection criterion are shown. The efficiencies over the preselected events, calculated independently for each cut, are reported in Tab. 7.3. The total selection efficiency is (52.5 ± 0.6)% for the signal and $(7.51 \pm 0.5) \times 10^{-4}$% for the background.

	Signal	**Background**
Generated	71200	26.3M (0.005 fb^{-1})
Preselected	57544	42817
$MIPS \geq 3.5$	45378	6491
$DLS \geq 12$	40915	1998
Δm ($\pm 60\ MeV$)	37408	197

Table 7.2: *Number of surviving signal and background events after each cut. From the top: generated events in acceptance, preselected events and surviving events after each selection cuts applied in sequence.*

Limited statistics of the background sample

Only 197 background events are selected and those are insufficient for the further steps in this MC study. To increase the amount of background, the $\pm 60\ MeV$ cut on the mass is not applied on background events. Since the background follow a

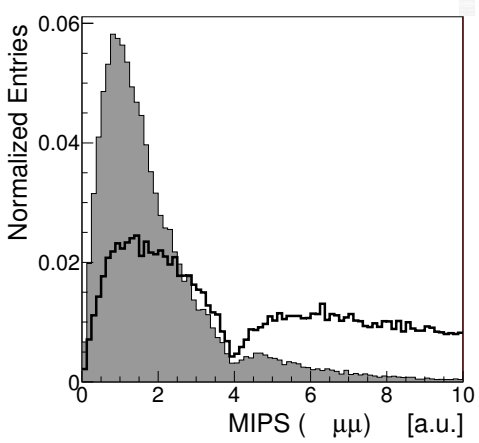

(a) Biased muon MIPS

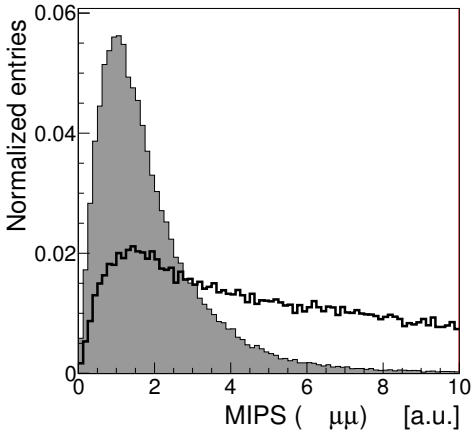

(b) Muons MIPS after PV refit

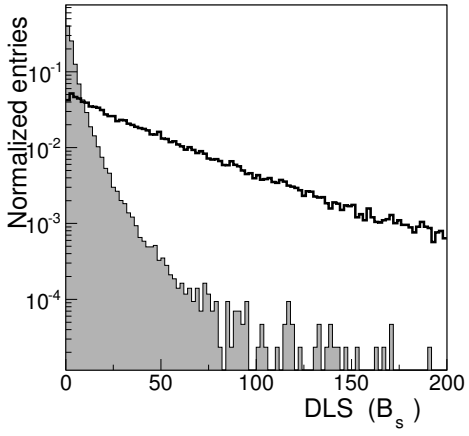

(c) DLS

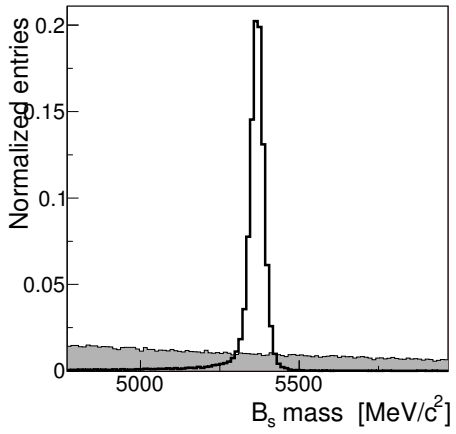

(d) Invariant mass

Figure 7.3: *Normalized distributions of the variables used in the selection for signal events (thick line) and preselected inclusive di-muon background events (grey area). Bias minimum impact parameter significance of the final state muons before (a) and after (b) refitting of the primary vertex (see text). (c) Decay length significance of the B_s. (d) B_s Invariant mass.*

sel/presel	**Signal**	**Background**
$MIPS \geq 3.5$	78.9 ± 0.6 %	15.2 ± 1.3%
$DLS \geq 12$	74.1 ± 0.6%	8.1 ± 2.2 %
Δm ($\pm 60\ MeV$)	90.6 ± 0.6%	9.8 ± 7.1%
All	**65.0 ± 0.6** %	**0.5 ± 2** %

Table 7.3: *Selection cuts efficiency over preselected events applied independently for each cut for signal and background.*

linearly decreasing distributions in the full preselected mass range ($\pm 600\ MeV$), the luminosity of the background sample is consequently rescaled by a factor ten, to an equivalent luminosity of 0.05 fb^{-1}.

7.4 Observables for likelihood

The maximum likelihood method consists of building a model using Probability Density Functions (PDF) corresponding to a set of input variables, in order to classify an event as signal or background. The likelihood of being signal (background), is obtained by multiplying the signal (background) PDFs of all input variables fitted on MC data by means of kernel density estimators [85]:

$$\mathcal{L}_{S(B)}(i) = \prod_{k=1}^{n_{var}} p_{S(B),k}(x_k(i)) \tag{7.2}$$

where $p_{S(B),k}$ is the normalized signal (background) PDF for the kth input variable x_k. The likelihood ratio $y_{\mathcal{L}}(i)$, for the event i, is defined by:

$$y_{\mathcal{L}}(i) = \frac{\mathcal{L}_S(i)}{\mathcal{L}_S(i) + \mathcal{L}_B(i)}. \tag{7.3}$$

As already said in the introduction to this chapter, three observables are used to classify the selected events as signal and background. Those variables are the invariant mass and two likelihood ratios (GL and MIL). The GL and MIL are designed to be independent and not correlated with the invariant mass. To achieve this independence the momenta of the muons are not used in the selection. This reduces the statistical power of rejecting background, but at the same time, this choice limits the systematic uncertainties to be handled in the calibration of the observables with control channels.

7.4.1 Geometry Likelihood (GL)

The GL assigns a probability that the geometrical characteristics of the event are signal or background like. The GL is built from the variables described below.

B_s lifetime and the χ^2 of the lifetime fit

The so-called χ^2 of the lifetime fit quantifies how well the reconstructed B fits the primary vertex. It is the χ^2 of a vertex fit in which the B candidate is constrained to originate from the PV, using the following model:

$$\vec{x}_B - \vec{x}_{PV} = \frac{\vec{p}}{|\vec{p}|} \times L = \frac{\tau}{m}\vec{p}, \tag{7.4}$$

where L is the decay length, $\vec{x}_B$ the reconstructed B vertex, $\vec{p}$ is the B momentum and $\vec{x}_{PV}$ is the PV position. The input are the measured $(\vec{x}_B, \vec{p})$ with covariance and $\vec{x}_{PV}$ with covariance. The output are the decay length L (or the eigentime τ) and new values for $\vec{x}_B$, $\vec{p}$ and $\vec{x}_{PV}$. The χ^2 distribution for signal and background is shown in Fig. 7.4(b). The discriminating power of the lifetime is similar to the flight distance but it is less momentum dependent because of the following: the decay length uncertainty correlates with momentum given the opening angle; the higher the momentum the larger the uncertainty. Since the uncertainty is approximately proportional to the momentum, the uncertainty on the lifetime is therefore almost constant. The lifetime distribution for signal and background is shown on Fig. 7.4(a) for preselected events. Signal events are distributed as an exponential, while most background events are constrained to a narrow region around zero.

Distance Of Closest Approach between the two muons (DOCA)

The DOCA is the distance between the two muon tracks. Since signal muons originate from a single vertex, the DOCA is approximately zero for signal. In the case of background, two arbitrary muon candidates are combined into a vertex and the DOCA can be larger. The DOCA distributions for signal and background events is shown in Fig. 7.4(c). The background distribution spans over a range of few hundreds microns, while most of the signal events fall within the first 50 microns.

Asymmetry of the muon momenta

The muon momenta asymmetry is defined as:

$$Asym = \frac{|p_- - p_+|}{|p_- + p_+|}, \tag{7.5}$$

where p_- and p_+ are the momentum of the μ^- and μ^+ respectively. The background often consists of combinations of a high and a low momentum muons, consequently the distribution has a peak at one as shown in Fig. 7.4(d). In the signal the momenta of the muons are correlated via the B_s-momentum. The observed shape of the signal distribution in Fig. 7.4(d) is due to the cutoff in momentum for the muon system.

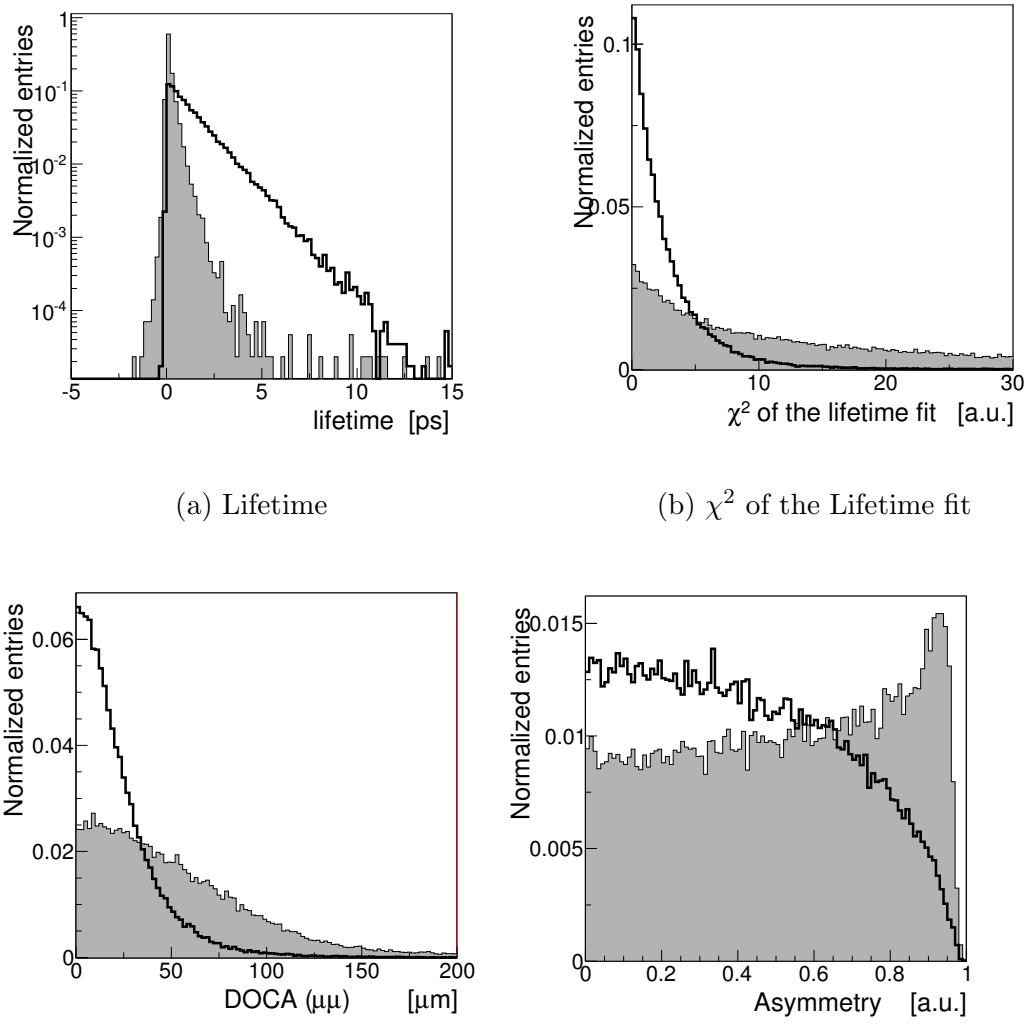

(a) Lifetime

(b) χ^2 of the Lifetime fit

(c) DOCA

(d) Asymmetry

Figure 7.4: *Normalized distributions of the variables used in the geometrical likelihood for signal events (thick line) and preselected background events (grey area). (a) B_s lifetime. (b) χ^2 of the lifetime fit. (c) Distance of closest approach between the two muon candidates. (d) Momentum asymmetry between final state muons.*

GL distribution

The distribution of the likelihood ratio formed with the observables above, peaks at zero for background and at one for signal. For convenience in the following analysis steps, the shape of the distributions are transformed such that the likelihood of the signal is flat and distributed in the range between 0 to 1. The distribution of the GL for the selected 37408 signal and 1998 background events is shown in Fig. 7.5(a), at high value of GL the background distribution is depleted.
The correlation between GL and momentum (required to be small to simplify the calibration procedure with first data) is studied versus the p_t of the B_s and the μ^+. The 2D distributions for the signal sample are sliced in 20 bins in p_t and the mean of each slice is shown in Figs. 7.5(b) and 7.5(c). A small dependence of the GL is noticeable for very low p_t muons, presumably due to the poor DL estimation as consequence a the worse extrapolation to the vertex region for these low p_t tracks.

7.4.2 Muon Identification Likelihood (MIL)

The PID likelihood is based on information from the muon chambers, the calorimeters and the RICH detectors to assign a global likelihood $\mathcal{L}$ for each mass hypothesis [86] (i.e. $\mathcal{L}_\mu$, $\mathcal{L}_k$, $\mathcal{L}_\pi$ for μ, kaon and π hypothesis, respectively). The Muon Identification Likelihood assigns a probability of a candidate to be a muon and is given by a likelihood ratio of these two likelihood differences

$$\Delta L_{\mu\pi} = \mathcal{L}_\mu - \mathcal{L}_\pi; \qquad \Delta L_{\mu k} = \mathcal{L}_\mu - \mathcal{L}_k. \tag{7.6}$$

The MIL is important for the rejection of minimum bias events and $B \rightarrow hh$ backgrounds but it will not used in the rest of this MC study, since in the inclusive di-muon background sample there are always two muons in the final state.

7.5 Sensitive region

Since the MIL is not used, the sensitive region is determined for GL and invariant mass only. The mass window width of $\pm 60\ MeV$ around the B_s mass is here optimized. To define the significance level a commonly used function is

$$SL = \frac{S}{\sqrt{S+B}}, \tag{7.7}$$

where S and B are the number of selected events for signal and background in 2 fb^{-1} (and primary interactions corresponding to the nominal instantaneous LHC luminosity of $2{\times}10^{32}\mathrm{cm}^{-2}\mathrm{s}^{-1}$). The optimization based on the equation above becomes not ideal for small number of background events, as it would be at high value of

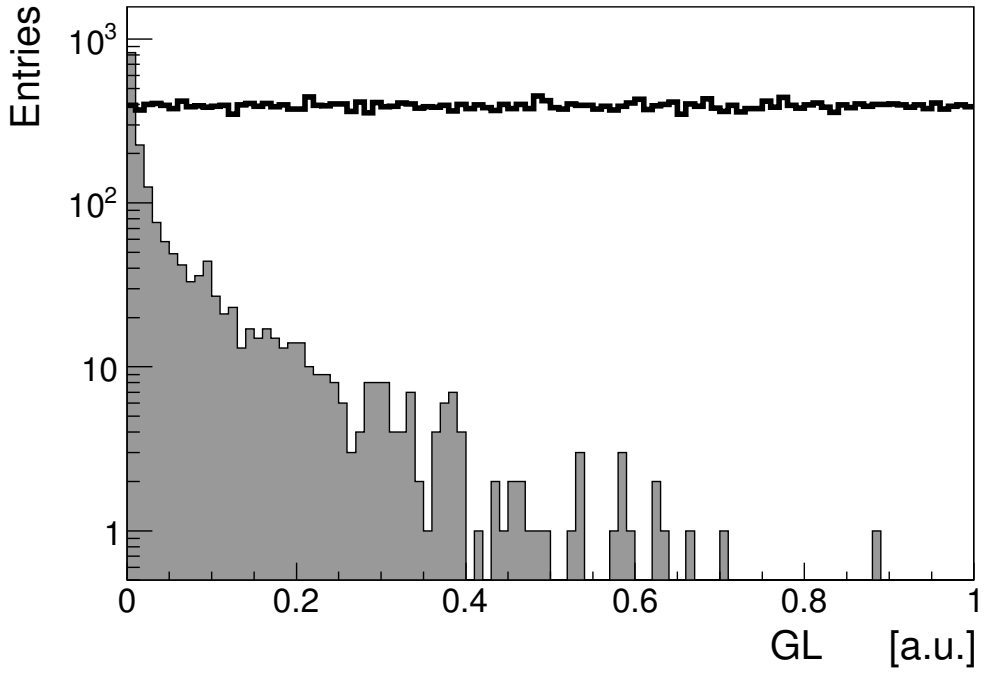

(a) GL distribution

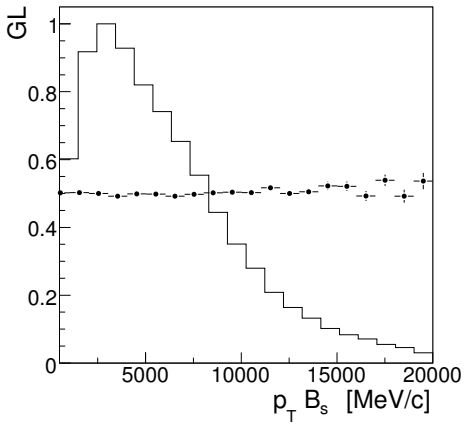

(b) GL correlation with B_s p_T

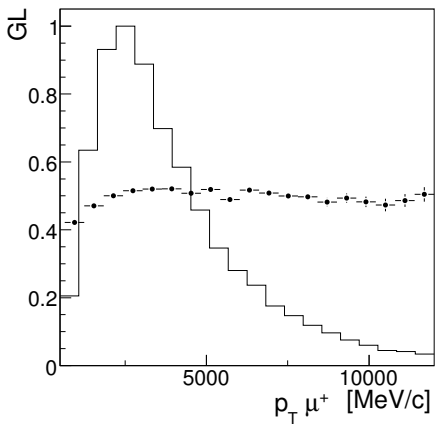

(c) GL correlation with μ^+ p_T

Figure 7.5: (*a*) *Distribution of the GL calculated for selected signal events (thick line) and selected background (grey area). Lower panel: Geometrical likelihood calculated for selected signal events and its correlation with the transverse momentum of the* B_s (*b*) *and the final state* μ^+ (*c*). *The* p_t *distributions on arbitrary scale are superimposed.*

GL, and it depends on the signal branching ratio. A convenient definition for the significance level was proposed by Punzi [87], here adopted as:

$$SL = \frac{S}{1.5 + \sqrt{B}}. \tag{7.8}$$

The SL is determined for the invariant mass for increasing mass windows. As illustrated in Fig. 7.8(c) the SL reaches a maximum at about 20-24 MeV, the optimal cut is therefore set to $\pm 25\ MeV$ which is about 1.5 times the invariant mass resolution.
The SL is then determined as function of an increasing cut on the GL. As illustrated in Fig. 7.6(b) it has a clear peak and the optimal cuts is set at GL>0.6.
Out of the full available MC signal sample, 11229 signal events fall into the sensitive

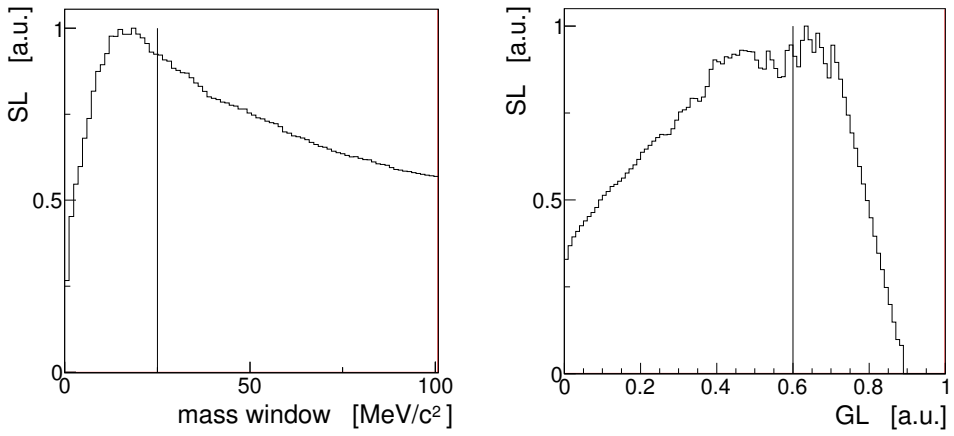

(a) mass cut Significance Level (b) GL cut Significance Level

Figure 7.6: *Significance level of $B_s \rightarrow \mu^+\mu^-$ versus a cut centered around the B_s invariant mass (a) and an increasing cut on the GL (b). The continuous line indicate the optimal cut: $\pm 25\ MeV$ in mass and GL > 0.6.*

region, namely $30.0 \pm 3.6\%$ of the selected signal. Assuming the SM branching ratio this corresponds to 22 for a luminosity of 2 fb^{-1}. For background, the selection cut on the mass is not applied, and out of the full available MC sample of 0.005 fb^{-1}, six background events ($N^{GL>0.6}_{B/0.005fb^{-1}}$=6) are in the region of GL>0.6. In 2 fb^{-1} the expected number of background events in the sensitive region and its uncertainty are therefore:

$$N^{SR}_{B/2fb^{-1}} = N^{GL>0.6}_{B/0.005fb^{-1}} \times 25/600 \times 2/0.005 = 100 \tag{7.9}$$

$$\sigma_{N^{SR}_{B/2fb^{-1}}} = \sqrt{N^{GL>0.6}_{B/0.005fb^{-1}}} \times 25/600 \times 2/0.005 = 41. \tag{7.10}$$

where 25/600 is the ratio of the mass windows (see Sec. 7.3.1) and 2/0.005 is the luminosity scaling factor.

7.6 Exclusion limit with a frequentist profile likelihood method

The purpose of this section is to set a constraint on the $B_s \to \mu^+\mu^-$ branching ratio by estimating the 90%CL exclusion limit, corresponding to an integrated luminosity of 2 fb^{-1}. The exclusion limit can be interpreted as follows: *The $B_s \to \mu^+\mu^-$ branching ratio is not larger than a certain value at a 90% Confidence Level (CL).* The limit calculations make use of the *profile likelihood method* [1] [88] and require as input the estimate of the expected number of background events in 2 fb^{-1} falling in the sensitive region, the number of actual "measured" events in the sensitive region and the uncertainty on the background. Since data are not available the "measured" number of events is given by a set of 10^7 random numbers generated according to a Poisson distribution around $N^{SR}_{B/2fb^{-1}}$. Each of those numbers corresponds to a so called "pseudo-experiment", a possible result of the LHCb experiment. Assuming that only background is measured (null hypothesis) an estimation of the average number of "signal events" is extracted and a corresponding exclusion limit for the required CL of 90% is calculated. The distribution of exclusion limits of the 10^7 pseudo-experiments is shown in Fig. 7.8(a). The sub-range (light grey) corresponds to the interval covering from 16% to 84% of the peak area. The vertical continuous line indicates the median of the distribution. From the median and the interval, the following estimation of the average value of the exclusion limit and its statistical uncertainty is determined:

$$Br^{90\%CL}(B_s \to \mu^+\mu^-) = (1.86 \ \pm \ 0.84) \ \times \ 10^{-9}. \tag{7.11}$$

However, in this MC study the estimate of the background is very poor. Therefore the prediction of the expected upper limit obtained above, has a larger uncertainty due to the error in the six background events measured in the the sensitive region ($N^{GL>0.6}_{B/0.005fb^{-1}}$). To fold the uncertainty on the average number of the expected background events, a first set of 10^3 random numbers according to the function in Fig. 7.7 (representing the spread of $N^{GL>0.6}_{B/0.05fb^{-1}}$) is generated and then multiplied by $25/600 \times 2/0.005$ as in Eq. 7.9. For each number in the first set, 10^4 random numbers are generated according with a Poisson distribution centered in it. In total 10^7 pseudo-experiments are generated and the corresponding distribution of the exclusion is shown in Fig. 7.8(b). Its sub-range (dark grey) correspond to the interval covering from 16% to 84% of the peak area. The wider range of this second distribution is used to quote the uncertainty on the exclusion limit estimate. The potential of LHCb of excluding the $B_s \to \mu^+\mu^-$ branching ratio at 90% in 2 fb^{-1}, accounting for the error due to the limited background statistic available for this MC study, is therefore

$$Br^{90\%CL}(B_s \to \mu^+\mu^-) = (1.86^{+1.2}_{-0.84}) \ \times \ 10^{-9}. \tag{7.12}$$

[1] Using the TRolke class implemented in the ROOT framework [89].

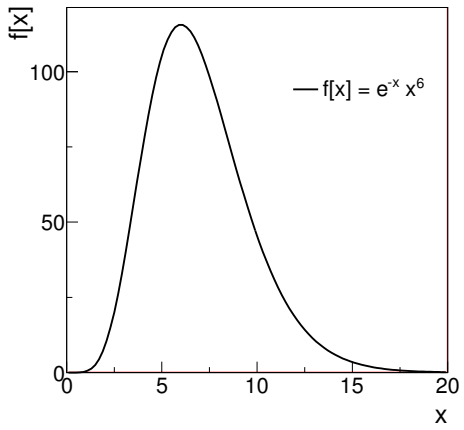

Figure 7.7: *Functions in arbitrary scale, used to smear* $N^{GL>0.6}_{B/0.005fb^{-1}}$ *(see text).*

After LHCb has taken data, sideband data can be used to estimate the background more precisely than with the limited MC statistics available for this study, and the "background" uncertainty quoted here will not be relevant.
Since the confidence level[2] of Eq. 7.12 scales as the inverse of the square root of the integrated luminosity, the 90%CL exclusion limit can be extrapolated along the first year of data taking as shown in Fig. 7.8(c). The dark grey band corresponds to the interval in Fig. 7.8(b). The dotted horizontal line corresponds to the SM prediction, which can be excluded at 90%CL with about 1 fb^{-1} (half nominal year of data). Sources of systematic uncertainties will be discussed in Sec. 7.9.

The profile likelihood method is also used to estimate how much luminosity is needed to reach a 3σ evidence or 5σ discovery with respect to the SM prediction. The sensitivity is extrapolated up to 10 fb^{-1}, corresponding to five years of nominal data (see Figs. 7.9(a) and 7.9(b)). Regarding the SM $Br(B_s \rightarrow \mu^+\mu^-)$, the 3 σ evidence and 5 σ discovery can be achieved with approximately 4 and 10 fb^{-1} of data respectively.

7.7 Exclusion limit with a non-frequentist binned likelihood method

For a comparison with the result in [80, 90], in this section a binned likelihood method developed for the Higgs search at LEP [91, 92] is used to calculate the $Br^{90\%CL}(B_s \rightarrow \mu^+\mu^-)$. In this specific application, a method is applied making use of 2D histogram (GL versus invariant mass) with four bins in the GL ranging between 0 to 1 and three bins in the invariant mass ranging in ± 60 MeV. This

[2]Optimized for 2 fb^{-1} of integrated luminosity.

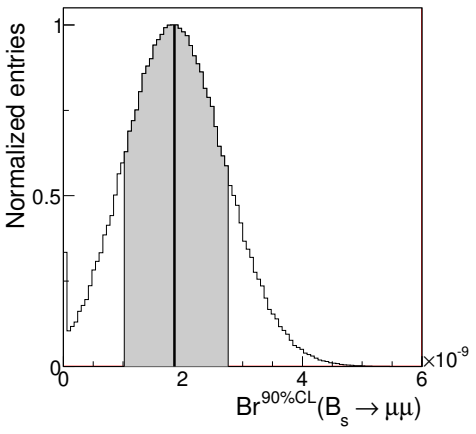

(a) Neglecting MC uncertainty

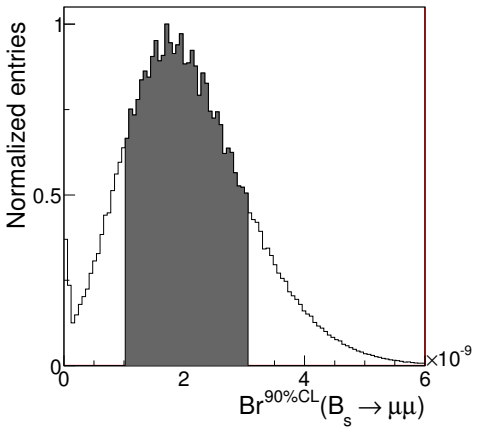

(b) Folding MC uncertainty

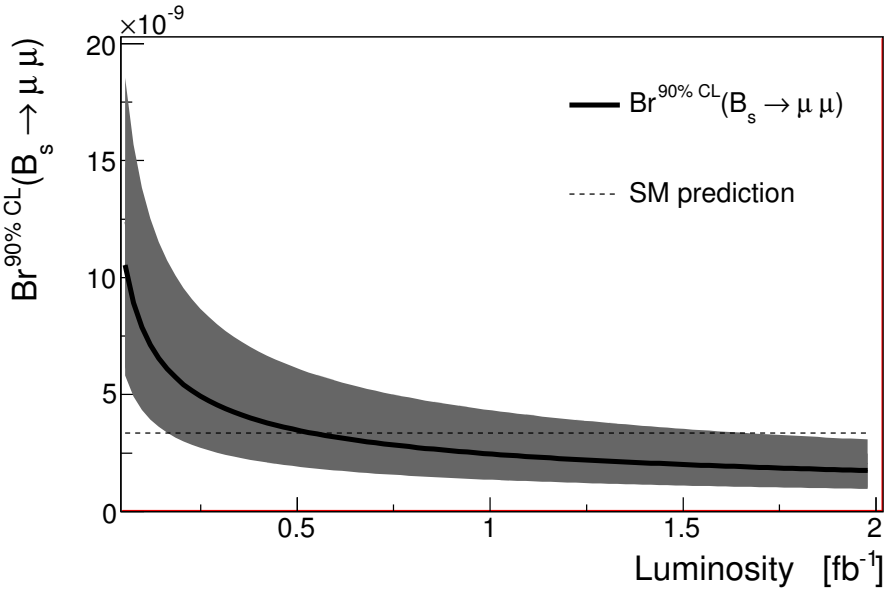

(c) $Br^{90\%CL}(B_s \to \mu^+\mu^-)$ vs luminosity

Figure 7.8: *Distribution of the 90% exclusion limit for* 10^7 *pseudo-experiments neglecting* (*a*) *and including* (*b*) *the uncertainty on the expected average number of background events in the sensitive region.* (*c*) *Estimate of the 90% exclusion limit as function of the integrated luminosity along the first year of data. The error band folds in the uncertainty due to the limited MC statistics. The horizontal dotted line indicates the SM prediction.*

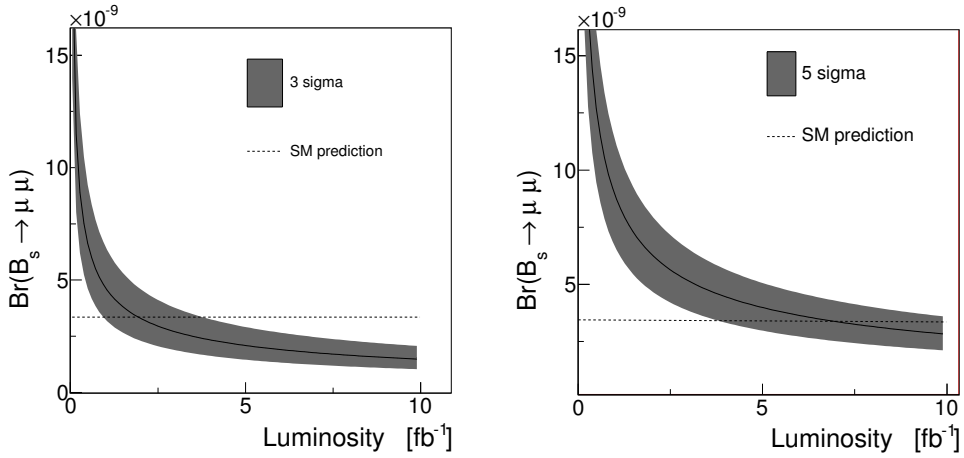

(a) 3 σ significance vs luminosity (b) 5 σ significance vs luminosity

Figure 7.9: *Estimate of the 3 sigma evidence (a) and 5 sigma discovery (b) as function of the integrated luminosity along the first 5 nominal years of data (10 fb^{-1}). The error band folds in the uncertainty due to the limited MC statistics. The thin continuous line indicated the median. The horizontal dotted line indicate the SM prediction.*

method takes care of uncertainties associated in each bin content. Since no cuts in mass or GL are applied, all the selected signal and background are used. In a null hypothesis the upper limit at 90% for the $B_s \rightarrow \mu^+\mu^-$ branching ratio is calculated to be:

$$Br^{90\%CL}(B_s \rightarrow \mu^+\mu^-) = (1.79 \pm 0.57) \times 10^{-9}. \tag{7.13}$$

The quoted statistical uncertainty is returned by the method and it does not take the MC uncertainty into account. An accurate estimation of the systematic uncertainty due to the limited MC sample, has not been pursued due to CPU time (each scenario requires about 1 day of CPU). The results in Eq. 7.12 and Eq. 7.13 are compatible.

7.8 Branching ratio extraction

The total number of produced B-mesons (N_b) is given by the $b\bar{b}$ cross section (500 μb) multiplied by the integrated luminosity. The number of signal events observed ($N_{(\mu\mu)}$) in the experiment is given by

$$N_{(\mu\mu)} = 2\ N_b \times f_s \times Br_{(\mu\mu)} \times \epsilon^{tot} \tag{7.14}$$

where f_s is the fragmentation fraction for a B-hadron to fragment into B_s, $Br_{(\mu\mu)}$ is the signal branching ratio and ϵ^{tot} is the total efficiency due to acceptance, reconstruction, selection and trigger. Since the luminosity (and therefore N_b) cannot

be determined with high precision and in order to reduce the sensitivity to the uncertainty in the efficiency, the branching fraction is measured by using a reference decay, namely $B^+ \to J/\psi(\mu\mu)K^+$. The measurement of the branching ratio can then be written as:

$$Br_{(\mu\mu)} = \frac{N_{(\mu\mu)}}{N_{(J/\psi K^+)}} \times \frac{f_u}{f_s} \times Br_{(J/\psi K^+)} \times \frac{\epsilon^{tot}_{(J/\psi K^+)}}{\epsilon^{tot}_{(\mu\mu)}}, \tag{7.15}$$

where $N_{(J/\psi K^+)}$ is the number of observed $B^+ \to J/\psi(\mu^+\mu^-)K^+$ events, f_u is the fraction for a B-hadrons to fragment into B_u, $Br_{(J/\psi K^+)}$ is the $B^+ \to J/\psi(\mu^+\mu^-)K^+$ branching ratio and $\epsilon^{tot}_{(J/\psi K^+)}$ its total efficiency. The main source of systematic uncertainty is due to the ratio of the fragmentation factors (see Sec. 7.9.1).

A second significant source of systematic uncertainty comes from the ratio of the efficiencies due to the extra K^+ which reduce the acceptance of $B^+ \to J/\psi(\mu^+\mu^-)K^+$ and differences in phase space (and therefore in the track reconstruction efficiency) between the muons in the final state of $B_s \to \mu^+\mu^-$ and $B^+ \to J/\psi(\mu^+\mu^-)K^+$ (see Sec. 7.9.2). The ratio of the efficiencies is computed using simulated data. In order to analyze the uncertainty in the efficiency ratio, the efficiency is schematically factorized as follows:

$$\epsilon^{tot} = \epsilon^{acc} \times \epsilon^{rec}_{acc} \times \epsilon^{sel}_{rec} \times \epsilon^{trigger}_{sel}. \tag{7.16}$$

The first two terms are discussed below, the ϵ^{sel}_{rec} is discussed in Sec. 7.8.1 for the control channels. In the following only the L0 trigger is applied.

ϵ^{acc} (Detector acceptance)

The acceptance is defined by a set of cuts that are applied at generator level in the LHCb MC simulation. The generated B-mesons must have a polar angle smaller than 400 $mrad$. Furthermore, all of its stable daughter particles (the two muons in the case of $B_s \to \mu^+\mu^-$ and the two muons and kaon for $B^+ \to J/\psi(\mu^+\mu^-)K^+$) must have a polar angle in the range 10-400 $mrad$. The angular acceptance is conservatively chosen larger than the actual detector acceptance, in order to prevent possible detection of particles that are generated outside the nominal angular region. The ratio of the acceptance for $B_s \to \mu^+\mu^-$ and $B^+ \to J/\psi(\mu^+\mu^-)K^+$ can only be extracted from MC and is shown on Tab. 7.5. Since the relative production ratio of B_s and B_u must be folded in, only the production ratio *in the acceptance* is relevant. In this analysis the acceptances will fully rely on the MC model.

ϵ^{rec}_{acc} (Reconstruction efficiency)

The reconstruction efficiency for a given decay is measured as the fraction of the number of events with the proper number of reconstructed long tracks (with assigned PID) and coming from the same vertex, over the number of events generated

within the detector acceptance. With the acceptance defined as above, the efficiency to reconstruct events in the acceptance is not unity, because the acceptance is chosen larger than the detector. In addition, the charged particles may traverse insufficient detector layers to be found by the track finding algorithms. In particular, the magnetic field introduces a cut-off for low momenta. Consequently, the reconstruction efficiency ϵ_{acc}^{rec} is strongly momentum dependent. The momentum spectrum of the B-decays produced in LHCb has a considerable uncertainty. Therefore, until the spectrum has been properly calibrated, it will introduce an appreciable systematic uncertainty when estimating efficiencies from the simulation.
Moreover, the reconstruction of track depends on the efficiency of the pattern recognition algorithm, which is based on the realistic hardware layer efficiency, and the actual resolution of the sub detectors. Track finding algorithms are also sensitive to occupancy (therefore, the reconstruction efficiency ϵ_{acc}^{rec} depends on the occupancy). It is not guaranteed that the existing MC simulation estimates the occupancy reliably. Consequently, until the MC is well tuned, there is also a systematic uncertainty due to the difference in detector occupancy.
To first order some of these uncertainties cancel in the ratio of efficiencies for $B_s \rightarrow \mu^+\mu^-$ and $B^+ \rightarrow J/\psi(\mu^+\mu^-)K^+$. Two approaches to evaluate this ratio are considered:

- **Using only MC**
  The limitations in the MC are mainly due to uncertainty in hit detection efficiency, wrong estimation of charge multiplicities, a bias in the B momentum spectrum, approximation in the material budget description and absence of further sources of environmental background like scattering and gas beam interactions. Once data will be available, the MC can be tuned and the efficiency ratio can be determined solely from the simulation. Moreover using the control channel, the simulation is either tuned or reweighed to properly represent the distributions to which the ratio is most sensitive, namely the momentum spectrum of the B and the occupancy of the event. Remaining differences between data and simulation are used to assign a systematic uncertainty.

- **Using the $B^0 \rightarrow J/\psi(\mu^+\mu^-)K^{*0}(K\pi)$ control sample**
  The sensitivity to errors in the efficiency estimate on MC can also be reduced by considering an additional ratio of control channels in order to probe explicitly the efficiency for reconstructing an extra track in the final state. A suitable control channel is $B^0 \rightarrow J/\psi(\mu^+\mu^-)K^{*0}(K\pi)$ with $K^{*0} \rightarrow K^+\pi^-$. If the probability for a track to be reconstructed is independent of the momentum of the track, one may expect that to first order

$$\frac{\epsilon_{acc(\mu\mu)}^{rec}}{\epsilon_{acc(J/\psi K^+)}^{rec}} \approx \frac{\epsilon_{acc(J/\psi K^+)}^{rec}}{\epsilon_{acc(J/\psi K^*)}^{rec}}, \tag{7.17}$$

  where the labels $(J/\psi K^+)$ and $(J/\psi K^*)$ are used to indicate $B^+ \rightarrow J/\psi(\mu^+\mu^-)K^+$

and $B^0 \to J/\psi(\mu^+\mu^-)K^{*0}(K\pi)$ respectively. In Fig. 7.10(a) the reconstruction efficiency is shown as function of the momentum of the B mesons for $B_s \to \mu^+\mu^-$, $B^+ \to J/\psi(\mu^+\mu^-)K^+$ and $B^0 \to J/\psi(\mu^+\mu^-)K^{*0}(K\pi)$. Each extra track to be reconstructed leads to a loss in the event reconstruction efficiency. In Fig. 7.10(b) the reconstruction efficiency ratios between $B^+ \to J/\psi(\mu^+\mu^-)K^+$ over $B_s \to \mu^+\mu^-$ (open dots) and $B^0 \to J/\psi(\mu^+\mu^-)K^{*0}(K\pi)$ over $B^+ \to J/\psi(\mu^+\mu^-)K^+$ (full dots) is shown as a function of the B momentum. The two profiles overlap over all the momentum spectrum. The grey area indicates the ratio of the efficiency ratios (double ratio) which is close to one in the full B_s momentum spectra. Given the number of observed events $N_{(J/\psi K^+)}$ and $N_{(J/\psi K^*)}$:

$$N_{(J/\psi K^+)} = N_b \times f_u \times Br_{(J/\psi K^+)} \times \epsilon^{tot}_{(J/\psi K^+)}, \tag{7.18}$$

$$N_{(J/\psi K^*)} = N_b \times f_d \times Br_{(J/\psi K^*)} \times \epsilon^{tot}_{(J/\psi K^*)}, \tag{7.19}$$

the $B_s \to \mu^+\mu^-$ branching ratio can be estimated from the observed $B_s \to \mu^+\mu^-$, $B^+ \to J/\psi(\mu^+\mu^-)K^+$ and $B^0 \to J/\psi(\mu^+\mu^-)K^{*0}(K\pi)$ events as follows

$$Br(B_s \to \mu^+\mu^-) \;=\; \frac{N_{(\mu\mu)}N_{(J/\psi K^*)}}{N^2_{(J/\psi K^+)}} \times \frac{f_u^2}{f_s f_d} \times \frac{Br^2_{(J/\psi K^+)}}{Br_{(J/\psi K^*)}} \times \frac{R1}{R2} \tag{7.20}$$

where:

$$R1 = \frac{\epsilon^{tot}_{(J/\psi K^+)}}{\epsilon^{tot}_{(\mu\mu)}}; \qquad R2 = \frac{\epsilon^{tot}_{(J/\psi K^*)}}{\epsilon^{tot}_{(J/\psi K^+)}} \tag{7.21}$$

7.8.1 Event selection of control channels

The selection for the control channels does not need to be optimized given the high event yield (see Tab. 7.4). However, if the selection efficiencies for signal and control channels are similar they cancel in R1, R2 and in the double ratio. Therefore the selection for both control channels is done similar to the signal selection described in Sec. 7.3.

The control channel decay topologies are shown in Fig. 7.11. Final state muons

Channel	**Branching ratio**	**Events** ($2fb^{-1}$)
$B^+ \to J/\psi(\mu^+\mu^-)K^+$	$(6.67 \pm 0.04) \times 10^{-5}$	1.9M
$B_s \to J/\psi(\mu^+\mu^-)K^{*0}(K\pi)$	$(8.81 \pm 0.08) \times 10^{-5}$	1.5M

Table 7.4: *Control channels branching ratio and event yield.*

come from the J/ψ. Therefore, the B_s vertex χ^2 cut is replaced with the χ^2 of the J/ψ. The mass cut is applied on the J/ψ mass peak. The impact parameter significance is calculated for the $B_{u|d}$. The detached SV is asked to be

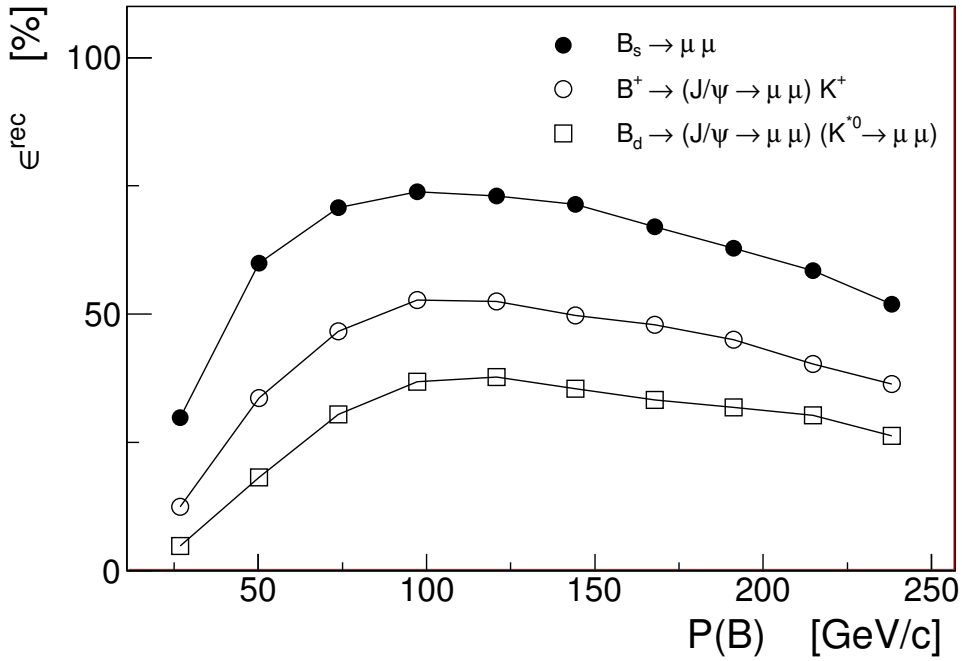

(a) ϵ^{rec} vs momentum.

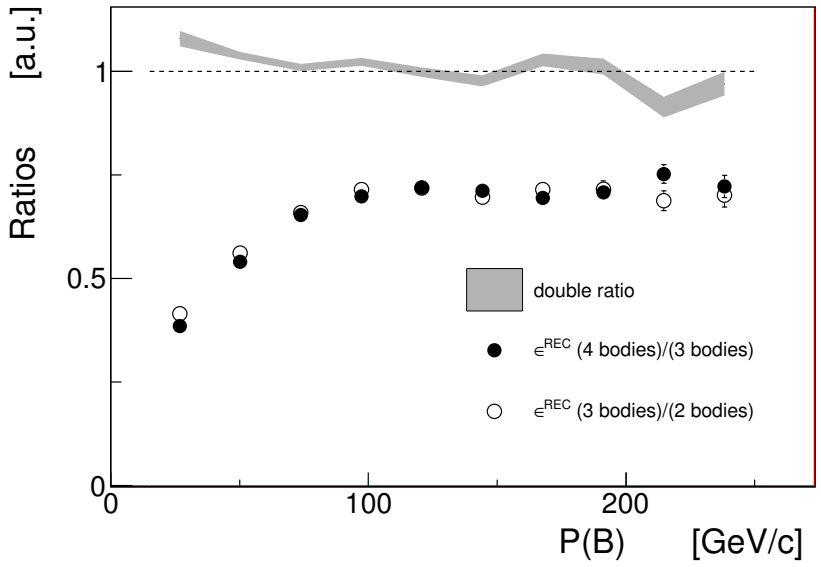

(b) Ratios of reconstruction efficiency vs momentum.

Figure 7.10: *(a) ϵ^{rec}_{acc} as function of the momentum of the B for signal and control channels. (b) The ratio of ϵ^{rec}_{acc} between $B_u \rightarrow J/\psi K^+$ and $B_s \rightarrow \mu^+\mu^-$ (open dots) and between $B^0 \rightarrow J/\psi(\mu^+\mu^-)K^{*0}(K\pi)$ and $B_u \rightarrow J/\psi K^+$ (full dots) is shown as function of the momentum of the B. The grey area indicates the ratio of the two.*

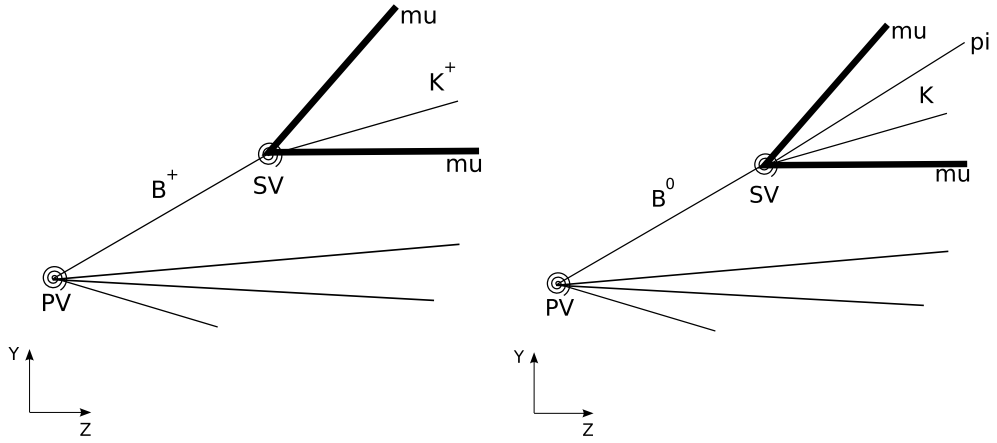

(a) $B^+ \to J/\psi(\mu^+\mu^-)K^+$ (b) $B^0 \to J/\psi(\mu^+\mu^-)K^{*0}(K\pi)$

Figure 7.11: *Control channels decay topology of* $B^+ \to J/\psi(\mu^+\mu^-)K^+$ *(a) and* $B^0 \to J/\psi(\mu^+\mu^-)K^{*0}(K\pi)$ *(b).*

downstream with respect to the PV. In summary, the preselection cuts for the control channels are: $\chi^2(J/\psi) < 14$, $IPS(B_{d/u}) < 6$ and mass$(J/\psi)\pm 600\ MeV$. The preselection efficiency are 95.53% and 95.15% for $B^+ \to J/\psi(\mu^+\mu^-)K^+$ and $B^0 \to J/\psi(\mu^+\mu^-)K^{*0}(K\pi)$ respectively.
The final selection cuts on the DLS(B_s) and MIPS($\mu\mu$) are replaced with the DLS($B_{u|d}$) and the IPS(K) respectively. The loose $\pm 60\ MeV$ mass cut is applied on the J/ψ mass. A breakdown of the efficiency for signal and control channels is given in Tab. 7.5.

	ϵ^{acc}	ϵ^{rec}_{acc}	ϵ^{sel}_{rec}	ϵ^{tot}
$B_s \to \mu\mu$	20.0 ± 0.20%	59.51 ± 0.19%	68.64 ± 0.15%	8.17 ± 0.10%
$B_u \to J/\psi(\mu\mu)K^+$	17.8 ± 0.20%	39.62 ± 0.22%	67.35 ± 0.16%	4.75 ± 0.10%
$B_d \to J/\psi(\mu\mu)K^*(K\pi)$	17.3 ± 0.20%	25.56 ± 0.16%	64.23 ± 0.28%	2.84 ± 0.10%

Table 7.5: *Breakdown of the efficiency calculated for signal and control channels.*

7.9 Systematic uncertainties

In this section the relevant sources of statistical and systematic uncertainty on the measurement of the $Br(B_s \to \mu^+\mu^-)$ are discussed.

7.9.1 Fragmentation fraction f_s

The use of the $B_u \rightarrow J/\psi K^+$ decay as normalization channel introduces in Eq. 7.20 the factor $\frac{f_u}{f_s}$, this is the main source of uncertainty in the branching ratio estimate. The fragmentation fractions depend on QCD parameters and the event energy scale. The average value and uncertainties on f_u, f_d, f_s and the ratios are summarized in Tab. 7.6 [7]. The uncertainty on f_s is the largest due to the limited world sample

$f_d = f_u$	0.398 ± 0.012
f_s	0.103 ± 0.014
$\frac{f_s}{f_u} = \frac{f_s}{f_d}$	0.265 ± 0.034

Table 7.6: *Fragmentation factors.*

of B_s collected by LEP and CDF, and the systematic uncertainties considered by combining LEP and CDF results. In the $B_s \rightarrow \mu^+\mu^-$ analysis of CDF and D0 the $B_u \rightarrow J/\psi K^+$ (see Sec. 2.2) was also chosen for the normalization. but the 14% uncertainty on f_s was less relevant given the lower B_s production rate compared to LHCb (unless they could perform the measurement as consequence of the enhancement of the $\mathrm{Br}(B_s \rightarrow \mu^+\mu^-)$). Given that LHCb can observe the SM signal in the first nominal year of data, this uncertainty is a relevant limitation.
One way to avoid the introduction of f_s in the normalization equation, is to use a B_s normalization channel. One possible candidate is $B_s^0 \rightarrow D_s^-\pi^+$. The Belle experiment has collected 23.6 fb^{-1} of data at the $\Upsilon(5S)$ resonance and has measured $\mathrm{Br}(B_s^0 \rightarrow D_s^-\pi^+) = 3.67^{+0.35}_{-0.33} \pm 0.65) \times 10^{-3}$ [93]. The relative uncertainty is of 20%, therefore with such statistical error it is not competitive.

7.9.2 Efficiency ratio

The use of the $B^0 \rightarrow J/\psi(\mu^+\mu^-)K^{*0}(K\pi)$ and $B^+ \rightarrow J/\psi(\mu^+\mu^-)K^+$ control channels, introduce in Eq. 7.20 the double-ratio $\frac{R1}{R2}$ which is a variable close to unity and less sensitive to the uncertainty in the efficiency. The average ratios are shown in Tab. 7.7. The associated statistical uncertainty can be improved using a larger sam-

$R1$	0.581 ± 0.014
$R2$	0.598 ± 0.025
$\frac{R1}{R2}$	0.972 ± 0.047

Table 7.7: *Breakdown of the efficiency ratios. The quoted uncertainties are from MC statistics.*

ple of $B^+ \rightarrow J/\psi(\mu^+\mu^-)K^+$ and $B^0 \rightarrow J/\psi(\mu^+\mu^-)K^{*0}(K\pi)$. In this study about

0.1 fb^{-1} of integrated luminosity per control channel is used. With one year of data (2 fb^{-1}) the associated statistical uncertainty will be below 1% and the double ratio will be dominated by the systematic uncertainty.
The reconstruction efficiencies ratio (R1 an R2) are strongly momentum dependent, however the double ratio is momentum independent as shown on Fig. 7.12(a). Its stability has been studied as a function of several variables (see Fig. 7.12): the B momentum, p_t of the B, number of primary vertexes, number of VELO clusters, IT clusters and OT hits; all shown in Fig. 7.12. Consequently, the considerable uncertainty in the spectrum of the B decays as well as on occupancy in the LHCb detector, does not significantly bias the determination of the double ratio.
When data becomes available, a cross-check of the simulation can also be obtained by studying the binned ratio of the yield of the two control channels, i.e. the ratio

$$\frac{\epsilon^{tot}_{(J/\psi K^*)} * Br(J/\psi K^*)}{\epsilon^{tot}_{(J/\psi K^+)} * Br(J/\psi K^+)} \times \frac{N_{(J/\psi K^+)}}{N_{(J/\psi K^*)}} \approx 1 \tag{7.22}$$

as function of the binned variables in Fig. 7.12 and sources of systematic uncertainties can be studied.

7.10 Degradation of the GL due to VELO misalignment

The expectation for the exclusion limit of the $B_s \to \mu^+\mu^-$ branching ratio described in this chapter is obtained assuming a perfectly aligned detector. As explained in Sec. 6.1, the detector geometry is corrected in software using tracks. In this section, the impact on the GL due to residual misalignment is investigated.

As a first step, a "random" misalignment is applied independently on the ϕ and r VELO sensors. The observables are then recalculated after refitting each particle track with the modified detector geometry. The misalignment has been chosen to be about 1.5 times the VELO single hit resolution [94] (see Tab. 7.8). This scale defines the width of a Gaussian distribution from which the misalignments are randomly taken and stored into a database.

As a second step, the detector geometry is corrected by using a sample of 90k MC particles tracks with at least 4 ϕ and 4 R hits and a $\chi^2/dof \leq 10$. R and ϕ sensors are aligned on all degrees of freedom (ΔT_x, ΔT_y, ΔT_z, ΔR_x, ΔR_y, ΔR_z) except for the ΔR_z of the R sensors. In total the alignment is performed over 462 degrees of freedom (21 stations $\times$ 2 VELO halves $\times$ (5+6) sensor degree of freedom). To constrain weak modes (see Sec. 6.2.2) several degrees of freedom are fixed.

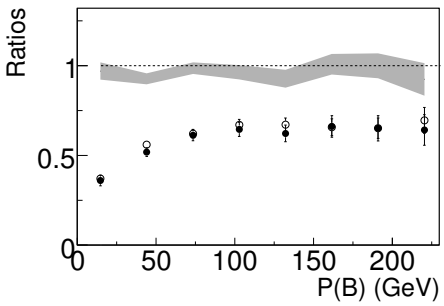

(a) B momentum

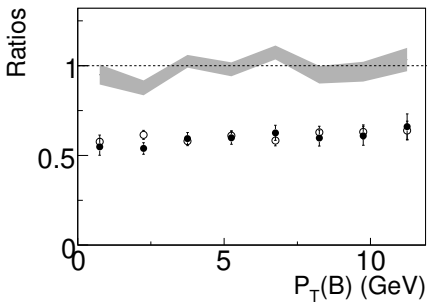

(b) B p_T

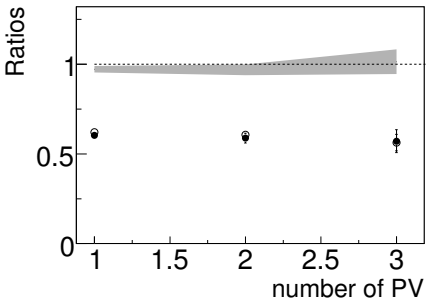

(c) Number of PV

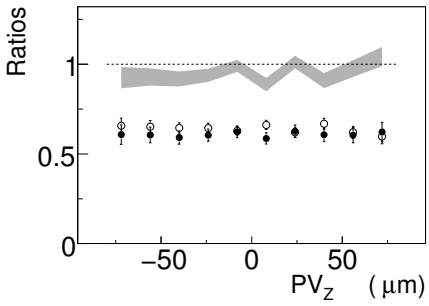

(d) PV z-position

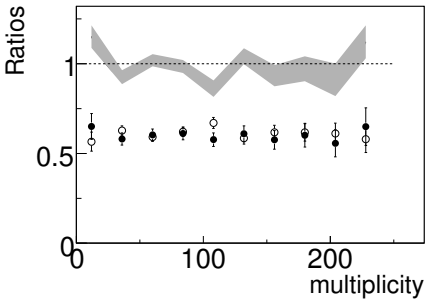

(e) Event tracks multiplicity

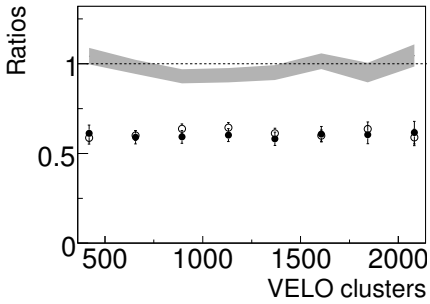

(f) VELO clusters

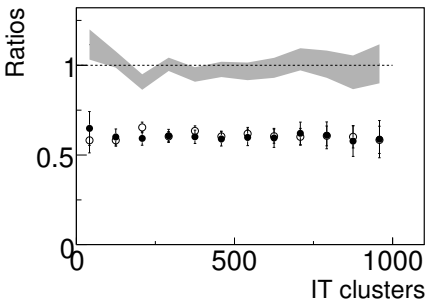

(g) IT clusters

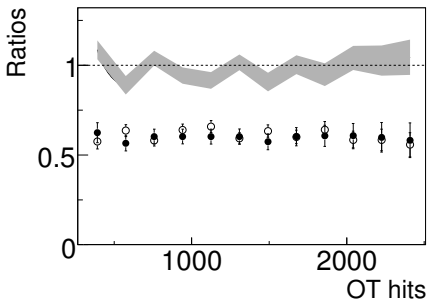

(h) OT hits

Figure 7.12: *The efficiency ratios R1 (full dots), R2 (empty dots) defined in Eq. 7.21 and the "double ratio" given by R1/R2 (grey area) as function of kinematic and occupancy related variables.*

	Translations (μm)			Rotations ($mrad$)		
Sub-detector	ΔT_x	ΔT_y	ΔT_z	ΔR_x	ΔR_y	ΔR_z
VELO modules	15	15	50	5	5	1
VELO sensors	15	15	50	5	5	1

Table 7.8: *Misalignment scales for the generation of random misalignments at the level of VELO modules and sensors.*

Observables

The effect of misalignment on observables is studied on selected signal events. The selected background is insufficient for the comparison of the shape of the distributions. The distributions of the signal observables used in the GL are shown in Fig. 7.13 in three different scenarios: Misaligned, aligned and default geometry.
Misalignments of the VELO modules and sensors affect the PV and SV. Consequently, for $B_s \to \mu^+\mu^-$ events, the distance of closest approach of the muons and the χ^2 of the B_s lifetime fit are smeared. The B_s lifetime and the asymmetry (see Figs. 7.13(a) and 7.13(d)) are not affected. After alignment with tracks, the distribution of the muons DOCA overlap with the default scenario, therefore the reconstruction of the SV is entirely un-affected by the "misalignment+alignment" procedure. The χ^2 of the lifetime fit improves, although for small χ^2 (first 3 bins) a significative difference is noticeable. This difference is attributed to residual misalignment that affects the PV reconstruction. For example, since the PV reconstruction also makes use of backward going tracks, the PV reconstruction is sensitive to the alignment of the VELO sensors upstream of the PV, whereas the SV reconstruction is not.

Geometrical likelihood

The loss of the signal-background discriminating power of the GL in the misaligned scenario, leads to an increase of the background entries in the sensitive region GL>0.6 from six to 50 as shown in Fig. 7.14(a).
After the "misalignment+alignment" procedure the distribution of the GL drastically improves and only 7 background events are in the sensitive region as shown in Fig. 7.14(b).
After the "misalignment+alignment" procedure on random misalignments, the potential of LHCb of excluding is mildly degraded and the $B_s \to \mu^+\mu^-$ branching ratio at 90% in 2 fb^{-1} result $Br^{90\%CL}(B_s \to \mu^+\mu^-)(1.89^{+1.4}_{-0.94}) \times 10^{-9}$, to be compared with Eq. 7.11.

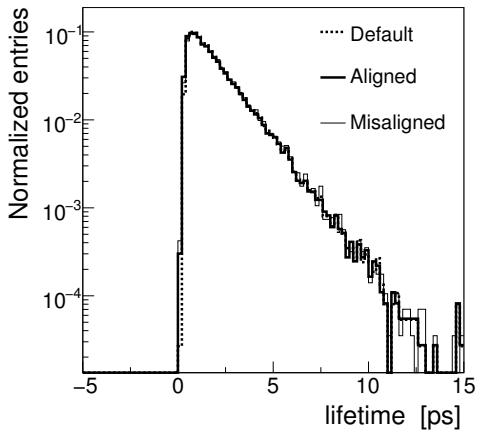

(a) B_s Lifetime

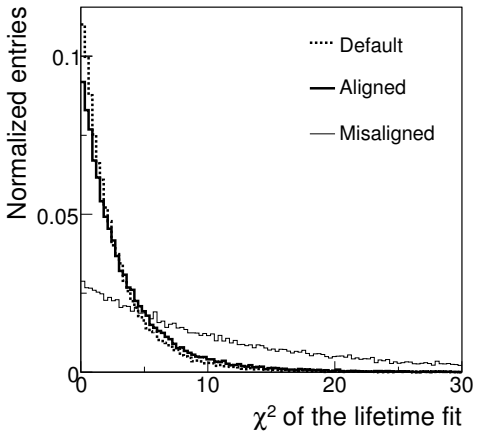

(b) χ^2 of the lifetime fit

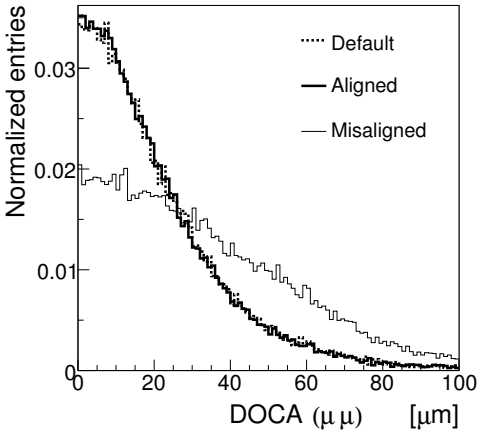

(c) DOCA muons

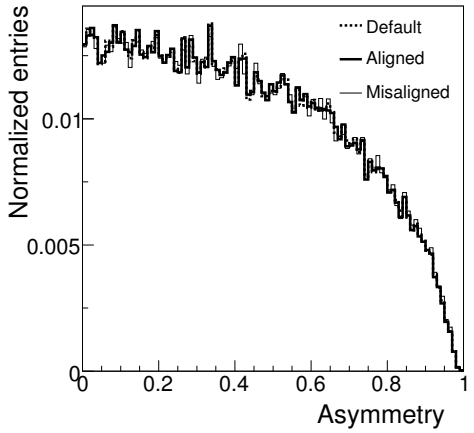

(d) Muon momentum asymmetry

Figure 7.13: *Improvement in the distribution selected signal for default geometry, aligned and misaligned scenarios.*

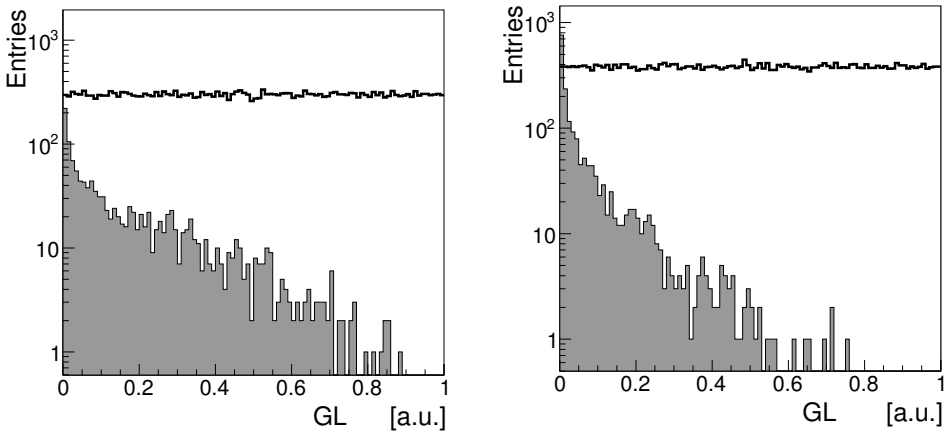

(a) GL (misaligned) (b) GL (aligned)

Figure 7.14: *The GL for signal (thick line) and preselected background (grey area) in the misaligned scenario (a) and the scenario after alignment (b).*

7.11 Outlook

The LHCb potential of measuring the $B_s \rightarrow \mu^+\mu^-$ branching ratio was investigated. The analysis consists of a loose selection and three independent observables: a likelihood built with geometrical properties of the decay (Geometrical Likelihood, GL) a PID likelihood to account for mis-identification of muons with pions or kaons (Muon Identification Likelihood, MIL) and the B_s candidate invariant mass. The amount of signal and background is measured in a sensitive region defined by maximizing the Punzi estimator for an integrated luminosity of 2 fb^{-1}. The 90%CL exclusion limit is calculated with a frequentist profile likelihood method.

In summary, the potential of LHCb of excluding the expected $B_s \rightarrow \mu^+\mu^-$ branching ratio at 90% for 2 fb^{-1} of integrated luminosity is

$$Br^{90\%CL}(B_s \rightarrow \mu^+\mu^-) = (1.86^{+1.2}_{-0.84}) \times 10^{-9}. \tag{7.23}$$

The luminosity needed to reach a 3σ evidence or 5σ discovery with respect to the SM prediction could be achieve with approximately 4 and 10 fb^{-1} of data respectively.

Chapter 8

Summary and outlook

The Standard Model of particle physics has established itself through an impressive series of successes at explaining a large variety of experimental observations and for its mathematical beauty. Despite of this, it is still regarded as an effective Quantum Field Theory, affected by several theoretical and phenomenological problems which led particle physicists to postulate the existence of New Physics beyond the Standard Model, accompanied by the existence of new, yet unobserved, particles. New heavy particles could be observed directly or indirectly through their contributions to quantum loops. Indirect contributions can change significantly the predicted SM branching ratio in Flavor Changing Neutral Currents process, where the SM contributions are suppressed. We chose to study the process $B_s \to \mu^+\mu^-$, due to its precise theoretical prediction and simple signature. The SM branching ratio is $Br(B_s \to \mu\mu) = (3.35 \pm 0.32) \times 10^{-9}$, but super-symmetrical models such as mSUGRA and NUHM predict an enhancement of the branching ratio as function of the sixth power of tanβ, which in regions of phase space with high tanβ could lead to $Br(B_s \to \mu\mu) \sim 10^{-8}$. Such large discrepancy between the SM and the measured branching ratio could then be observed experimentally.

To perform such a measurement, a copious source of B mesons is needed. LHC is the most powerful pp collider ever built, accelerating proton bunches in a ring of 27 km at a center-of-mass energy of 14 TeV, producing $b\bar{b}$ pairs in a forward and backward cone along the beam axis. LHCb, one of the four experiments along the LHC ring, is dedicated to B physics. It is designed as a single-arm spectrometer, covering a region of 300 mrad and 250 mrad in the horizontal and vertical planes, respectively. About $\sim 10^{12}$ B mesons are expected to be produced per year in the LHCb interaction point, at the nominal instantaneous luminosity of $\mathcal{L} = 2{\times}10^{32}\mathrm{cm}^{-2}\mathrm{s}^{-1}$.
One of the key components of the LHCb detector is the tracking system: it efficiently reconstructs charged tracks and measures primary and secondary decay vertices, providing precise particle momentum measurements. The LHCb tracking system

consists of a vertex locator around the interaction region (VELO), and tracking systems before and after the magnet (TT, IT, OT). In addition to a precise and efficient tracking system, LHCb features a particle identification system that provides π/K separation (two RICH detectors), electron, photon and hadron identification, (calorimeter system), and muon identification with dedicated muon chambers.

The Tracking Stations (T-stations) measure the momenta of charged particles. They cover a surface-area of about 6×5 m^2. Over this area, there is a large variation in the particle flux: the innermost part (IT) is covered with silicon strips, while the outer part (OT) is covered with straw tube drift cells. The OT reconstructs tracks with a nominal momentum resolution of about 0.5% in the momentum region from 2 to 100 GeV. The OT layers in the T stations consist of modules. Each module has two separated detector halves containing two mono-layers of straw tubes. The detector efficiency and resolution have been measured in a test beam: a resolution of 200 μm and an average cell efficiency ϵ_{cell} of 98% have been found.

The hit signals on the straws tubes are read out by the OT electronics to determine the drift times of detected particles. The OT FE Electronics consists of a fast amplifier with a baseline restoration circuit (to eliminate the slow ion tail), a discriminator and a Time-to-Digital Convertor to determine the timing of the hit. The OT Electronics have been installed and successfully commissioned. Strict selection criteria (at the chip, board and global level) guarantee a high uniformity in the preamplifier and TDC responses. In particular, all preamplifier chips (ASDBLR) can be operated with a unique threshold value without significant noise increase or efficiency loss, while the TDC resolution ($\pm$0.5 bin) is well above the required drift time resolution ($\sim$ 2 ns).

To achieve the best performance in the tracking, the detector alignment is of paramount importance. A misaligned detector leads to a deterioration of the track reconstruction in terms of efficiency loss and reduced track parameter resolution. It has been shown that misalignments between detector elements can be resolved and corrected through a χ^2 minimization alignment method based on the tracks residuals. However, this method cannot resolve misalignments to which the track χ^2 is insensitive: such scenarios generally correspond to common movements of detector elements and are called weak modes. The two most relevant weak modes for the LHCb tracking system were observed and studied: the common x-translation and the common z-translation of the T-stations. The corresponding bias in the $\frac{q}{pc}$ track parameter has been parameterized versus the misalignment scale. Moreover the bias on the invariant mass was studied by means of two decay channels: $J/\psi \to \mu\mu$ and $B_d \to \pi\pi$. The effect on the invariant mass of a B-field scale transformation and its relation with a common translation in the z-direction have been studied.

The LHCb potential at measuring the $B_s \to \mu^+\mu^-$ branching ratio was investigated. It was concluded that the SM branching ratio can be excluded at 90%CL with less than one nominal year of LHCb data (2 fb^{-1}). The analysis is based on a loose selection and three independent observables to further separate signal and background: a likelihood built with geometrical properties of the decay (Geometrical Likelihood, GL); a PID likelihood to account for mis-identification of muons with pions or kaons (Muon Identification Likelihood, MIL); and the B_s candidate invariant mass. The amount of signal and background measured in a sensitive region, defined by maximizing the Punzi estimator, was used to determine the 90%CL exclusion limit achievable with an integrated luminosity of 2 fb^{-1}. The limit was estimated by using a frequentist profile likelihood technique. The uncertainty due to the limited statistics of background events has been folded into the final result. The potential of LHCb at excluding the SM $B_s \to \mu^+\mu^-$ branching ratio at 90% CL with 2 fb^{-1} of integrated luminosity is therefore:

$$Br^{90\%CL}(B_s \to \mu^+\mu^-) = (1.86^{+1.20}_{-0.84}) \times 10^{-9}. \tag{8.1}$$

Systematic checks showed that the developed method was robust against residual misalignments.
The luminosity needed to reach a 3σ evidence (5σ discovery) with respect to the SM prediction was estimated to be 4 fb^{-1} (resp. 10 fb^{-1}).

If the Br($B_s \to \mu^+\mu^-$) is enhanced by new-physics, the measurement of the branching ratio could be achieved sooner than expected. For instance, assuming the most probable scenario predicted by the NUHM model - Br($B_s \to \mu^+\mu^-$) $\sim 10^{-8}$ - the 5σ discovery could be achieved in the first year of LHCb data, with about 2 fb^{-1} of integrated luminosity.

Bibliography

[1] P. Bechtle, O. Brein, S. Heinemeyer, G. Weiglein and K. E. Williams, *Higgs bounds: bonfronting brbitrary Higgs bectors with bxclusion bounds from LEP and the Tevatron*, [arXiv:hep-ph/0811.4169].

[2] V. Barger, J. Jiang, P. Langacker and T. Li, *Gauge coupling unification in the standard model*, Phys. Rev. Lett. B **624** (2005) 233.

[3] A. A. Andrianov and N. V. Romanenko, *Fine tuning in the Standard Model and beyond*, [arXiv.org:hep-th/9512199].

[4] A. Sakharov, *Violation of CP invariance, C asymmetry, and baryon asymmetry in the universe*, Pisma Zh. Eksp. Teor. Fiz. **5** (1967) 32-35.

[5] P. Huet, *Electroweak baryogenesis and the Standard Model*, SLAC-PUB-6492 (1994).

[6] S. Amato *et al.*, *LHCb Techical proposal*, CERN-LHCC **4** (1998).

[7] C. Amsler *et al.*, [Particle data group], *Review of particle physics*, Phys. Lett. B **667** (2008) 1.

[8] A. J. Buras, *Relations between* $\Delta M(s,d)$ *and* $B(s,d) \to \mu^+\mu^-$ *in models with minimal flavor violation*, Phys. Lett. B **566** (2003) 115-119.

[9] M. Blanke, A.J. Buras, D. Guadagnoli and C. Tarantino, *Minimal flavour fiolation waiting for precise measurements of* ΔM_s, S_{psiphi}, A^s_{SL}, $|V_{ub}|$, *gamma and* $B_s \to \mu^+\mu^-$, JHEP0610 **3** year 2006 [ArXiv.org:hep-ph/0604057].

[10] N. Cabibbo, *Unitary symmetry and leptonic decays*, Phys. Rev. Lett. **10** (1963) 531.

[11] M. Kobayashi and T. Maskawa, *CP Violation in the renormalizable theory of weak interaction*, Prog. Theor. Phys. **49** (1973) 652.

[12] R. Fleischer *et al.*, *The CKM matrix and the unitarity triangle*, [arXiv:hep-ph/0304132].

[13] S. L. Glashow, J. Iliopoulos and L. Maiani, *Weak Interactions with lepton-hadron symmetry*, Phys. Rev. D **2** (1970) 1285.

[14] F. Halzen and A. Martin, *Quarks and leptons, an introductory course in modern particle physics*, John Wiley Editor, ISBN 0-471-88741-2.

[15] T. Aaltonen *et al.*, [CDF collaboration], *Search for* $B^0_s \to \mu^+\mu^-$ *and* $B^0_d \to \mu^+\mu^-$ *decays with* $2fb^{-1}$ *of* $p\bar{p}$ *collisions*, Phys. Rev. Lett. **100** (2008) 101802.

[16] [D0 Collaboration] *A new expected upper limit on* $B^0_s \to \mu^+\mu^-$ *using 5* fb^{-1} *of run II data*, D0 note 5906.

[17] ATLAS collaboration, *ATLAS detector and physics performance technical design report*, CERN-LHCC 98-13.

[18] V. Adler *et al.*, *CMS physics: technical design report*, CERN-LHCC (2006).

[19] N. V. Nikitin, S. Y. Sivoklokov, L. N. Smirnova, D. A. Tlisov and K. S. Toms, *Possibility of recording rare muonic decays of B mesons at the ATLAS detector in the case of LHC operation in the initial-luminosity mode*, Phys. Atom. Nucl. **70** (2007) 2086.

[20] K. A. Ulmer et al. *Prospects for measurements of rare B decays and other heavy flavour physics at CMS*, Nucl. Phys. Proc. Suppl. **187** (2009) 57.

[21] R. Barate *et al.*, *Search for the standard model Higgs boson at LEP*, Phys. Lett. B **565** (2003) 61.

[22] D. D. Price, *Search for Standard Model Higgs in* $W\ H \rightarrow l\nu bb$ *at the Tevatron*, [arXiv.org:hep-ex/0910.3420].

[23] S. P. Martin, *A supersymmetry primer*, [arXiv:hep-ph/9709356].

[24] J. R. Ellis, J. S. Hagelin, D. V. Nanopoulos, K. A. Olive and M. Srednicki, *Supersymmetric relics from the big bang*, Nucl. Phys. B **238** (1984) 453.

[25] M. Drees and S.P. Martin, *Electroweak symmetry breaking and new physics at the TeV Scale*, World Scientific (1996) 146-215.

[26] A. Dedes, H. K. Dreiner and U. Nierste, *Correlation of* $B_s \rightarrow \mu^+\mu^-$ *and (g-2)* (μ) *in minimal supergravity*, Phys. Rev. Lett. **87** (2001) 251804.

[27] J. Ellis, T. Hahn, S. Heinemeyer, K. A. Olive and G. Weiglein, *WMAP-Compliant benchmark surfaces for MSSM Higgs bosons* [arXiv.org:hep-ex/0709.0098].

[28] C.L. Bennett *et al.*, *First year Wilkinson Microwave Anisotropy Probe (WMAP) observations: Preliminary maps and basic results* The Astrophysical Journal **148** (2003).

[29] G.W. Bennett *et al.*, *Measurement of the negative muon anomalous magnetic moment to 0.7 ppm*, Phys. Rev. Lett. **92** (2004).

[30] S. Myers, *The LEP collider, from design to approval and commissioning*, CERN yellow report **08** (1991).

[31] P. Lebrun *et al.*, *LHC Design Report. Vol.I: The LHC main ring*, CERN Geneva (2004).

[32] E. Abat *et al.*, *The ATLAS Transition Radiation Tracker (TRT) proportional drift tube: Design and performance*, JINST **3** (2008) P02013.

[33] F. Antinori it et al., *ALICE, Technical Proposal for A Large Ion Collider Experiment at the CERN LHC*, CERN-LHCC (1995) 95-71.

[34] S. Amato *et al.*, *"LHCb reoptimized detector design and performance: technical design report*, CERN-LHCC bf 30 (2003).

[35] T. Sjöstrand, S. Mrenna and P. Skands, *A Brief Introduction to PYTHIA 8.1*, Comput. Phys. Commun. **178** (2008) 852 [arXiv:hep-ph/:0710.3820].

[36] A. Hicheur and G. Conti, *Private communications: LHCb-2007-093 internal note.*

[37] A. Keune, *Parameterization of the LHCb Magnetic Field Map*, LHCb note **2** (2009).

[38] S. Amato *et al.*, *LHCb Vertex Locator technical design report*, CERN-LHCC **11** (2001)

[39] S. Amato *et al.*, *LHCb Inner Tracker technical design report*, CERN-LHCC **29** (2002).

[40] S. Amato *et al.*, *Outer Tracker technical design report*, CERN-LHCC **24** (2001).

[41] S. Amato *et al.*, *LHCb RICH technical design report*, CERN-LHCC **37** (2000).

[42] N. Brook *et al.*, *LHCb RICH1 Engineering Design Review Report*, LHCb note **121** (2004).

[43] S. Amato *et al.*, *LHCb Calorimeters technical design report*, CERN-LHCC **36** (2000).

[44] S. Amato *et al.*, *LHCb Trigger System technical design report*, CERN-LHCC **31** (2003).

[45] A. Alves *et al.*, *The LHCb Detector at The LHC*, JINST **3** (2008) S08005.

[46] E. Bos, *Reconstruction of charged particles in the LHCb detector*, LHCb PhD thesis (2010).

[47] B. Hommels, *The Tracker in the Trigger of LHCb*, LHCb PhD thesis (2006).

[48] J. Nardulli and N. Tuning, *Private communication: LHCb-2004-114 internal note.*

[49] P. Vankov, *Study of the B meson lifetime and the performance of the Outer Tracker at LHCb*, LHCb PhD thesis (2008).

[50] Y. Guz *et al.*, *Wire tension meter for the Production of the LHCb Outer Tracker - commissioning and calibration* LHCb note **34** (2004).

[51] G. van Apeldoorn *et al.*, *Outer Tracker module production at NIKHEF - Quality Assurance*, LHCb note **78** (2004).

[52] G. van Apeldoorn *et al.*, *Beam tests of final modules and electronics of the LHCb Outer Tracker in 2005*, LHCb note **76** (2005).

[53] E. Simioni and Y. Guz, *Private communication*, [37th LHCb week at CERN, OT Session].

[54] S. Bachmann, *Ageing studies for the straw tube detectors for the LHCb outer tracking system*, IEEE-2004 NSS-MIC (2004).

[55] S. Bachmann, *The straw tube technology for the LHCb outer tracking system*, Nucl. Instr. and Methods A **535** (2004) 171-174.

[56] G. van Apeldoorn *et al.*, *Aging studies of straw tube chambers*, LHCb note **3** (2001).

[57] S. Bachmann, *The straw tube technology for the LHCb outer tracking system*, Nucl. Instr. and Methods A **535** (2004) 171-174.

[58] M. Blom, *Aging in the LHCb Outer Tracker*, Vrije Universiteit, Amsterdam, LHCb master thesis (2009).

[59] I. Mous, *Aging in the LHCb Outer Tracker*, Vrije Universiteit, Amsterdam, Amsterdam, LHCb master thesis (2007).

[60] V. Faerber and U. Uwer, *Private communication*, [50th LHCb week at CERN, OT Session].

[61] N. Tuning, *Private communication.*

[62] E. Abat *et al.*, *The ATLAS Transition Radiation Tracker (TRT) proportional drift tube: Design and performance*, JINST **3** (2008) P02013.

[63] M. Newcomer *et al.*, *Radiation Hardness: Design Approach and Measurements of the ASDBLR ASIC for the ATLAS TRT*, IEEE Nuclear Science Symposium Conference Record **1** (2002).

[64] G. Cervelli *et al.*, *A 0.13 μm CMOS serializer for data and trigger optical links in particle physics experiments*, IEEE Nuclear Science Transactions **51** (2004) 836-841.

[65] A. Pellegrino *et al.*, *Study of the Global Performance of an LHCb OT Front-End electronics prototype*, LHCb note **120** (2004).

[66] A. Pellegrino *et al.*, *Noise studies with the LHCb Outer Tracker ASDBLR board*, LHCb note **117** (2004).

[67] E. Simioni, A. Pellegrino and T. Sluijk, *Selection of ADSLBR chip for LHCb Outer Tracker FE*, LHCb note **88** (2005).

[68] E. Simioni, *OT FE boards test and production*, LHCb note **122** (2007).

[69] ATLAS Online, *http://hsi.web.cern.ch/HSI/s-link/devices/hola*.

[70] W. Hulsbergen and A. Bocci, *TRT alignment for SR1 cosmic mand beyond*, CERN-ATL-COM-INDET **11** (2007).

[71] W. Hulsbergen, *The global covariance matrix of tracks fitted with a Kalman filter and an application in detector alignment*, Nucl. Instrum. Meth. A **600** (2009) 471.

[72] L. Nicolas, J. Amoraal, A. Hicheur, W. Hulsbergen, M. Needham and G. Raven, *Alignment of LHCb tracking stations with tracks fitted with a Kalman filter*, LHCb note **66** (2008).

[73] J. Amoraal, *Alignment with Kalman fitted tracks* LHCb PhD thesis (2010).

[74] J. van Tilburg, *Track simulation and reconstruction in LHCb*, LHCb PhD thesis (2005).

[75] J. Amoraal, *The $J/\psi \to \mu\mu$ selection*, LHCb note **52** (2007).

[76] A. Carbone *et al.*, *Charmless charged two-body B decays at LHCb*, LHCb note **59** (2007).

[77] *Vector Fields Limited, 24 Bankside, Kidington, Oxford OX5 1JE, England*.

[78] R. Bernhard *et al.*, *A Combination of CDF and DO Limits on the Branching Ratio of $B_{s/d} \to \mu^+\mu^-$ Decays*, [arXiv:hep-ex/0508058].

[79] H. Morata *et al.*, *Measurement of trigger efficiencies and biases*, LHCb note **73** (2008).

[80] E. Simioni, F. Teubert, D. Martinez *et al.*, *Roadmap for selected key measurements of LHCb*, LHCb publication **29** (2009) [arXiv:hep-exp/09124179].

[81] R. Antunes-Nobrega *et al.*, *LHCb computing: technical design report* CERN-LHCC (2005).

[82] T. Sjostrand, M.H. Seymour, *PYTHIA and HERWIG for Linear Collider Physics*, [arXiv:hep-ph/9909346].

[83] D. J. Lange, *The EvtGen particle decay simulation package*, Nucl. Instrum. Meth. A **462** (2001) 152.

[84] M. Beneke and M. Neubert, *QCD factorization for $B \to PP$ and $B \to PV$ decays*, Nucl. Phys. B **675** (2003) 333.

[85] E. Parzen, *On estimation of a probability density function and mode*, Ann. Math. Stat. **33** (1962) 1065-1076.

[86] D. Perego, *Characterization of Silica Aerogel for the LHCb RICH Detector and Measurement of the Oscillation Parameter Δm_s*, LHCb PhD thesis (2005).

[87] G. Punzi, *Sensitivity of searches for new signals and its optimization*, [arXiv:physics/0308063].

[88] W. A. Rolke, A. M. Lopez and J. Conrad, *Confidence intervals with frequentist treatment of statistical and systematic uncertainties*, Nucl. Instrum. Meth. A **551** (2005) 493.

[89] L. Moneta, I. Antcheva, R. Brun and A. Kreshuk, *Root statistical software*, CERN **1** (2008), www.root.cern.ch.

[90] D. Martinez, J. Hernando and F. Teubert, *LHCb potential to measure/exclure the branching ratio of the decay $Bs \to \mu^+\mu^-$*, LHCb note **33** (2007).

[91] T. Junk, *Sensitivity, exclusion and discovery with small signals, large backgrounds, and large systematic uncertainties* CDF note **8128** (2007).

[92] T. Junk, *Building a more general χ^2*, CDF note **7904** (2006).

[93] A. Drutskoy, *Y(5S) and B_s decays at Belle*, [arXiv:hep-ex/0905.2959].

[94] M. Gersabeck, J. Nardulli and E. Rodrigues, *Impact of misalignments on the analysis of B decays*, LHCb note **12** (2008).

Samenvatting en vooruitzicht

Nieuwe fysica in zeldzame beauty-vervallen

Het Standaard Model van de deeltjesfysika is, naast het feit dat het over een mathematische schoonheid beschikt, experimenteel bevestigd door verklaringen te geven voor een indrukwekkende reeks van waarnemingen. Desondanks wordt het nog steeds beschouwd als een effectieve Quantum Velden Theorie met verschillende theoretische en fenomenologische problemen, welke deel-tjes-fysici ertoe brachten het bestaan van Nieuwe Fysica voorbij het Standaard Model (SM) te postuleren, vergezeld van het bestaan van nieuwe, nog niet waargenomen, deeltjes. Nieuwe zware deeltjes zouden direct waargenomen kunnen worden, of indirect door middel van hun bijdrage aan quantum-lussen. Indirecte bijdrages kunnen voorspelde SM vervalsfracties in Flavour Changing Neutral Current-processen significant vEranderen, daar waar de SM bijdrages onderdrukt zijn. Wij kozen ervoor om het proces $B_s \to \mu^+\mu^-$ te bestuderen, vanwege zijn nauwkeurige theoretisch voorspelde vervalsfractie en simpele signatuur. De SM vervalsfractie is $Br(B_s \to \mu^+\mu^-) = (3.35 \pm 0.32) \times 10^{-9}$, maar supersymmetrische modellen zoals mSUGRA en NUHM voorspellen een toename van de vervalsfractie als functie van de zesde macht van $\tan\beta$, welke in gebieden van de faseruimte met hoge $\tan\beta$ kan leiden tot $Br(B_s \to \mu^+\mu^-) \sim 10^{-8}$. Een zo grote discrepantie tussen de voorspelling in het SM en de gemeten vervalsfractie zou experimenteel waargenomen kunnen worden.

Om zo een meting te kunnen uitvoeren, is een intense bron van B mesonen nodig. De krachtigste *pp* deeltjes-versneller ooit gebouwd is de LHC, die protonbundels in een ring van 27 km bij een zwaartepuntsenergie van 14 TeV laat botsen, waarbij $b\bar{b}$-paren in een voorwaartse en een achterwaartse kegel langs de bundel-as geproduceerd worden. LHCb, één van de vier experimenten aan de LHC-ring, is toegewijd aan B-fysica. Het is ontworpen als een spectrometer met één arm, die een gebied van 300 mrad en 250 mrad in het horizontale en respectievelijk verticale vlak bestrijkt. Ongeveer 10^{12} B-mesonen zullen elk jaar geproduceerd worden in de LHC, bij een nominale instantane luminositeit van $\mathcal{L} = 2 \times 10^{32}$ cm^{-2} s^{-1}. Eén van de belangrijkste componenten van de LHCb-detector is het tracking-systeem: het systeem dat geladen sporen efficiënt reconstrueert en primaire en secundaire vertices meet, waarbij nauwkeurige metingen van de impuls van deeltjes worden verschaft.

Het tracking-systeem van LHCb bestaat uit een systeem dat de vertex bepaalt (de VELO) en systemen die geladen sporen voor en achter de magneet reconstrueren (TT, IT, OT). Naast een nauwkeurig en efficient tracking systeem, beschikt LHCb over een systeem voor deeltjes-identificatie voor scheiding van π/K (twee RICH-detectoren), elektron-, foton- en hadron-identificatie (het systeem van calorimeters) en muon-identificatie met behulp van muon-kamers.

De Tracking Stations (T-stations) meten de impulsen van geladen deeltjes. Ze beslaan een oppervlak van ongeveer 6×5 m^2. Over dit gebied is er een grote variatie in deeltjes-flux: het binnenste deel (IT) bestaat uit silicium strips, het buitenste deel (OT) bestaat uit drift-buizen (of rietjes). De OT reconstrueert sporen met een nominale impuls-resolutie van ongeveer 0.5% in het impulsgebied van 2 tot 100 GeV. De OT-lagen in de T-stations bestaan uit modules. Elke module heeft twee aparte detector-helften die twee mono-lagen van strootjes bevatten. De efficiëntie en resolutie van de de detector zijn gemeten in een test-bundel: een resolutie van 200 μm en een gemiddelde cel-efficiëntie ϵ_{cell} van 98% zijn gevonden.

De trefsignalen van de rietjes worden uitgelezen door de OT-electronica om de drifttijden te bepalen. De FE-electronica van de OT bestaat schematisch uit een snelle versterker met een circuit dat de baseline herstelt (om de langzame ionenstaart te elimineren), een discriminator en een Tijd-naar-Digitaal Converter (TDC) om de timing van de hit te bepalen. De OT-electronica is geïnstalleerd en succesvol in bedrijf gesteld. Nauwkeurige selectie-criteria (op het niveau van de chip, van het bord en op globaal niveau) garanderen een grote gelijkmatigheid in de responsen van de voorversteker en de TDC. In het bijzonder kunnen alle voorversterker-chips (ASDBLR) functioneren met unieke waardes van de drempel, zonder significante groei van de ruis of verlies van efficiëntie, terwijl de TDC-resolutie (± 0.5 bin) ruim boven de benodigde resolutie van de drifttijd (~ 2 ns) is.

Voor de beste prestatie van de spoorreconstructie is de uitlijning (alignment) van de detector van het allergrootste belang. Een verkeerd uitgelijnde detector heeft een verslechtering van de spoorreconstructie tot gevolg in termen van het verlies van efficiëntie en verminderde resolutie van de track-parameters. Het is aangetoond dat fouten in de uitlijning (misalignments) tussen detector-elementen kunnen worden bepaald en gecorrigeerd door middel van een alignment-methode, waarbij een χ^2 gebaseerd op de track-residuen wordt geminimaliseerd. Echter, deze methode kan geen misalignments aantonen waarvoor de χ^2 van de track ongevoelig is: zulke scenario's corresponderen in het algemeen met gemeenschappelijke bewegingen van detector-elementen en worden 'zwakke modi' genoemd. De twee meest relevante zwakke modi voor het tracking-systeem van LHCb zijn gevonden en bestudeerd: gemeenschappelijke verschuiving van de T-stations in de x-richting en in de z-richting. De bijbehorende systematische afwijking in de $\frac{q}{pc}$ track-parameter is geparametrizeerd als functie van de schaal van de misalignment. Bovendien is de systematische afwijking van de schaal van de misalignment bestudeerd met twee vervalskanalen: $J/\psi \to \mu^+\mu^-$ en $B_d \to \pi\pi$. Het effect op de invariante massa van

een schaaltransformatie van het magneetveld en zijn verhouding met een gemeenschappelijke verschuiving in de z-richting zijn bestudeerd.

De mogelijkheid voor LHCb om de $B_s \to \mu^+\mu^-$ vervalsfractie te meten is bestudeerd. Er is geconcludeerd dat de SM vervalsfractie uitgesloten kan worden met 90%CL met minder dan een jaar van LHCb data (2 fb^{-1}). De analyse is gebaseerd op een losse selectie en drie onafhankelijke variabelen om signaal en achtergrond nog meer te scheiden: een waarschijnlijkheid geconstrueerd met geometrische eigenschappen van het verval (Geometrische Waarschijnlijkheid, GL); een PID waarschijnlijkheid om mis-identificatie van muonen met pionen of kaonen in rekening te brengen (Muon Identificatie Waarchijnlijkheid, MIL); en de invariante massa van de B_s-kandidaat. De hoeveelheid signaal en achtergrond gemeten in een gevoelig gebied, vastgelegd door de Punzi-estimator te maximalizeren, is gebruikt om vast te stellen wat de limiet is die met 90%CL kan worden uitgesloten met een geïntegreerde luminositeit van 2 fb^{-1}. De limiet was bepaald door de techniek van de *frequentist profile likelihood* te gebruiken. De onzekerheid ten gevolge van de beperkte hoeveelheid achtergrond-events is meegenomen in het uiteindelijke resultaat. De daaruit volgende mogelijkheid voor LHCb om de SM vervalsfractie van $B_s \to \mu^+\mu^-$ uit te sluiten met 90%CL met 2 fb^{-1} geïntegreerde luminositeit is:

$$Br^{90\%CL}(B_s \to \mu^+\mu^-) = (1.86^{+1.20}_{-0.84}) \times 10^{-9}.$$

Systematische controles hebben aangetoond dat de ontwikkelde methode bestand is tegen *residual* misalignments. De luminositeit benodigd om een 3σ aanwijzing (5σ ontdekking) ten opzichte van de SM voorspelling te vinden is bepaald op 4 fb^{-1} (resp. 10 fb^{-1}).

Als de $Br(B_s \to \mu^+\mu^-)$ vergroot is door Nieuwe Fysica, zal de meting van de vervalsfractie eerder verricht kunnen worden dan verwacht voor het SM. Bijvoorbeeld, in het geval van het meest waarschijnlijke scenario voorspeld door het NUHM model - $Br(B_s \to \mu^+\mu^-) \sim 10^{-8}$ - kan de 5σ ontdekking bereikt worden in het eerste jaar van LHCb data, met ongeveer 2 fb^{-1} aan geïntegreerde luminositeit.

Acknowledgments

It was a cold and dark night of October in the year of the Lord 2004, about three months after my graduation, when I started sending my CV and letters of intention to B-Physics group leaders among several European universities. The winner was Jo van der Brand, who forwarded my request to Antonio Pellegrino. Antonio initially called me for a phone interview and - to make a long story short - in December I was visiting NIKHEF but only in march of 2005 I finally started my PhD. I was very impressed by the excellent organization and the kindness of the people, moreover the prospect of having a real salary and not just a scholarship as in the Italian system, push me to decide of taking the chance.

Antonio has been not just an amazing supervisor due to his smartness, deep technical knowledge of the hardware and coding skills, but is also the only person who can ask me "Eduard, da uno a dieci, quanto sei coglione?" and make me happy to answer "dieci" without being arrested for homicide. I would really thanks Antonio who gave me the possibility to start this experience: I hope I managed to pay back his trust in those years.

Another very peculiar "element" that I want to thanks, is the B-Physics group leader at NIKHEF, Marcel Merk. His feedbacks and advices have been fundamental to bring this thesis to an academical level. I'm quite sure I'll never find anyone else who can - in a harmless group outing - make me so drunk to fall down the bike three times in a night and wake up the day after bleeding from the forehead with little memory of what happened. The lesson was to never challenge Marcel if drinks are involved.

Another person I would like to thanks is Wouter Hulsbergen. This guy is extraordinary smart, it has been a real pleasure to work with him during the second part of my PhD. I really appreciated his way to face problems and focusing on the most relevant aspects of them, even when he told me about the results of a couple of months of work "Eduard, this is useless, let's restart from scratch on relevant misalignment configurations involving common movements of the sub-detectors".

I would like also to thanks the $B_s \to \mu^+\mu^-$ task force, who participated in improving and giving ideas to carry out this thesis, in particular Frederic Teubert, Gaia Lanfranchi and Olivier Schneider. Was very inspiring to join and participate their meetings and activities. I'm grateful to Diego Martinez, Hugo Ruiz, Marc Olivier-Bettler, Antonio Perez for the useful discussions.

There have been other persons who helped me during those years, first of all Niels Tuning, the "NIKHEF kind soul" and "aging master" who helped me to get into the group. I think I'm the only person who managed to get Niels really angry once in arguing about an internal note but - lucky me - he has also excellent forgiving skills. Moreover, Yury Guz with which I had the pleasure to work with for few months during my first year and share the chill of observing what later on became the infamous OT aging issue, Herve Terrier the only french in our group and an hard worker, all the electronics department, in particular Tom Sluijk, Ad Berkien and Albert Zwart. Every time I talked with Tom was like and injection of joy. About Albert I regret I never saw him performing with his jazz band.
I would also thanks Oscar van Petten and Luk Ceelie and the entire mechanics department Without Oscar, my boat would be still in the Flevopark with the engine broken!

Coming back to physics I am definitely grateful to Nicola Serra, who helped me in the analysis work, sharing his code and experience in a friendly and efficient way. I'll never forget the night in which we debug my hybrid algorithm... me, heavily cursing, he, rolling on the floor laughing. I'm looking forward to restart punching and kicking each other at the boxing club at CERN with Jacopo ed Alessio very soon.

I would also thanks my several office mates/colleagues: Jacopo Nardulli, who introduced me into the world of the LHCb software and for the unforgettable dinners (ah... le specialita di pesce!); Edwin Bos and his discussions about the pursuit of the good life; Tristan Du Pree because another one like that is simply impossible to find; Besma M'charek (with her older sister, her mum plus the two Jewish nephews) for the fun and the excellent Tunisian delicatessen; Fabian Jansen for his criticism, precision and useful discussions, Aras Papadelis for his countless funny stories (I'll never forget that poor squirrel...) and just because is always nice to talk with him; Mathieu Blom which daily challenged me on the dart board, I'm looking forward to find another warrior as you; Daan van Eijk probably the best office mate ever, who can appreciated classical music and at the same time eat disgusting sandwich and throw me back staplers, pens etc.: unfortunately he never understood me while I was speaking Mesopotamian languages; Milena Dyulendarova for her sweetness an the beautiful T-shirt of Moscow, Sipho van der Putten, for being my regular "bras d'honneur" challenger who adopt this italian-french tradition and gave me hard time in the last two years, Polina Georgieva for teaching me the longest bulgarian word

and helping me doing shopping in France; Ernesta Swanepoel, for her natural way of being extraordinary; and finally but not for importance, Jan Amoraal and Gabriel Ybeles Smit: those two guys are like brothers for me, we have had such a great time and so many useful discussion about code and physics which is one of my greatest regret of leaving NIKHEF. I wish them the best luck looking forward to meet each other again in the near future.

I keep separate the Italian (or Italian related) office mates/colleagues section, since there are so many: I start to thanks Sarah Bernardis who encouraged me to look for a PhD abroad, I know her since many years and still she always manage to surprise me as the first time; Serena Oggero, for her smartness, kindness and for having increased my music skills; Giada Carminati and Gordon Lim for their sincere friendship and countless outing, beer, jenever, brandewijn etc.; Chiara Farinelli and Hegoi Garitaonandia for their kindness, Michele Maio the only string theorist I can talk with; Dorothea Fonnesu, for being able to catalyze on me several non-sense actions as the first break-in into the tunnel of a dutch accelerator; Claudio Bogazzi, despite his devotion to the Internazionale football team; Barbara Storaci e Samuele Kaplun for the failed attempt of improving my habits, Patrizia Trevisan for the failed attempt of improving my ethic, Francesco Zappon e Daniele Dequal for our common venetian roots (e che ghe mancaria anca quela!).

A special thanks to Matteo Durighetto, The president the Vice-President and all the P.A.P.A. association, for our legendary meetings we had in the last decade. Now that we are spread over the world, the spirit is alive as it has never been before!

I would like to thanks the wijnand focking in Amsterdam and the bold barman, for producing the best jenever and brandewijn of the Netherlands.

Infine un ringraziamento speciale va alla mia famiglia: a mio papa per avermi sempre incoraggiato a migliorarmi, a mia mamma per avermi dato un po del suo lato artistico ed il suo immenso affetto ed infine a mio fratello, che ha sempre creduto in me ed aiutato nei momenti difficili.